Diplomarbeit

Experimental analysis of a compression heat pump with an integrated latent storage

ausgeführt zum Zwecke der Erlangung des akademischen Grades eines

Diplom-Ingenieurs

eingereicht an der Technischen Universität Wien, Fakultät für Maschinenwesen

und Betriebswissenschaft

von

Philipp Mascherbauer, Bsc

Matr.Nr.: 01226798

unter der Anleitung von

Dipl.-Ing. Dr. techn. Klemens Marx, MBA

Dipl.-Ing. Dr. techn. Johann Emhofer

Privatdoz. Dipl.-Ing. Dr. techn. Christoph Reichl

Institut für Strömungsmechanik und Wärmeübertragung

Wien am 19/02/2020 _____

Ich habe zur Kenntnis genommen, dass ich zur Drucklegung meiner Arbeit unter der Bezeichnung

Diplomarbeit

nur mit Bewilligung der Prüfungskommission berechtigt bin.

Ich erkläre weiters an Eides statt, dass ich meine Diplomarbeit nach den anerkannten Grundsätzen für wissenschaftliche Abhandlungen selbständig ausgeführt habe und alle verwendeten Hilfsmittel, insbesondere die zugrunde gelegte Literatur genannt habe.

Weiters erkläre ich, dass ich dieses Diplomarbeitsthema bisher weder im In- noch Ausland (einer Beurteilerin/einem Beurteiler zur Begutachtung) in irgendeiner Form als Prüfungsarbeit vorgelegt habe und dass diese Arbeit mit der vom Begutachter beurteilten Arbeit übereinstimmt.

Danksagung

Ich möchte mich an dieser Stelle bei allen bedanken, die mir während dem Verfassen dieser Diplomarbeit zur Seite gestanden sind.

Mein großer Dank gilt Priv. Doz. Dr. Christoph Reichl, der sich immer Zeit für mich genommen hat, und mir jederzeit mit seinem Fachwissen Hilfe leistete. Sein Enthusiasmus brachte mich dazu, das meiste aus meinen Ergebnissen heraus zu holen.

Mein besonderer Dank geht außerdem an Dr. MBA Klemens Marx der mich nicht nur in die Thematik einführte, sondern mir auch während des gesamten Prozesses immer zu Seite stand und mit seinem Fachwissen den Weg ebnete. Durch seine Hilfe war es mir möglich über mein eigentliches Forschungsziel hinaus zu forschen und mir einen großen Anteil zusätzliches Wissen anzueignen.

Ein weiterer Dank geht an das AIT - Austrian Institute of Technology - und dem Center for Energy. Hierbei möchte ich mich besonders bei Dr. Johann Emhofer, Dr. Tilman Barz sowie MSC Johannes Krämer bedanken, die mir wichtige Inputs lieferten.

Zu guter Letzt möchte ich mich bei meinen Eltern bedanken, ohne die ich dieses Ziel nie erreichen hätte können. Außerdem gebührt mein Dank meinen Schwestern und meiner Freundin Dóra, die mich sowohl während der Arbeit als auch auf dem Weg dahin moralisch unterstützen.

Kurzfassung

Die Wärmeenergie für die Trinkwassererwärmung in Wohngebäuden wird heute überwiegend in durchaus sinnvollen Wasserspeichern gespeichert. Sie sind kostengünstig und weit verbreitet. Aber obwohl die spezifische Wärme des Wassers hoch ist, könnten Materialien, die einen Phasenwechsel durchführen, eine deutlich höhere Speicherenergiedichte erreichen als ein herkömmlicher Wasserspeicher.

Die folgenden Themen werden in diese Arbeit einbezogen:

- Experimentelle Tests von neuartigen latenten Wärmespeicher/Wärmetauscher Modulen für Wohngebäude, die in einen Wärmepumpenzyklus integriert sind.
- Anpassungen des Versuchsaufbaus und des experimentellen Hardware-in-the-Loop Setups.
- Auswertung und Analyse der Ergebnisse und Vergleich von Messungen mit Simulationen.
- Entwicklung von Korrelationen für das Verhalten des Phasenwechselmaterials im Latentwärmespeicher.

Im Rahmen der vorliegenden Masterarbeit wird eine neuartige Speicherkomponente, ein leistungsstarkes Wärmespeicher/Wärmetauscher Modul, direkt in den Kältemittelkreislauf einer Wärmepumpe integriert und in einem thermisch gesteuerten Labor experimentell getestet, das für Hardware in den Kreislaufversuchen bereit ist.

Die experimentellen Ergebnisse werden kontinuierlich diskutiert. Schließlich wird die Arbeit eine umfassende Analyse der Experimente geben und mögliche Betriebsarten in Wohngebäuden und die Machbarkeit von Upscaling diskutieren.

Zusätzlich wird das verwendete Phasenwechselmaterial in einem separaten Versuchsaufbau untersucht. Es wird versucht eine Korrelation zwischen der Dicke der Festphase und dem Wärmestrom durch das Phasenwechselmaterial zu finden. Dabei wird das Schmelz- und Erstarrungsverhalten genauer beobachtet.

Abstract

Today, the thermal energy for domestic hot water in residential buildings is mainly stored in sensible water storages. They are cost-efficient and widely available. But although the specific heat of water is high, materials carrying out a phase change could reach significantly higher storage energy density compared to a conventional sensible water storages.

The following topics will be included in the thesis:

- Experimental tests of novel latent heat storage/heat exchanger modules integrated into a heat pump cycle for residential buildings.
- Adaptions of the experimental set-up and experimental hardware in the loop analysis
- Evaluation and analysis of the results and comparison of measurements with simulations.
- Development of correlations for the behavior of the phase change material in the latent heat storage.

Within the present master thesis, a novel storage component, a high-performance latent heat storage/heat exchanger module, will be integrated directly into the refrigerant cycle of a heat pump and will be experimentally tested in a thermally controlled laboratory ready for hardware in the loop experiments.

Experimental results will be discussed continuously. Finally, the thesis will give a comprehensive analysis of the experiments and will discuss possible operation modes in residential buildings and the feasibility of upscaling.

Additionally, the used phase change material is investigated in a separate experimental setup. An attempt is made to find a correlation between the thickness of the solid phase and the heat flow through the phase change material. The melting and solidification behavior is observed in greater detail.

Table of contents

Nomenclature

Abbreviations

AC	alternating current
AIT	Austrian Institute of Technology
ASHP	air source heat pump
CFC	chlorofluorocarbons
CO_2	carbon dioxide
DC	direct current
DHW	domestic hot water
GSHP	ground source heat pump
GWP	global warming potential
HC	hydrocarbons
HCFC	hydrochlorofluorocarbons
HFC	hydrofluorocarbons
HP	heat pump
IEA	International Energy Agency
ODP	ozone depletion potential
PCM	phase change material
R-32	refrigerant difluoromethane
RPW-HEX	refrigerant phase change material water – heat exchanger
SoC	state of charge
TES	thermal energy storage

Subscripts

aluminum	aluminum
amb	ambient
charging	charging
cold	cold
compressor	compressor
Cond	condenser
discharging	discharging
el	electrical
fan	fan
Hot	hot
loss	loss
max	maximum
R	refrigerant
tot	total
RPW	RPW-HEX
RT64	phase change material RT64
thermal	thermal
W	water

Latin Symbols

c_p	specific heat capacity	$Jkg^{-1}K^{-1}$
COP	coefficient of performance	1
E	energy	Ws
g	gravitational constant	ms^{-2}
I	current	A
l	characteristic length	m
$\dot{m}$	mass flow	kgs^{-1}
Nu	Nusselt Number	1
P	electric power	W
p	pressure	Pa
PF	performance factor	1
Pr	Prandtl number	1
$\dot{Q}$	thermal power	W
$\dot{q}$	heat flux	$W\ m^{-2}$
Ra	Rayleigh number	1
Re	Reynolds number	1
RH	relative air humidity	%
T	temperature	K
t	time	S
u	rotational speed	$Rads^{-1}$
U	voltage	V
V	Volume	m^3
W	electric work	W
x	thickness	m

Greek Symbols

α	heat transfer coefficient	$Wm^{-2}K^{-1}$
β	reciprocal temperature	K^{-1}
Δ	difference	()
λ	thermal conductivity coefficient	$Wm^{-1}K^{-1}$
ν	dynamic viscosity	m^2s^{-1}
κ	thermal diffusivity	m^2s^{-1}
ϑ	temperature	°C
ρ	density	kgm^{-3}

1 Introduction

The importance of reducing the energy demands of buildings is undeniable. Being responsible for 36% of the total CO_2 emissions in Europe and 40% of the final energy consumption (European Commission, 2020) it is impeccable to reduce this consumption to reach current climate goals, as proposed by the *International Energy Agency* (IEA) (International Energy Agency, 2013).

By combining different renewable energy sources with the latest heating technologies and already state of the art building technologies, it is possible to build zero-emission houses and even Energy-plus buildings. A building is considered an energy plus building if it annually produces more energy than it uses.

One approach to increase building efficiency and reduce CO_2 emissions is the use of compression heat pumps (HPs). They have the ability to heat and cool a building CO_2-free as they are powered by electricity. HPs are being used more frequently when a building is equipped with a low temperature heat distribution system such as floor or wall heating. Because by increasing the heat transfer area the necessary water temperature for heating can often be reduced. This makes HPs particularly attractive as they operate at a much higher efficiency when the temperature gap between source and sink is lowered. HPs are gladly combined with solar panels. This way CO_2-free heating/cooling is guaranteed throughout most time of the day. However, peak loads and domestic hot water (DHW) production still pose a problem to the efficiency of HPs.

In order to heat up water to a higher temperature level, for DHW, the electric load of an HP increases significantly. This can lead to peaks in the electric grid and cause an increase in the grid's CO_2 emissions. Therefore, a solution for hot water production with low electric loads is necessary. Combining the HP with DHW production via an integrated heat storage system should boost efficiencies and reduce the electric load for hot water generation. In this work, the integrated latent heat storage is a refrigerant (R)/ water (W) heat exchanger (HEX). In between the water and the refrigerant channels is phase change material (P). In short, this leads to the expression of RPW-HEX for the latent heat storage.

In the building sector, a lot of research has been conducted on how heat storages in buildings can improve energy efficiency and reduce peak loads. The most commonly used technology is a hot water tank to decouple DHW production from consumption. Advantages are the easy installation and the reasonable price. Its biggest disadvantage is the required space and that the thermal energy stored is sensitive. Since HPs operate only in a certain temperature range the energy density of water storage is very limited. Phase change materials (PCMs) have a high energy density in a certain temperature range, therefore, they offer themselves to be used in combination with HPs. Also, the required space can be reduced significantly by using a PCM instead of a water-only storage (Hirmiz et al., 2019). For DHW, commonly a temperature between 50 °C and 70 °C is desired. Therefore, the PCM has to melt and solidify in this temperature range. It is important to understand how the PCM behaves under different circumstances in order to fully utilise the energy the latent heat storage (LHS) can yield. Throughout this work, two experimental setups were built. One was the integrated RPW-HEX into a refrigerant circuit. The other set up consisted of small LHS.

1.1 Stand-alone mini-LHS

In the *mini-LHS,* the PCM which is used in the RPW-HEX is investigated. As the RPW-HEX is a closed unit it is impossible to determine when and where the PCM is completely melted or solidified. As PCMs can change their melting and solidification behavior depending on cooling rates and previous states, it is important to understand how the used PCM will behave in operating conditions. In addition, the heat transfer coefficient through PCMs is generally low. In order to prevent the heat storage from being limited by the low heat transfer rates, the heat transfer has to be enhanced. In literature a series of heat transfer enhancement possibilities are described like, using a fin structure or metal foams. In this work, the *mini-LHS* were tested with and without a heat transfer enhancement method and compared to each other. For a better heat distribution, metal fins were inserted into the PCM.

1.2 Integrated RPW-HEX

This thesis is part of the project *HYBUILD* conducted by the Austrian Institute of Technology (AIT) which basically aims to reduce energy demands of buildings and therefore CO_2 emissions. *HYBUILD* is divided into two climate concepts. One for a Mediterranean climate which focuses more on cooling and one for a continental climate where heating is more relevant. This work focuses on the concept of the continental climate.

The project addresses a concept that is dedicated to delivering heating energy for buildings with an electrical compression HP and at the same time DHW with the help of an integrated latent heat storage. HPs are known to work efficiently at low-temperature levels. With this concept, it is possible to produce hot water despite the low-temperature stroke of the HP.

The air source heat pump (ASHP) heats up water for heating while continuously charging the RPW-HEX. DHW will be produced by discharging the same storage with water. The RPW-HEX is integrated right after the compressor in the refrigerant cycle, using the hot exit gas. This way, the RPW-HEX is charged even when the HP operates in cooling mode during the hot season. The system was developed, simulated and experimentally tested at AIT. In this thesis, the different experimental assemblies will be described, and the results will be discussed.

1.3 Research Questions

This master thesis aims to answer the following questions:

Stand-alone mini-LHS:

1. How is the phase change behavior altered when implementing fins into the PCM?
2. How does the heat transfer change with progressing solidification?
3. Is the measurement of a heat flux sensor dependent on the state of the PCM-phase?
4. Can an optimal fin geometry be derived from the *mini-LHS* measurements, for the RPW-HEX?
5. What should be considered when using RT64 in a large storage device? How can the results of the *mini-LHS* be translated to a larger system? Does the PCM RT64 have any properties that can either enhance or limit its use in a latent heat storage for DHW production?

Integrated RPW-HEX:

1. Is the implementation and operation of the latent heat storage in an HP cycle possible from a technical point of view?
2. What challenges arise when integrating a heat storage directly into a refrigerant cycle and how can they be overcome?
3. Do surface temperature sensors on the RPW-HEX deliver reliable results?
4. How can the state of charge (SoC) of the RPW-HEX be determined?
5. Is the system capable of providing DHW under normal operating conditions?
6. What factors have the biggest influence on the performance of the overall system?
7. Is the performance of the system enhanced by implementing the RPW-HEX?

2 Theory

In this chapter, the basics of the proposed novel system, as well as state of the art technologies and constructions, are described. This includes the concepts of compression heat pumps, thermal energy storages, heat exchangers, refrigerants, and phase change of materials.

2.1 Compression heat pump

A HP is a device that converts electrical energy into heat by means of a thermodynamic cycle. The process was originally discovered in the 20th century by Rudolf Plank and is therefore often also called Plank-process. The simplest assembly of an HP consists of a compressor, two heat exchangers and an expansion valve (see left image in Figure 1). The compressor compresses a superheated refrigerant lifting it to a higher pressure level (see the right image in Figure 1). Subsequently, the refrigerant is being condensed in the condenser, providing thermal energy. After that, the already cooled down refrigerant flows through an expansion valve, reducing the pressure and therefore cooling it dramatically. Then it enters the second heat exchanger (evaporator) where it is being heated up and vaporized. From there the gas enters the compressor again and this is how an HP transports heat from a cold temperature source to a high temperature source. It is basically a reversed Carnot cycle.

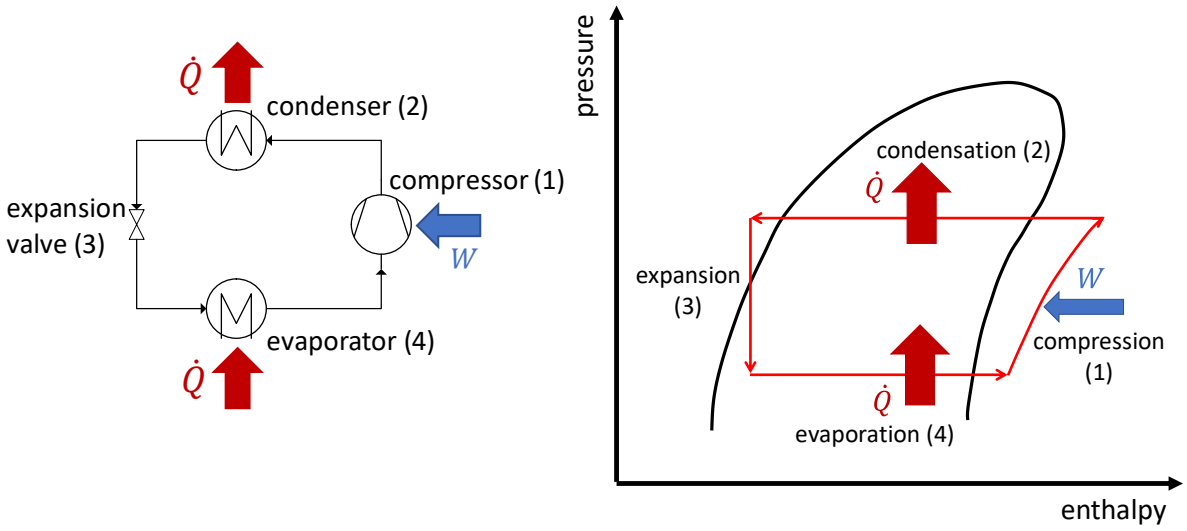

Figure 1: Left: Simple schematic diagram of a compression heat pump. The useful heat exerts from the condenser and is gained in the evaporator. Right: Pressure-enthalpy diagram of a simple heat pump cycle.

The coefficient of performance (COP) is used to describe the efficiency of the HP. It is the ratio of the useful heat ($\dot{Q}$) extracted from the HP to the total electrical work (W) introduced to the HP:

$$COP = \frac{\dot{Q}}{W} \quad \textbf{(1)}$$

An ideal HP is a reversed Carnot cycle, therefore, the highest possible COP is limited through the temperature difference of the source (T_{cold}) and the sink (T_{hot}):

$$COP_{\max} = \frac{T_{\mathrm{hot}}}{T_{\mathrm{hot}} - T_{\mathrm{cold}}} \quad \textbf{(2)}$$

This equation shows that a HP works most efficiently when the temperature gap between the source and the sink is small. In practice, this means that HPs work better where lower rather than higher temperature heat is required. The Carnot factor is never reached because heat- and friction losses occur throughout the cycle. Therefore, the real COP of any HP is significantly lower. Furthermore, heat exchangers need a temperature difference for a heat transfer and the compressor has a limited efficiency as well.

The power of a heat exchanger can be calculated with the first and second thermodynamic law. For the condenser, there are two fluid inlets and outlets. Determining the thermal power $\dot{Q}$ one fluid obtains or yields can be done with the help of the mass flow $\dot{m}$, the difference between in- and outlet temperature ΔT and the specific heat capacity c_p of the respective fluid:

$$\dot{Q} = \dot{m} * c_p * \Delta T \quad \textbf{(3)}$$

In general, HPs can be divided into two categories, depending on the exchange source the heat exchanger uses. The source can either be the surrounding air or water in the pipes of a ground heat exchanger. Ground source heat pumps (GSHP) are usually more efficient but have very high installation costs (Christodoulides et al., 2019). It should be noted that they exhibit usually longer lifetimes than ASHP. ASHP have a stable performance and an easy installation (Shen et al., 2019). Therefore, today mainly ASHPs are used for the air conditioning of buildings. Switching from an ASHP to a GSHP will be economically viable only after 20 years due to the high installation costs. (Christodoulides et al., 2019) However, the sound emissions that an ASHP produces should not be neglected.

Another problem ASHP face is the frosting phenomenon that occurs on the outside heat exchangers surface when operating in cold conditions with high air humidity. Two conditions have to be met for frost to build up. The first condition is, that the surface temperature of the heat exchanger is below 0 °C. Secondly, this surface temperature has to be below the dew point of the surrounding air. Research has shown that frosting occurs at outside air temperatures between 7 °C and -12 °C with a relative humidity higher than 60% (Shen et al., 2019). When frosting occurs the airflow is obstructed, and the heat exchanger becomes inefficient. This results in a decrease in COP and heating capacity. The performance drop occurs in the latter part of the frosting process. The mass of the deposited ice is not directly related to the performance drop (Chung et al., 2019). To prevent a major performance loss, it is necessary to defrost the heat exchanger periodically or to destroy the emerging ice. Several approaches to conduct an efficient defrost process have been investigated. For example, (Shen et al., 2019) and (Minglu et al., 2010) propose to charge an LHS which will act as heat source during the defrost process to ensure a continuous heating process and improve thermal comfort.

HPs distinguish themselves from conventional heating systems in many ways. They are more complex than traditional gas or oil boilers and therefore, need greater skills to achieve high quality installations. HPs use electricity often at peak times. This poses many challenges to the supply network when connecting a large number of HPs to the electrical supply grid. These challenges could be met with the implementation of smart grids. Further, to make HPs an environmentally friendly alternative, the electric grid needs to produce a large percentage of its electricity with renewables. Another challenge HPs face is, that they work best with a low temperature household heat distribution system. This makes it especially difficult to implement them into older existing buildings. Switching from a conventional high water-based radiator system to a low temperature system e.g. using underfloor heating is cost intensive.

There are a number of factors that influence the market of HPs in different countries. These are climate, government policy on energy and environmental issues, energy prices, availability of competing energy sources, electricity supply and generation characteristics, housing characteristics as well as history, geography and geology. For example, in England an HP system was compared to a conventional gas boiler system in terms of energy efficiency and running costs (Le et al., 2019). The HP system was not able to compete with the conventional gas boiler due to the cheap gas price, unfavorable operating conditions and an electricity mix with a very low percentage of renewables. Because of these reasons, HPs for domestic households are still a niche product in many parts of Europe (Fawcett, 2011).

Still, they are becoming increasingly popular since they are slowly becoming economically rentable and more importantly, they can be used for cooling in summer. In addition, research shows that by using HPs instead of natural gas boilers, significant primary energy savings can be made (Bianco et al., 2017), (Jarre et al., 2018). Moreover, with a growing number of renewables the carbon emission reduction is even more significant compared to conventional heating systems.

2.2 Thermal energy storages

Thermal energy storages (TES) are becoming increasingly popular since renewable energy systems found their way into the market. By decoupling production from consumption, they can enhance a system's efficiency dramatically. In doing so the heat storage has to be economically feasible, it has to have a great energy capacity and at the same time be small in size. Basically, TES can be divided into two main categories: sensible heat storages and latent heat storages. There are also chemical storages but only a few of them are commercially available, thus they will not be discussed further in the course of this work. Sensible storages have been playing an important role in the building industry for centuries, whereas latent heat storages are relatively new in comparison. Lizana et al., 2017 gives an overview of heat storage technologies and their applications for building service engineering. Latent storages like encapsulated PCM inside the building envelope are being used as passive applications for heating and cooling. Small PCM storages can be used for solar energy storage.

2.2.1 Sensible storages

Sensible heat storages are based on elevating the temperature of solid or liquid material and releasing the thermal energy by decreasing the temperature when it is required. Therefore, the storage capacity is directly related to the specific heat capacity and the volume and density of the materials. The amount of stored heat can be expressed as:

$$Q = \rho * V * c_p * \Delta T = m * c_p * \Delta T \quad \textbf{(4)}$$

Where Q denotes the stored heat, c_p the specific heat capacity, ΔT the temperature difference between the initial and the current temperature, ρ the density and V the volume. An effective sensible storage material should, therefore, have a high specific heat capacity and high density. In addition, it should be inexpensive, have high thermal conductivity and be easy to store.

In this aspect, sensible heat storages have been used for centuries in buildings. The energy is stored by sensible heat of the materials in the building envelope reducing indoor temperature fluctuations and delaying air temperature minima and maxima. Heavy envelope constructions can reduce heating energy demand by about 30% compared to lightweight envelope constructions (Ferrari,

2007). Of course, the storage capacity can be enhanced by technical solutions like an external insulation.

Another very common sensible heat storage is a hot water tank. Hot water tanks are used to decouple hot water consumption from production especially in combination with solar systems (Furbo, 2015). Together with solar collectors, they can reduce power loads due to DHW production significantly. Advantages are the easy installation and the reasonable price. The main disadvantage is the required space for such a tank.

2.2.2 Latent heat storage

Latent heat storages store thermal energy in a medium which undergoes a phase change. Thus, they use the enthalpy of fusion/solidification to store energy. The enthalpy difference between solid and liquid state is usually a lot higher than the enthalpy difference of sensible heating in common temperature ranges of building applications. For example, the specific enthalpy difference from solid to liquid in water is around 330 $kJkg^{-1}$. The sensible specific enthalpy difference of water is 4.2 $kJkg^{-1}K^{-1}$. Therefore, water would have to be heated up by 78.5 °C to store the same amount of thermal energy as stored in the phase change from ice to water. This leads to very high energy densities for latent TES and thus, compared to sensible storages, the volume can be reduced dramatically.

PCMs can roughly be divided into two groups: organic and inorganic PCMs. Generally, organic PCMs are chemically and thermally stable, non-corrosive to metals and recyclable. On the other hand, they have a bad thermal conductivity, they are mostly flammable, and their phase change enthalpy is, in general, lower than those of inorganic PCMs. Inorganic PCMs are of low cost, have high phase change enthalpies and better thermal conductivity. On the contrary, they are corrosive and lack thermal stability and require the use of nucleating agents to minimize subcooling (Farid et al., 2004; Rady, 2009). Up to date, researchers have not found a PCM that satisfies all chemical, physical and economical demands (Elias and Stathopoulos, 2019).

The phase change of PCMs happens at a certain temperature. This poses new requirements when choosing a latent TES as the PCM must be suitable for its use in terms of having the right melting/solidification temperature. But the narrow field of application with regard to temperature also has advantages. Stropnik et al., 2019 presents the main advantages of a latent heat storage which are reflected primarily in combination with HPs because HPs operate most effectively in a certain temperature range.

For domestic households, water temperatures ranging from 20 °C to 80 °C are usually needed. Hence, PCMs which melt in this temperature range are suitable. *RUBITHERM GmbH* offers a wide range of paraffin waxes as PCMs with melting temperatures between -9 °C and 100 °C. One of these is RT64, which will be investigated in the course of this work.

2.3 Heat exchangers

Heat exchangers are distinguished by the phase of the media that exchanges heat (solid, liquid, gaseous) and by their geometry. The heat exchange can either happen directly or the two mediums are separated from each other by a separator. In this case, the heat has to be conducted through a solid material as well. The second law of thermodynamics states that heat only flows from a hot source to a cold sink to reach thermal equilibrium unless external work is introduced to the system. Therefore, a heat exchanger only works if the two media have different temperatures. A HP consists of at least two heat exchangers, where the refrigerant condenses and where it is evaporated.

2.3.1 Plate heat exchanger

The condenser is a refrigerant to water heat exchanger and is often realized as a plate heat exchanger (see Figure 2). The plates are mainly made of aluminum, stainless steel or titanium (Guo et al., 2015). The space between the plates is mostly sealed with rubber gaskets.
Compared to shell and tube heat exchangers, plate heat exchangers have several advantages. Firstly, they have a large surface area per unit volume and high heat transfer efficiencies. This makes them small in size and contributes to more heat recovery. The heat exchange area can be increased at will by simply adding more plates to the stack. Corrugated plates can further enhance the heat transfer coefficient by forcing the liquids into turbulent flows (Guo et al., 2015).
Due to the small hydraulic diameters, this kind of heat exchanger exhibits serious fouling problems. Another disadvantage is the high capital cost (Picón-Núñez and Robles, 2005).

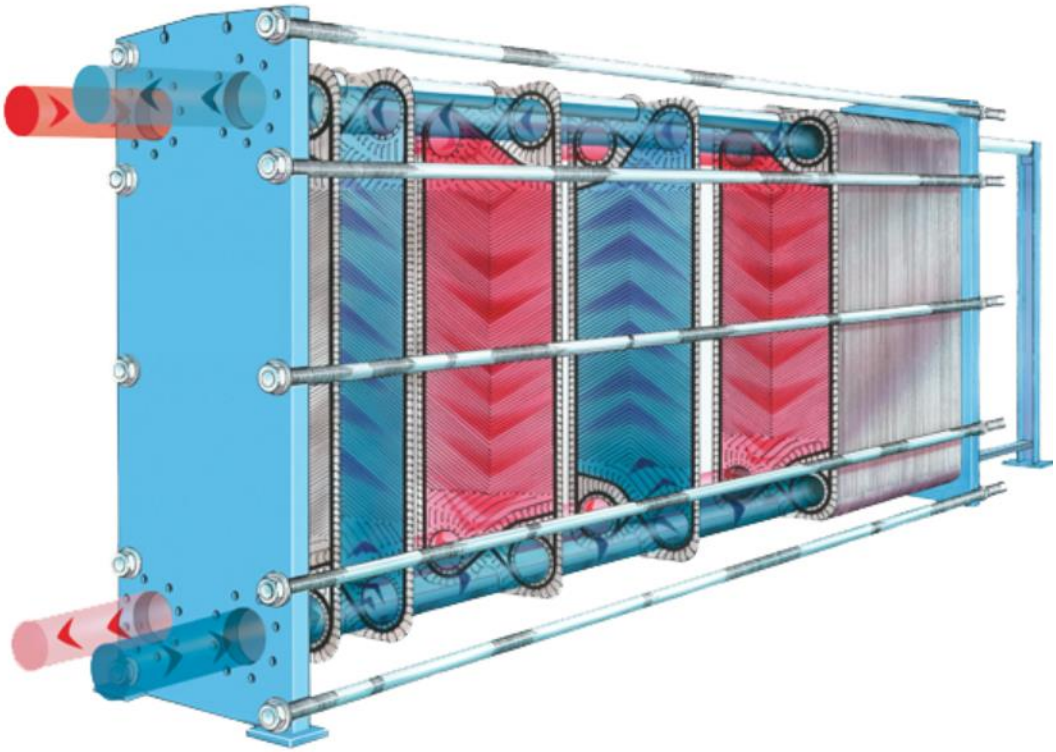

Figure 2 Schematic scheme of a plate heat exchanger (“Plate heat exchanger,” 2020). The red stream denotes the hot fluid and the blue steam the cold fluid.

2.3.2 Finned tube heat exchanger

In an ASHP the evaporator is a liquid to air heat exchanger where the surrounding air heats up the refrigerant and is usually realized as a fin tube heat exchanger (see Figure 3). To maximize the heat transfer, the surface of the tubes is extended by metal fins or plates. Through the tubes flows the refrigerant and exchanges heat with air that passes the fined tube surface in a cross-counter-flow. With small tube diameters, the heat exchange between refrigerant and metal can be enhanced and the necessary amount of refrigerant in the system is reduced which is desired when using environmentally unfriendly refrigerants. But at the same time, the pressure drop rises which has to be compensated by the compressor. The air flow is driven by a fan through the fins. The fin structure can be wavy or slit which would also enhance the heat transfer but again the pressure drop has to be compensated by the fan. In addition, plain fins have higher reliability when it comes to long term operation (Tang et al., 2019).

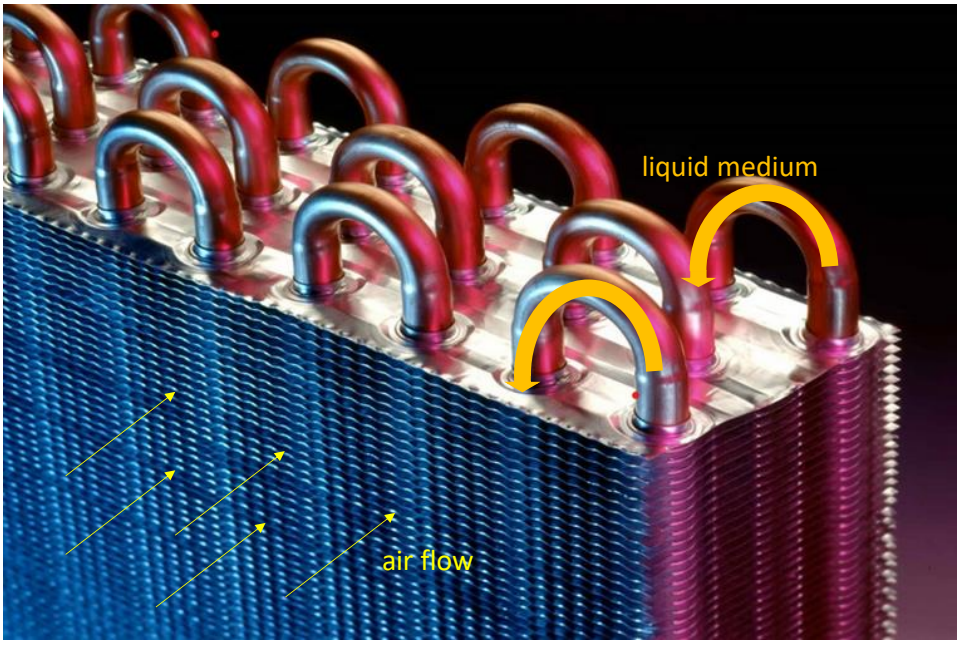

Figure 3 Picture of a finned tube heat exchanger. (“Air-water heat exchanger,” 2020)

Depending on the direction of the air flow plate heat exchangers are distinguished into upright positioned heat exchangers or table heat exchangers. The first is used e.g. in car coolers and the air flows from the front to the back. The latter is a lying heat exchanger. The air flows from the bottom to the top or vice versa.

2.4 Refrigerants

The most commonly used refrigerants in the past were chlorofluorocarbons (CFCs). They have been replaced by hydrochlorofluorocarbons (HCFCs) in the 1990s and 2000s because of their severe environmental impacts. As HFCFs contain chlorine they are also harmful for the environment. Based on the 1997 Kyoto Protocol, the applications of HCFC refrigerants have been restricted due to their high global warming potentials (GWPs) and high ozone depletion potential (ODP). They can be used until 2030 in developed nations and in developing countries until 2040. In order to remove the chlorine from the refrigerants, hydrofluorocarbons (HFCs) were considered as refrigerants. They still have high GWPs, but they do not deplete the ozone layer. The most common HFC used in air conditioners is R-410A. Another one is R-32 which is better than R-410A in terms of GWP. The most environmentally friendly refrigerants on the market are hydrocarbons (HCs). In Table 1 some selected refrigerants are listed.

Table 1 Common refrigerants and their ODP as well as GWP (Linde Gases AG, 2020).

Type	*Product Name*	*ODP*	*GWP*
CFC	R-12	1	10900
	R-502	0.33	4657
HCFC	R-22	0.055	1810
	R-401A	0.033	1182
HFC	R-410A	0	2088
	R-32	0	675
HC	R-600a	0	3
	R-744	0	1

The perfect refrigerant should fulfill the 4 key criteria of environment, energy efficiency, safety and economy. Each refrigerant has strong and weak points, which also vary depending on the application. From a technical point of view, HFCs have better thermodynamic and thermophysical properties than HCs. Many major air conditioning manufacturers have determined that R-32 is the optimum choice for their products. R-32 has zero ODP and a relatively low GWP. It is a single component refrigerant and therefore easy to handle. The toxicity level is low, and it has a high refrigeration capacity and good thermal conductivity. In addition, its energy efficiency is superior. A R-32 HP with optimized heat exchanger design exhibited a higher performance improvement than that of a conventional R-410A HP (Kim et al., 2020). The biggest disadvantage of R-32 is, that according to ISO 817:2014, it is mildly flammable. That means the burning velocity is below 10 cm per second. This excludes the use of R-32 in some applications.

HC refrigerants rarely have the thermodynamic properties close to HFC refrigerants. For example, R-744, which is CO_2, is not flammable and has a minimal environmental impact. Obstacles for this refrigerant are the high pressure and the low critical temperature. Using this refrigerant in a refrigerant cycle needs special equipment designs. An alternative to match the desirable properties would be a mixture of two HC refrigerants (Mohanraj et al., 2011). But HC-mixtures are highly flammable which limits their use (Palm, 2008).

2.5 Numerical treatment of the phase front

To calculate the heat flux through the PCM between two walls with steady temperatures, the following approach was chosen. In between two walls with steady temperatures, a phase front emerges (see Figure 4).

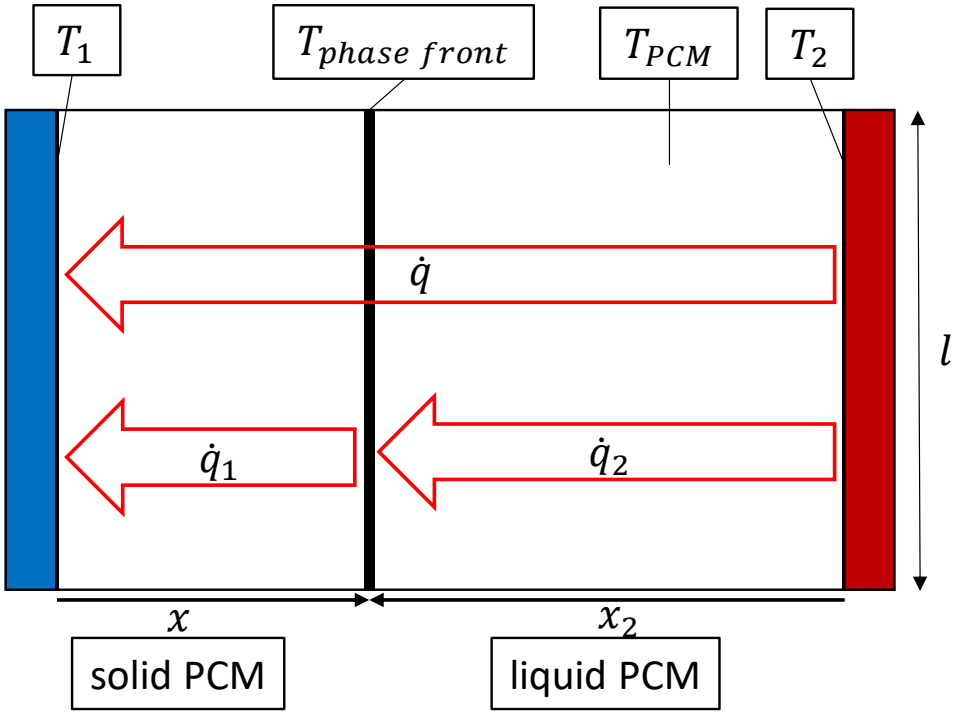

Figure 4: Visualization of the heat transfer from the hot wall to the cold wall with a phase front.

The phase change temperature $T_{\text{phase front}}$ is assumed to be of constant value. The thickness of the solid PCM can be described with $\Delta x = x - x_0$. As x_0.will always be zero the thickness of the solid phase will be described with x in the further course of this work.

The heat flux can be described with:

$$\dot{q} = \alpha * (T_2 - T_1) \quad \textbf{(5)}$$

α being dependent on the Fourier heat conduction in solid-state and natural convection as well as conduction in the liquid state. In a first step the heat flux is assumed to be constant between the fins:

$$\dot{q} = \dot{q}_1 = \dot{q}_2 \quad \textbf{(6)}$$

Then the heat flux can be described with two equations. In the liquid phase, natural convection is the dominant heat transfer mechanism. The contribution of conduction in the liquid phase is not considered because the heat transfer coefficient λ is unknown for the PCM that is investigated throughout this work. Usually, the conduction through a liquid medium is by an order of magnitude lower than convection, however, PCM materials have not been investigated in such detail:

$$\dot{q}_2 = \alpha_2 * (T_2 - T_{\text{phase front}}) \quad \textbf{(7)}$$

With α_2 is being derived from:

$$\alpha_2 = \frac{\text{Nu} * \lambda}{l} \quad \textbf{(8)}$$

The Nusselt number Nu is a function of the Rayleigh Number Ra and the function $f_1(\mathrm{Pr})$ in the range of $\mathrm{Ra} = 10^{-1}$ to $\mathrm{Ra} = 10^{12}$ (Verein Deutscher Ingenieure, 2010):

$$\mathrm{Nu} = \left\{0.825 + 0.387 * [\mathrm{Ra} * f_1(\mathrm{Pr})]^{1/6}\right\}^2 \quad \textbf{(9)}$$

l denotes the characteristic length. In transition flows between laminar and turbulent this equation is not exact ($10^8 \leq \mathrm{Ra} \leq 10^9$) but should still be sufficient for engineering applications.
The function $f_1(\mathrm{Pr})$ considers the effect of the Prandtl number in the range $0.001 < \mathrm{Pr} < \infty$ (Verein Deutscher Ingenieure, 2010):

$$f_1(\mathrm{Pr}) = \left[1 + \left(\frac{0.492}{\mathrm{Pr}}\right)^{9/16}\right]^{-16/9} \quad \textbf{(10)}$$

$$\mathrm{Pr} = \frac{\nu * \rho * c_p}{\lambda} \quad \textbf{(11)}$$

With ν being the kinematic viscosity, ρ the density and c_p the specific heat capacity. The Rayleigh number Ra is calculated as follows:

$$\mathrm{Ra} = \frac{g * l^3 * \beta * (T_2 - T_{\mathrm{PCM}})}{\nu * \kappa} \quad \textbf{(12)}$$

With g being the gravitational constant, l the height of the fin where the natural convection occurs, κ the thermal diffusivity and β the thermal expansion coefficient which is idealized with:

$$\beta = 1/T_{\mathrm{PCM}} \quad \textbf{(13)}$$

T_{PCM} denotes the temperature of the liquid PCM. To simplify calculations, it is assumed that the temperature in the liquid PCM is uniform. The experiments, however, will reveal that this is not the case.

For the PCM RT 64 that is investigated the physical properties of the liquid PCM like viscosity and density are only known at a temperature of 80 °C. Therefore, it is not possible to calculate the heat flux in the liquid PCM ($\dot{q}_2$) accurately.

It is often described in literature that convection is the driving force during heat transfer in a liquid medium and that the heat transfer in a medium is, therefore, higher in the liquid state than in the solid-state (Jevnikar and Siddiqui, 2019; Shokouhmand and Kamkari, 2013; Sparrow et al., 1978; Sun et al., 2018, 2016). Hence, in this thesis, a correlation between the amount of solid phase and the heat flux is being investigated. The heat flux should rise with decreasing width of the phase front. This way the heat flux can be described as a function of the cold wall temperatures and the width of the solid phase:

$$\dot{q} = f(T_1, T_{\text{phase front}}, x) \quad \textbf{(14)}$$

Furthermore, if the conduction by the solid PCM is seen as the limiting factor for the heat transfer ($\dot{q} = \dot{q}_1 = \dot{q}_2$), the heat flux can be described by the following equation:

$$\dot{q}_1 = \lambda * \frac{T_{\text{phase front}} - T_1}{x} = \dot{q} \quad \textbf{(15)}$$

This way, the heat flux through the liquid PCM is completely ignored. The temperature of the phase front is considered constant but has different values depending on the phase state of the PCM (melted or solidified). RT64 has its highest melting enthalpy between 63 °C and 65 °C and its highest solidification enthalpy between 61°C and 64°C. Therefore, it is assumed that $T_{\text{phase front}}$ will have 64 °C when the PCM is being melted and 62 °C when it is being solidified. The thermal conductivity λ is provided by *RUBITHERM* with 0.2 W m^{-1} K^{-1}.

By measuring the thickness of the phase front as well as the heat flux we can transform the equation to:

$$\lambda = \frac{\dot{q} * x}{T_{\text{phase front}} - T_1} \quad \textbf{(16)}$$

If the heat transfer coefficient λ is constant, the heat flux $\dot{q}$ has to decline with a growing phase front x.

This numerical problem could be described as a Stefan problem. However, because of the missing thermodynamic properties of the PCM, the Stefan problem will not be addressed in this thesis.

3 Experimental setups

In this chapter both experimental setups are described, and the methods of data acquisition are explained.

3.1 Stand-alone mini-LHS

This experimental setup aims to investigate the phase change behavior of RT64 and how the heat transfer depends on the phase front between two walls with different temperatures. Each *mini-LHS* has two water inlets and two outlets. Through these, heat is supplied to and dissipated from the *mini-LHS*. In Figure 5 and Figure 6 photographs of the *mini-LHS* with dimensions are given. The two *mini-LHS* have the exact same dimensions. The only difference are the additional aluminum fins in between the two main fins which are being heated/cooled by water. In the further course of this work, these *mini-LHS* samples are going to be referred to as the *empty-sample* and *fin-sample*.

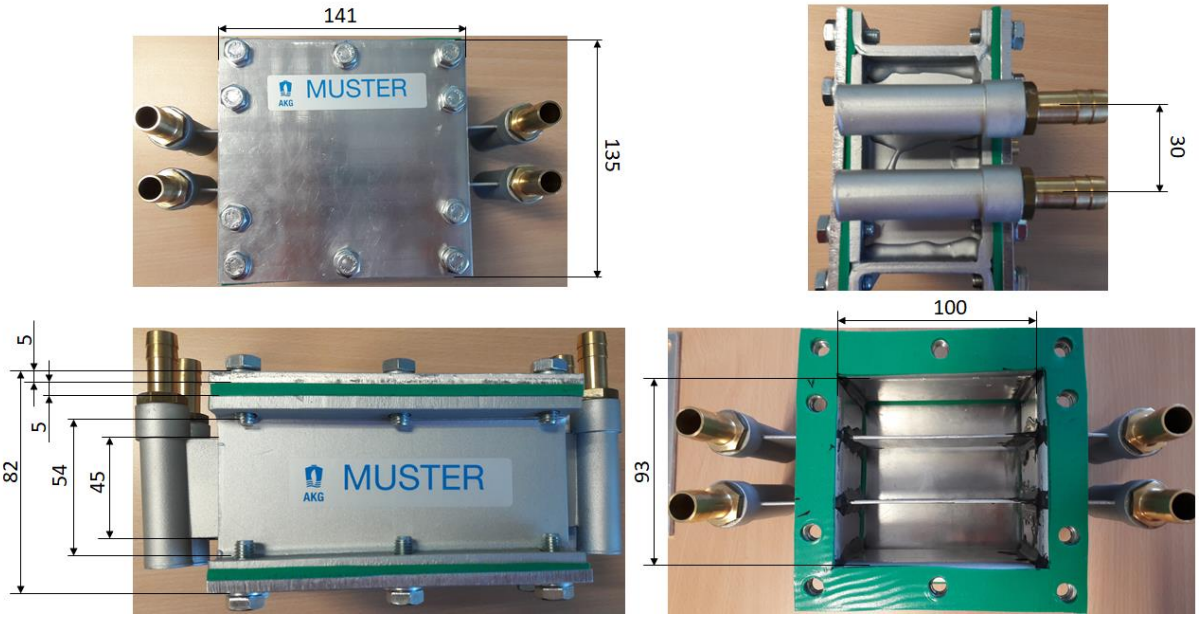

Figure 5: Representation of the *empty-sample* with dimensions. All dimensions are given in millimeters.

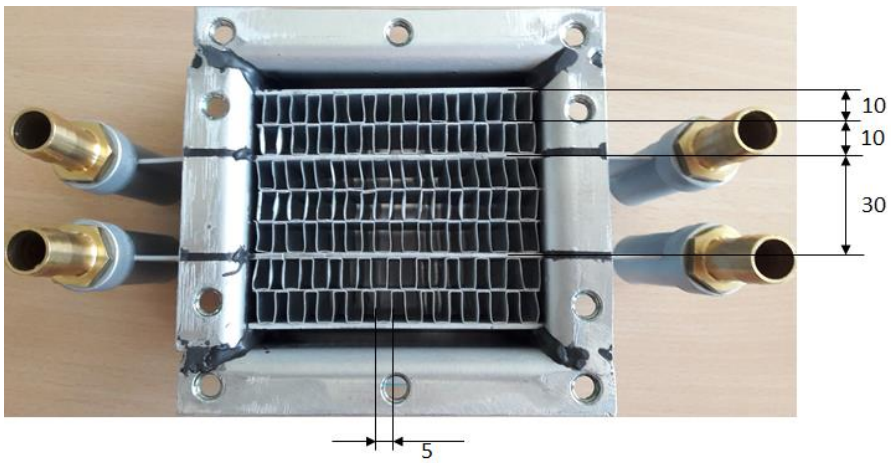

Figure 6: Representation of the *fin-sample* with dimensions. All dimensions are given in millimeters.

On each inlet and outlet, a temperature sensor (PT-100; 1/3DIN; 2x10mm, 1/3 Class B: dT = ± (1/3*(0.30 °C + 0.005 T))) is mounted. To measure the temperature distribution in

the PCM, temperature sensors (PT-100, DIN EN 60751, Class A, 1x50mm, -50°C to 250°C) are inserted into the PCM. Figure 7 is a schematic representation of the experimental setup. The water temperature is controlled with a *JULABO* (Type: FP51-SL) for each fin. The temperature sensors TI-51, TI-52, TI-53, and TI-54 measure the water temperature at the inlets and outlets respectively. The water mass flow is set as high as 380 lh^{-1} so that the inlet temperature no longer differs from the corresponding outlet temperature. This way it is ensured that the fins have virtually constant temperatures. Therefore, TI-51 and TI-53 are referred to as "hot fin temperature" (T_2) and TI-52 and TI-54 are referred to as "cold fin temperature" (T_1) in the further course of this work.

$$T_1 = T_{\text{cold fin}} = TI51 = TI53 \quad \textbf{(17)}$$

$$T_2 = T_{\text{hot fin}} = TI52 = TI54 \quad \textbf{(18)}$$

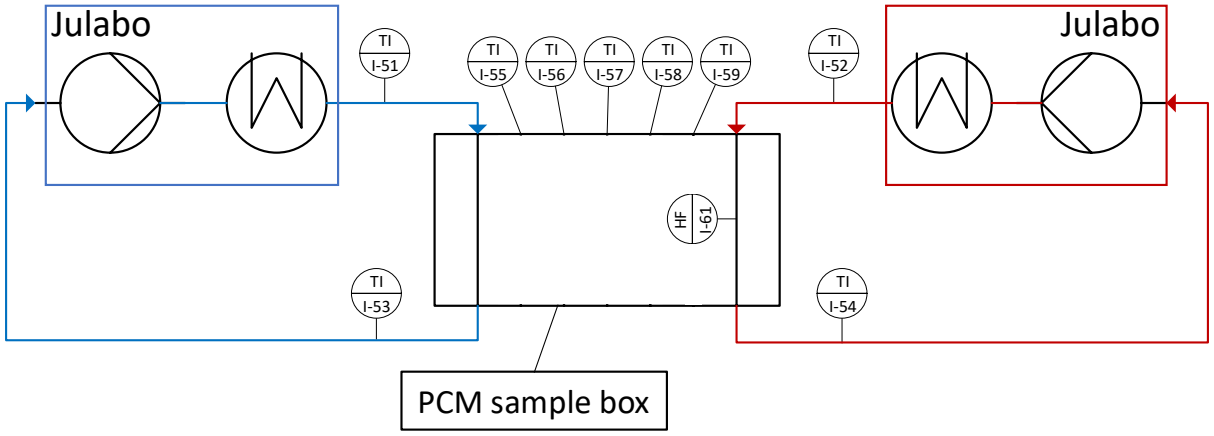

Figure 7: Schematic structure of the experimental setup. The colors blue and red represent the cold and the hot water cycle respectively.

The heat transferred through the PCM from one fin to another is measured with a heat flux sensor (HF61) (gSKIN-XM 27 9C. 4x4 mm) which is mounted onto the hot fin (Figure 8). The storage is placed inside a box and surrounded with expended glass from *GEOZELL* (DiBt Z-23.11-114, $\lambda = 0.07\ Wm^{-1}K^{-1}$) as thermal insulation. Above the *mini-LHS*, a camera was mounted to make images from which the thickness of the phase front can be extracted. The lid of the storage tank consists of a 10 mm thick acrylic glass plate so that one can observe the phase front during solidification and melting.

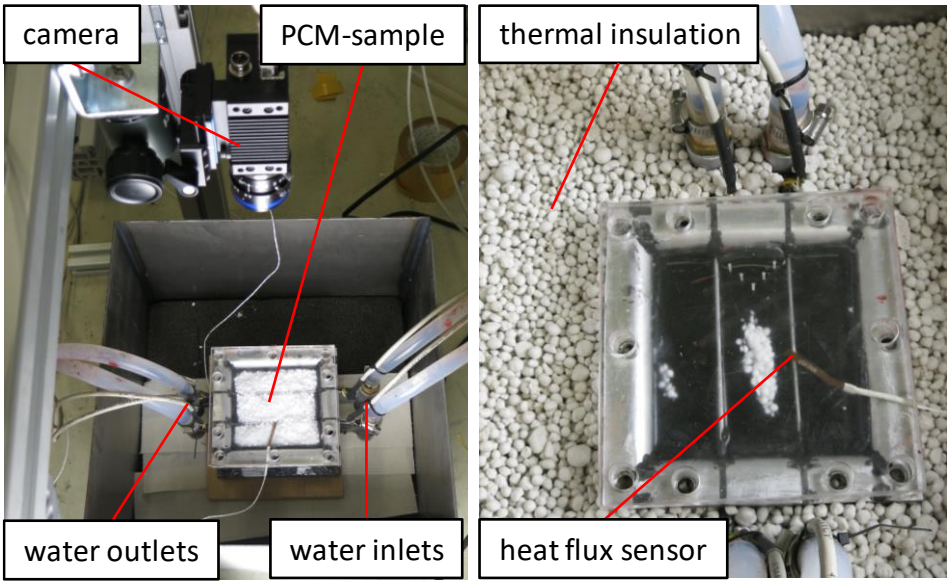

Figure 8: Left: Picture of the experimental setup. Right: The *mini-LHS* is being surrounded by expanded glass as thermal insulation. Heat Flux sensor gSKIN-XM 27 9C is glued to one of the fins, facing the second fin.

In Figure 9 the location of the heat flux and temperature sensors is provided. TI-55 to TI-59 are the rod temperature sensors that measure the temperature inside the PCM in between the two fins. They are mounted at a distance of 5 mm to each other. The rod temperature sensors have a length of 35mm. Since they are inserted through the acrylic glass plate which is 10 mm thick with a gap of 5 mm between the PCM and the acrylic glass plate, the temperature sensors reach 20 mm deep into the PCM. The space between the fins in the *fin-sample* is divided into 3 parts. Therefore only 3 rod temperature sensors are being used for experiments with the *fin-sample*.

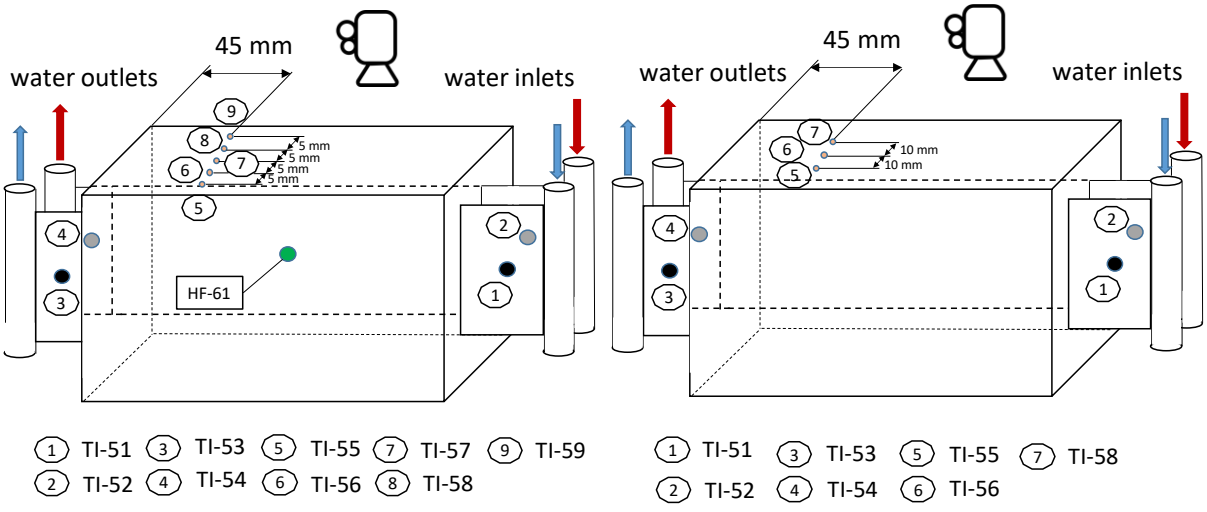

Figure 9: Schematic illustration of the LHS with the location of the sensors. Left: *Empty-sample*. Right: *Fin-sample*.

The pictures from the camera are being analyzed with PYTHON. The thickness of the solid phase front is extracted from the images as represented in Figure 10.

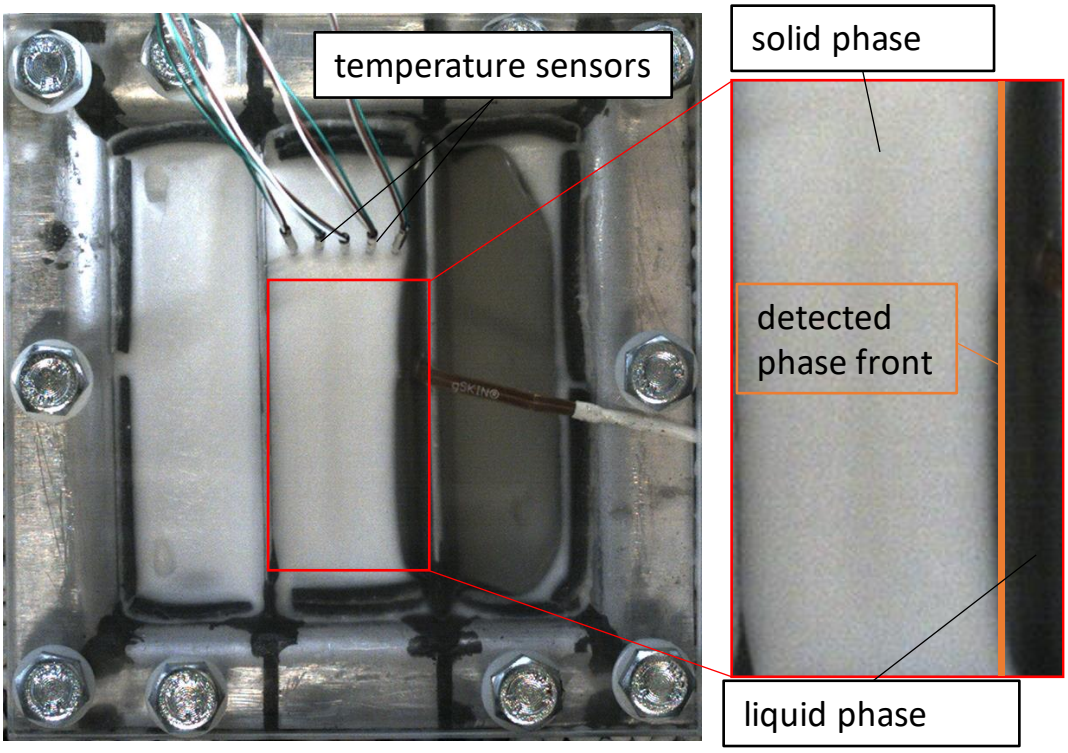

Figure 10: Picture of the *mini-LHS* with PYTHON phase front detection (right).

3.1.1 Phase Change Material (PCM)

RT64 from *RUBITHERM GmbH* is used as PCM. This particular PCM has the advantage of being very resilient over a long period of cycles. The main disadvantage is that it gains a lot of volume when melted and it has low thermal conductivity. The thermal conductivity λ is around 0.2 $Wm^{-1}K^{-1}$. The *mini-LHS* are filled with 350g of RT64.

RT64 has different melting and solidification behavior. As we can see in Figure 11 the partial enthalpy is different for heating and cooling. The PCM melts around 64 °C while it completely freezes at 61 °C.

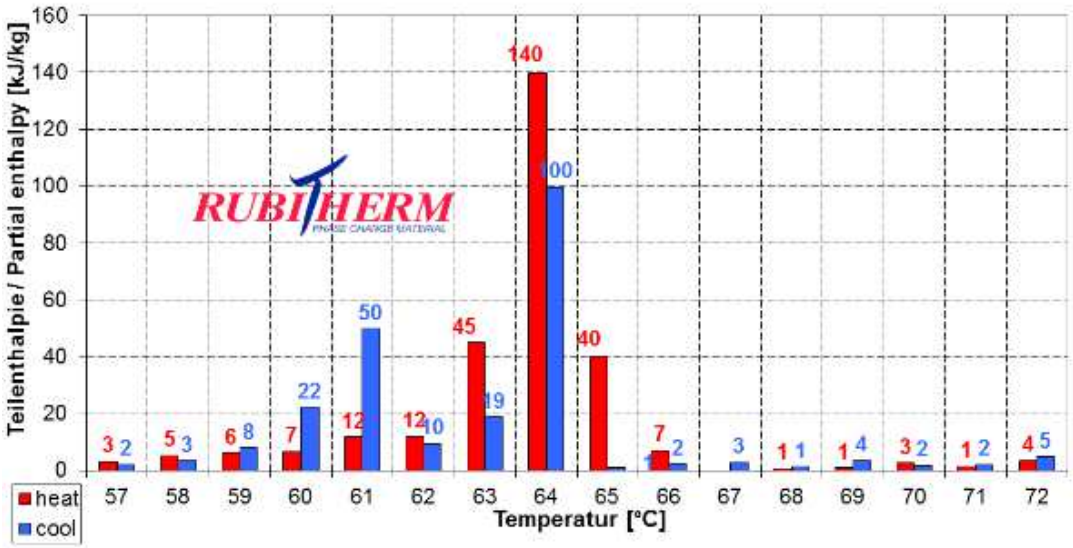

Figure 11: Partial enthalpy distribution of RT64HC. (Rubitherm, 2020)

3.2 Integrated RPW-HEX

The experimental setup for the HYBUILD project was built in two separate climatic chambers. One chamber represented the indoor environment and the other the outdoor environment. Figure 12 shows the experimental setup of the HP in the indoor chamber. It consisted of the HP, the RPW-HEX and the measurement points as well as water connections to the AIT infrastructure and obviously the refrigerant connection to the outside chamber where the evaporator is located.

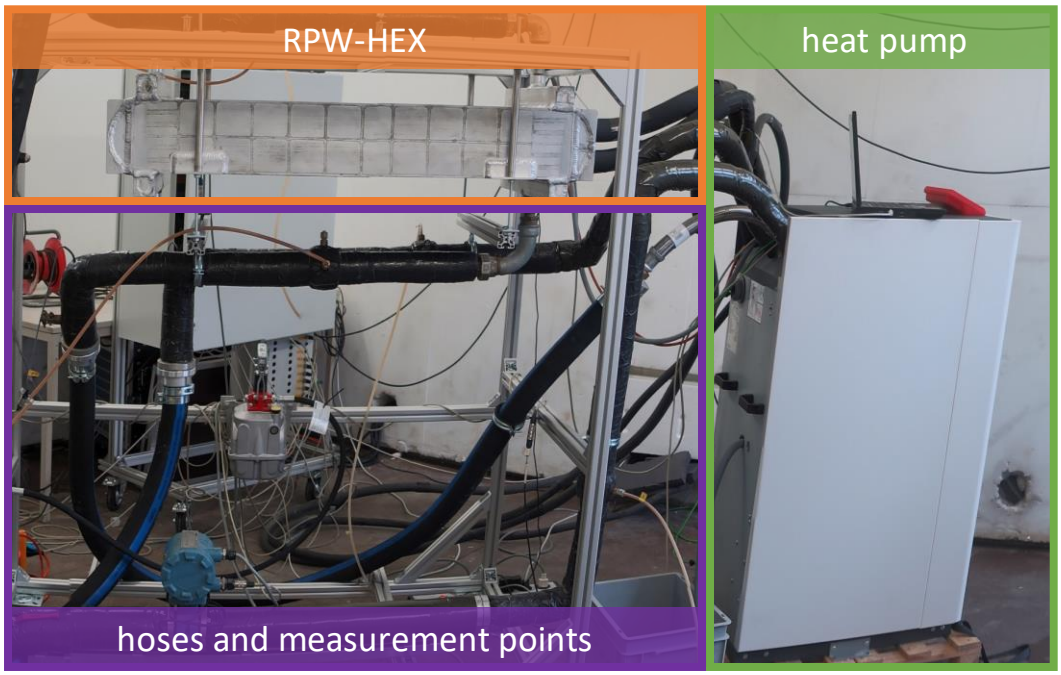

Figure 12 Picture of the experimental setup with integrated RPW-HEX.

3.2.1 Compression heat pump

The HP tested in the pursuit of this work is manufactured by *OCHSNER*. It is a prototype and has been specially manufactured for combination with a heat storage and the use of R-32 refrigerant. The HP is a water/air type HP and comprises an inside unit and an outside unit. The compressor is driven by a variable speed drive and allows for AC and DC-supply through an AC/DC converter. Figure 13 shows a simple schematic representation of a frequency converter. A simple frequency converter works in two steps: The conversion from alternating current (AC) to direct current (DC) and then from DC to AC again. These two steps are connected by a DC link. The frequency converter, which is connected to the experimental setup supplies direct current to the DC link. This made it possible to operate the HP with AC and DC.

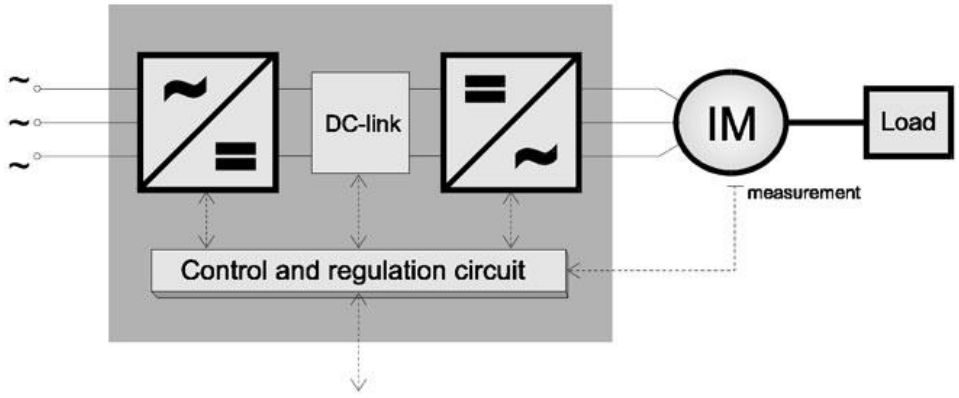

Figure 13: Schematic of a frequency converter ("Frequenzy converter," 2020).

3.2.1.1 *Refrigerant*

The refrigerant used by the HP is difluoromethane, also known as R-32. Its flashpoint is at -51,6 °C and the melting point is at -136 °C. In this experimental setup, the R-32 will not reach temperatures higher than 105 °C and pressures higher than 35 bar. The total amount of refrigerant in the cycle accounts to 3.9 kg.

3.2.2 RPW-HEX

The RPW-HEX was built by *AKG Thermal Systems*. It weighs a total of 160 kg whereby the aluminum accounts for 115 kg, the PCM for 40 kg and water for 5 kg.

Water and refrigerant flow through micro channels respectively. Water and refrigerant channels are separated by a PCM channel (see Figure 14). The channels for water and refrigerant are 2 mm wide whereas the channels where the PCM is stored are 7 mm thick. In total there are 42 PCM channels. The RPW-HEX is divided into two levels. On one side, water and refrigerant are redirected. Refrigerant enters the RPW-HEX on the upper level and leaves it on the lower level. The water flows in the opposite direction.

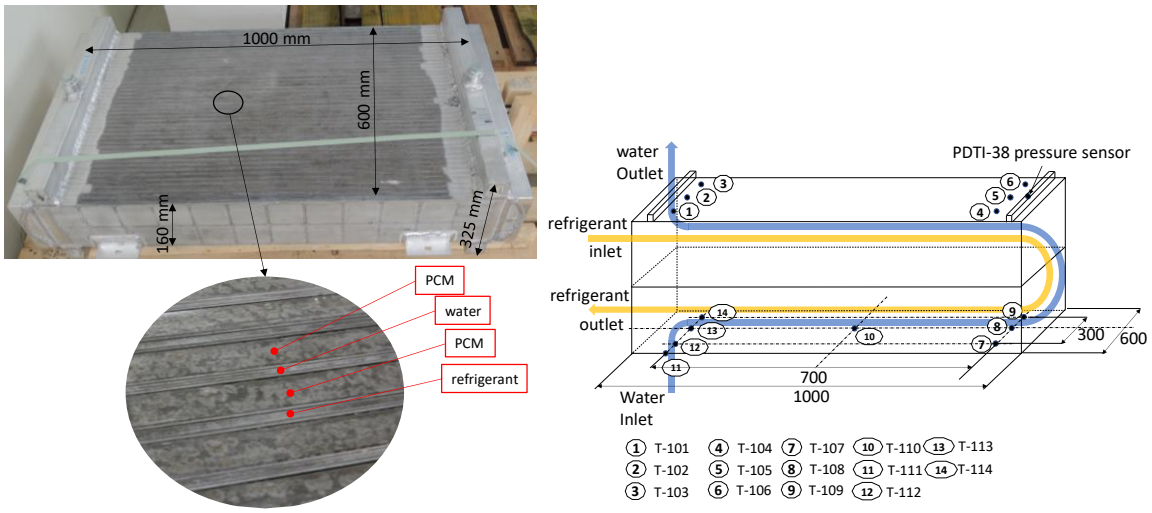

Figure 14: Left: Picture of the RPW HEX with close up of the channels. Right: Schematic representation of the RPW-HEX with location of the measurement points.

Directly onto the aluminum surface of the storage, 14 temperature sensors (RS PRO PT100 thin film detectors, 2 x 10mm, class A type 362-9799) were mounted. The location of these sensors is shown in Figure 14 on the right. To ensure proper functionality of the sensors the surface was cleaned first (see Figure 15). After that, a heat-conducting paste was put on the surface (see Figure 18). The sensor was stuck into the paste and fixated onto the aluminum with an electrically insulating and high-temperature resistant tape (see Figure 16). To ensure good attachment duct tape (Tesa extra power Universal, 50 mm) was used (see Figure 19). After this process, the whole storage was insulated using Armaflex with 32 mm thickness (see Figure 17). The cables from the temperature sensors were routed through the insulation (see Figure 20). Each sensor was mounted onto a channel filled with PCM. This way, it was assumed that the temperature in the PCM can be inferred rather than the refrigerant or water temperature.

Figure 15: The surface where the temperature sensor is applied, is cleaned.

Figure 16: Temperature sensor is attached to the surface with thermal resistant and electrical insulating tape.

Figure 17: Armaflex (3,2 cm) is used to insulate the whole RPW-HEX.

Figure 18: Heat conduction paste is applied onto the surface.

Figure 19: Duct tape is used to ensure good fixation.

Figure 20: The RPW-HEX is completely insulated, cables from the temperature sensors were routed through the insulation.

The pressure sensor (PDTI-38) is mounted on the top of the RPW-HEX as represented in Figure 21. It is attached to the PCM section to capture the change in pressure caused by the volume displacement of the PCM. The sensor is capable of measuring pressures between -600 and +600 mbar.

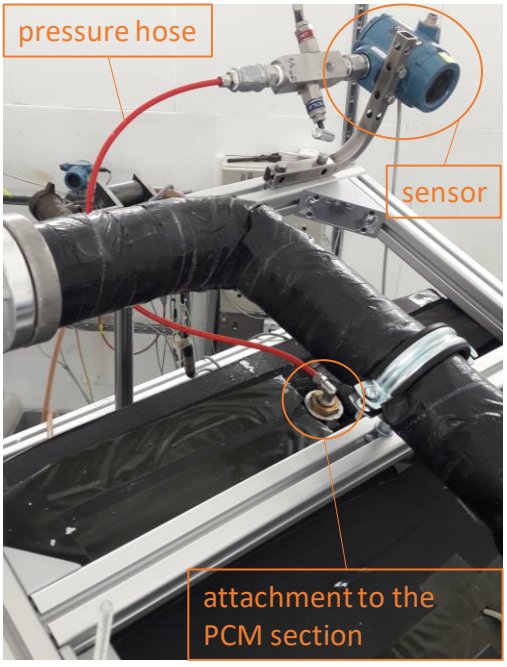

Figure 21 Pressure sensor PDTI-38 attached to the PCM section of the RPW-HEX.

The RPW-HEX is mounted onto a framework that enables it to be tilted up to 45° (Figure 22). Because the compressor ran dry in the first few experiments (see chapter Integrated RPW-HEX experiments4.2) it was decided to operate the HP with the RPW-HEX tilted upwards.

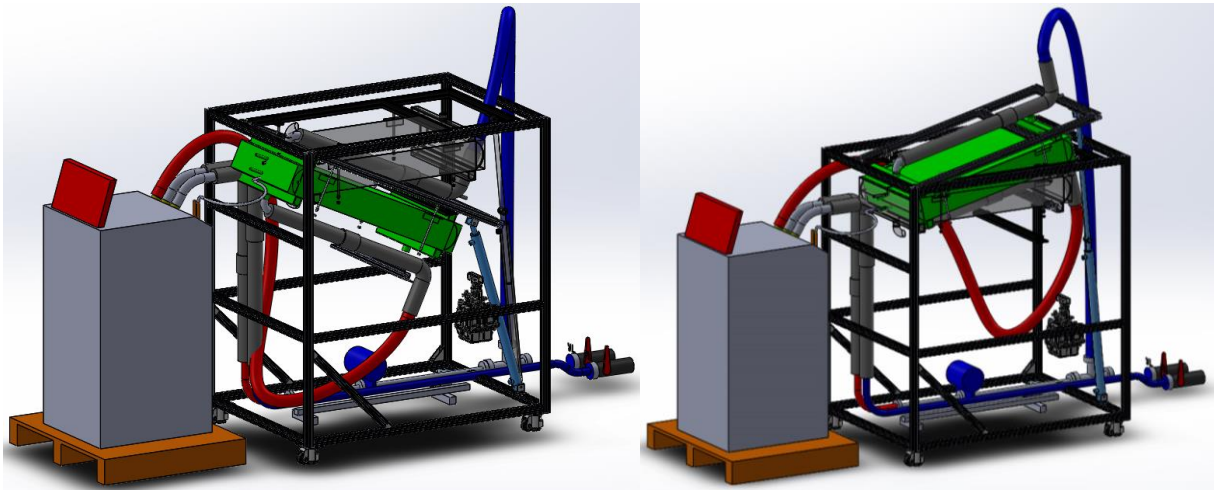

Figure 22 Representation of the experimental setup with the RPW-HEX tilted downwards (left) and upwards (right).

3.2.3 DC generator

For some tests, a DC generator is used to power the compressor of the ASHP. The DC generator works as a standalone unit and is equipped with sensors for recording the electrical power and energy consumption. Electrical power is supplied by two serial Regatron TOP Con: TC.P.16.600.400.S. It is operated with an individual control system and the DC voltage, current and electrical power are recorded every second and saved in a CSV file.

3.2.4 Evaporator

As already mentioned, the evaporator is located in a climatic chamber where ambient conditions are simulated. The evaporator is mounted on top of a scale to measure weight differences invoked by the accumulation of frost on the heat exchangers surface (Figure 23).

Figure 23: Evaporator inside the climatic chamber is mounted onto a scale to measure changes in weight.

The heat exchanger of the evaporator is a micro channel finned tube heat exchanger. Figure 24 shows the heat exchangers surface. The fins are wavy to enhance the heat transfer with the air. The fan which is located on the top of this table heat exchanger blows the air from the top to the bottom through the metal fins.

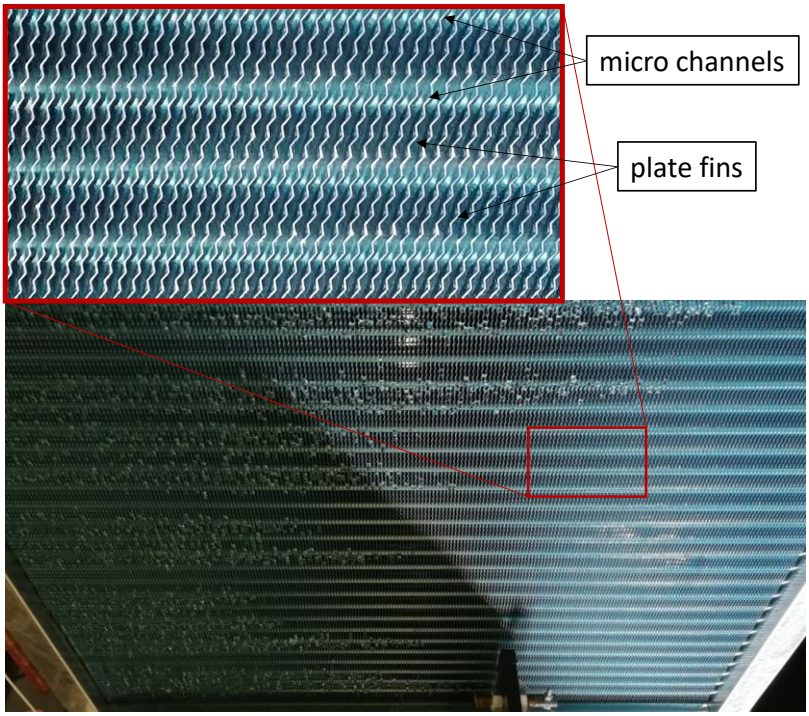

Figure 24 Picture taken from underneath the evaporator showing the micro channel finned tube heat exchanger surface.

3.2.5 Assembly

The experimental setup can be divided into three main parts. The RPW-HEX, which is described in chapter RPW-HEX, the water cycle, and the refrigerant cycle (see Figure 25).

Starting with the compressor ① the refrigerant is being compressed and the temperature is lifted to a maximum temperature of 103 °C. Valves V-4 and V-6 are opened and valve V-5 is closed at all times during operation, forcing the refrigerant to flow through the RPW-HEX. The hot gas charges the RPW-HEX ②. After that, the refrigerant passes the 4-way-valve ③ and flows through the condenser ④ where it is being cooled below its dew point. To ensure that the refrigerant is in a single-phase state before entering the expansion valve ⑤, it runs through a heat exchanger which cools it even further. The same heat exchanger warms up the liquid refrigerant after the expansion valve. After having passed the evaporator ⑥, the refrigerant flows back to the compressor. In case the exhaust gas of the compressor becomes too hot, part of the liquid refrigerant is being piped directly back from the condenser exit to the compressor through the liquid injection valve ⑦. Without being evaporated it cools the already evaporated steam in front of the compressor down. The compressor is able to handle the refrigerant in a two-phase state as long as the liquid share is relatively small.

To simulate the heating and DHW water needs of a building, water can be provided from the lab at AIT at a temperature range of 5 °C to 70 °C and at flow rates between 380 and 2230 lh^{-1}. For real operations, the supply water temperature for the HP system will be between 20 °C and 35 °C. To cover heating demands this water is heated up in the condenser to temperatures around 40 °C. This is a typical supply temperature for houses with large surface heating.

The water is being pumped by the water pump ⑧ through the condenser ④ (see Figure 25). If the 3-way-valve ⑨ is completely closed, the water bypasses the RPW-HEX. As soon as the 3-way-valve is being opened, part of the water mass flow is being directed through the RPW-HEX ② discharging it. V-10 is a manual valve, which is used to throttle the bypass to achieve the same pressure loss in the bypass as in the RPW-HEX. After the mixing point, TI-36 is used to regulate the 3-way-valve during discharging.

The expansion valve and the evaporator are located inside a climatic chamber where the temperature and the air humidity can be set arbitrarily to test the HP under different climatic conditions.

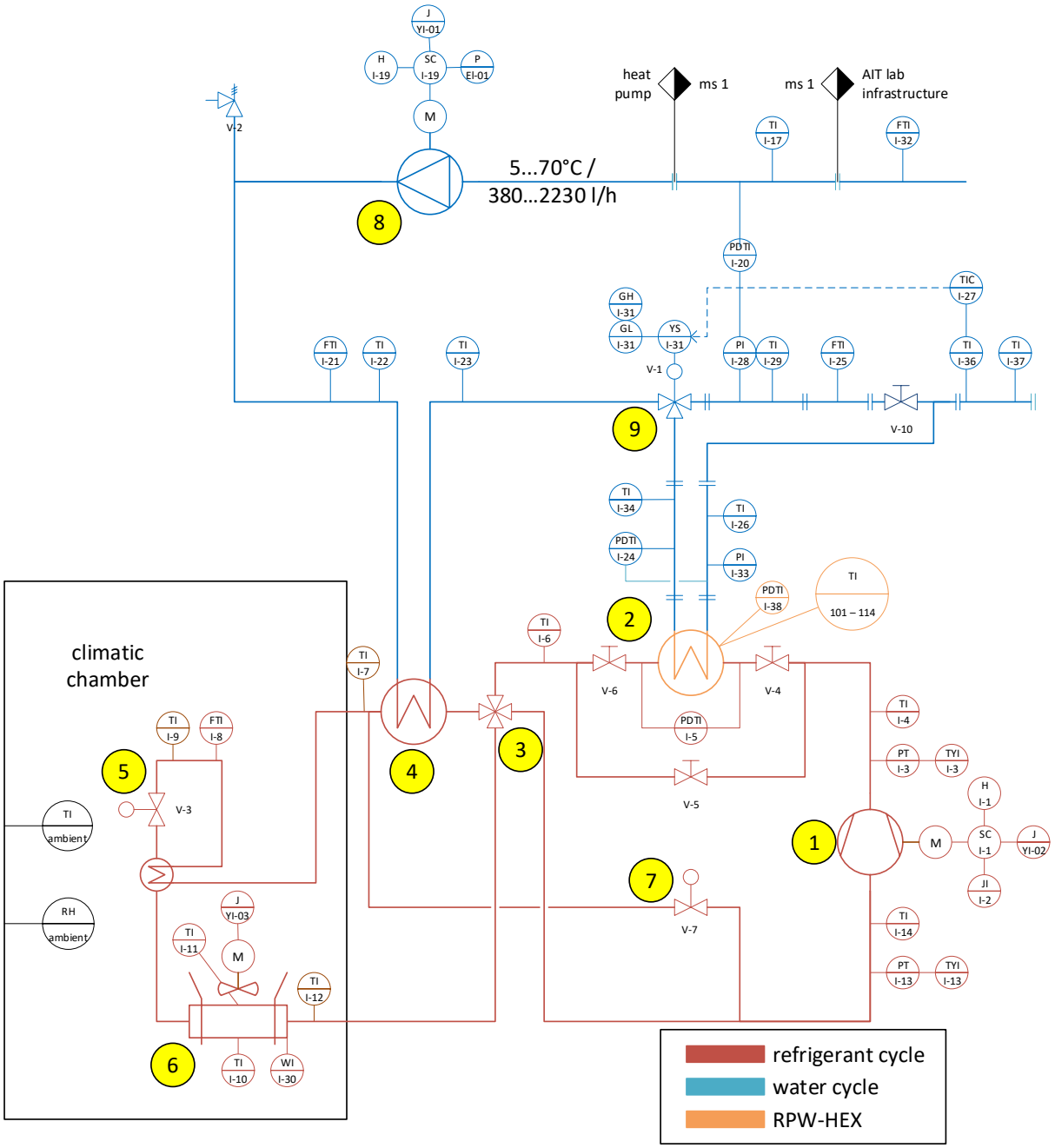

Figure 25: P&ID of the complete experimental setup. ① compressor, ② thermal storage (RPW-HEX), ③ 4-way-valve, ④ condenser, ⑤ expansion valve, ⑥ evaporator, ⑦ liquid injection valve, ⑧ water pump, ⑨ 3-way-valve. (TI) Temperature sensors, (PT) Pressure sensors, (FTI) mass flow sensors, (SCI) speed monitoring, (JI) electrical power measurement, (WI) scale.

All the sensors which are visualized in Figure 25 are either sensors which are originally installed in the HP or retroactively attached sensors by the AIT. Temperature sensors that have been installed in the original product are PT 1000 class B (TI-22, TI-23, TI-4, T-06, TI-12, TI-9, TI-7, TI-6, PTI-13, PTI-3, TI-36). Sensors provided by AIT are PT 100 class A (TI-17, TI-34, TI-26, TI-29, TI-37, TI-101 – TI-114). To achieve more accurate results, the PT 100 sensors are used whenever possible to validate the measured data. Mass flow measurements (FTI), scale measurements (WI) and electrical power measurements (JI) are also provided by AIT.

In case the HP is used in cooling mode or is performing a defrost, the 4-way valve switches and reverses the cycle (see Figure 26). The superheated refrigerant exiting the compressor ① still passes through the RPW-HEX ② but now the 4-way-valve ③ directs the hot refrigerant into the outside located evaporator ⑥. Thus, the evaporator becomes the condenser. The refrigerant passes the expansion valve ⑤ and is being evaporated in the condenser ④ which functions as evaporator in reversed mode. Subsequently, the refrigerant flows back to the compressor. In cooling and defrost operation the liquid injection valve ⑦ is not opened.

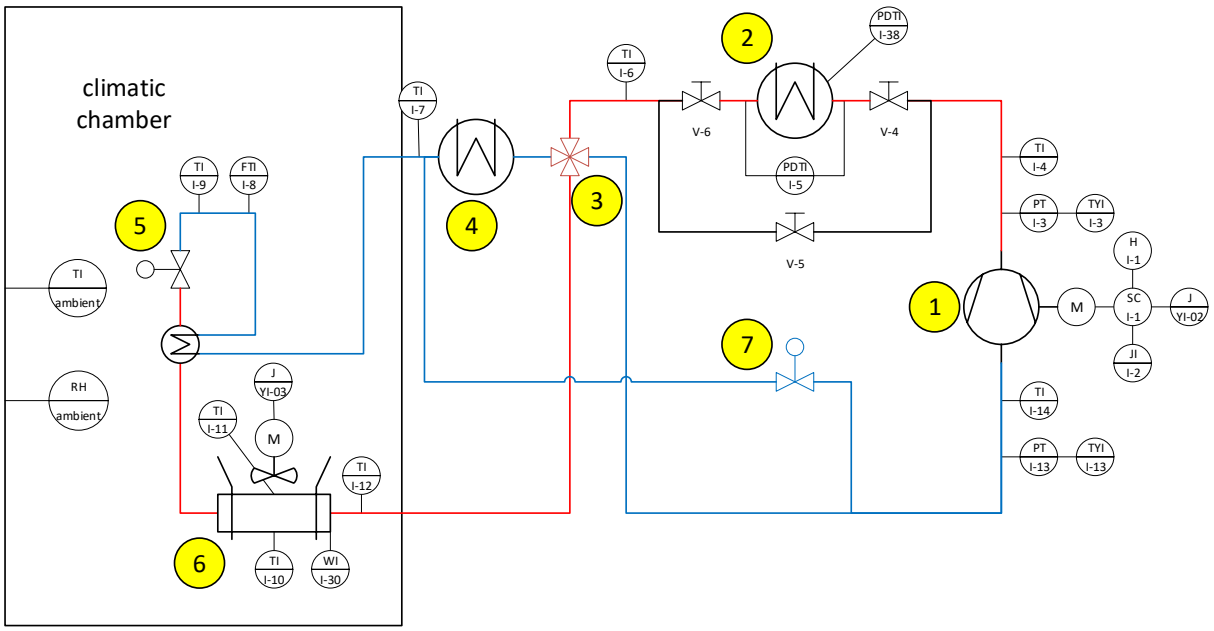

Figure 26: P&ID of the refrigerant cycle in cooling/defrosting mode. ① compressor, ② thermal storage (RPW-HEX), ③ 4-way-valve, ④ condenser, ⑤ expansion valve, ⑥ evaporator, ⑦ liquid injection valve.

3.2.6 Calculation of the relevant parameters

As visible in Figure 25 the systems useful heat $\dot{Q}$ exerts from two sources, the condenser, and the RPW-HEX. While the RPW-HEX delivers always heat, the condenser can also be used for cooling, depending on the operation mode. In that case, the useful heat of the condenser turns negative as the heat is being dissipated. In theory $\dot{Q}$ can be derived either from the refrigerant or the waterside. However, whenever the bypass opens the measurement of the refrigerant mass flow is incorrect. In addition, the refrigerant's state of phase is sometimes unclear after the condenser. Therefore, the useful heat cannot always be derived from the refrigerant side and in the course of this work and will always be derived from the waterside.

With the data from the visualized measurement devices (see Figure 25), power, energy, and efficiency of the system were calculated as followed:

$$\dot{Q} = (T_{\text{exit}} - T_{\text{inlet}}) * \dot{m} * \bar{c}_p(T_{\text{exit}}, T_{\text{inlet}}) \quad \textbf{(19)}$$

$\dot{Q}$ denotes the thermal power, T_{inlet} and T_{exit} are the respective inlet and outlet temperatures of a subsystem, $\dot{m}$ is the mass flow and $\bar{c}_p$ is the specific heat capacity given as a mean value. The thermal energy is calculated by integrating the thermal power over time:

$$E_{\text{thermal}} = \int \dot{Q} * dt \quad \textbf{(20)}$$

The electrical power of the system is the measured electrical power of the compressor and the fan of the evaporator. The power of the water pump is not considered. In order to regulate the total water mass flow for the experiments, the water pump runs at 90% of its capacity during the charging of the RPW-HEX and at 5% of its capacity during discharging. Since both of these operating points of the water pump are unrealistic, taking its electrical power into account would greatly falsify the results. The electrical energy of the system is again derived by integration over time:

$$E_{\text{el}} = \int (P_{\text{compressor}} + P_{\text{fan}}) * dt = \int P_{\text{el}} * dt \quad \textbf{(21)}$$

The COP is the proportion of the total thermal power $\dot{Q}_{tot}$ to the electrical power P_{el}.

$$COP = \frac{\dot{Q}_{\text{cond}} + \dot{Q}_{\text{RPW}_\text{W}}}{P_{\text{el}}} = \frac{\dot{Q}_{\text{tot}}}{P_{\text{el}}} \quad \textbf{(22)}$$

Here $\dot{Q}_{\text{cond}}$ is the thermal power provided by the condenser and $\dot{Q}_{\text{RPW}_\text{W}}$ is the thermal power provided by the RPW-HEX measured on the waterside.

Since the COP is only meaningful at a certain point in time or for a static system, the performance factor (PF) is introduced to describe the dynamic system. The PF is calculated from the thermal energy divided by the electrical energy:

$$PF = \frac{\int \dot{Q}_{\text{cond}}\, dt + \int \dot{Q}_{\text{RPW}_\text{W}}\, dt}{\int P_{\text{el}}\, dt} = \frac{\int \dot{Q}_{\text{tot}}\, dt}{\int P_{\text{el}}\, dt} = \frac{E_{\text{tot}}}{E_{\text{el}}} \quad \textbf{(23)}$$

The exact sensors that are used for the calculations can be obtained from Appendix A.

3.2.7 Data acquisition

The temperature and air humidity of the climatic chamber is controlled with a *DAC vista* system and recorded with a *LabView* program and *Agilent* at AIT. Using an interface converter (eWON - Flexy 205 from HMS Industrial Networks) converting from ModBus RTU to OPC-UA (see Figure 27) allowed the *OCHSNER* HP to communicate with the AIT lab infrastructure.

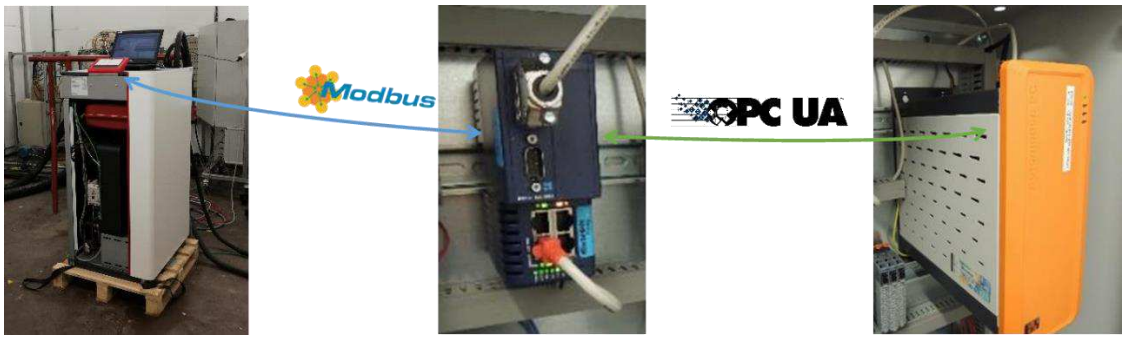

Figure 27: Communication between Ochsner HP controller (left) and Bernecker und Rainer APROL® industrial PC. ("HYBUILD deliverable 3.2," 2020)

Sensors provided by AIT are connected to the existing automation system, an industrial PCS system from *Bernecker und Rainer* (*B&R*) using the APROL® software and X20 PLC hardware (see Figure 28).

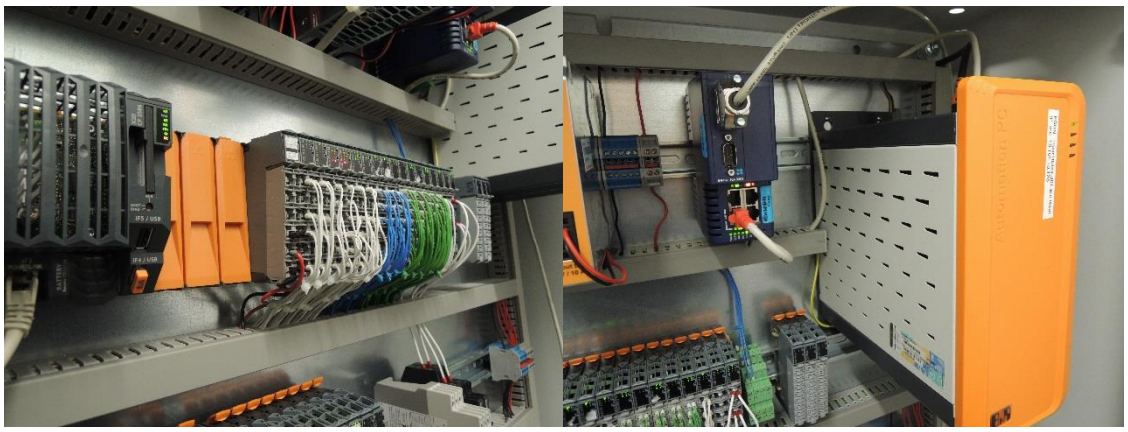

Figure 28: Bernecker und Rainer industrial hardware used in AIT thermal laboratory. ("HYBUILD deliverable 3.2," 2020)

From the *B&R* server, the data is easily accessible with tools of *B&R Industrial Automation GmbH* like APROL DISPLAY CENTER (see Figure 29). From the same display center, the HP is also being controlled. For the stand-alone *mini-LHS* the temperature sensors, as well as the heat flux sensor, were directly connected to the *X20* system from *B&R*.

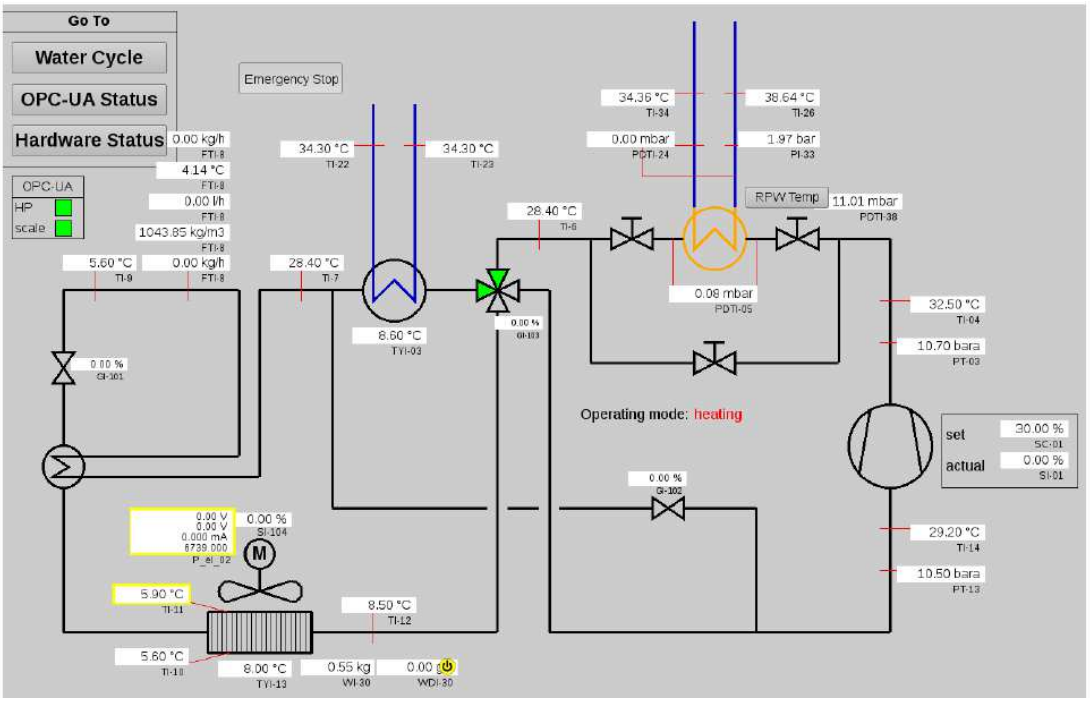

Figure 29: Screenshot of the APROL DISPLAY CENTER showing all the sensors and their current values in the refrigerant cycle.

From the *B&R* server, the data was transferred to a local computer where calculations were carried out in *PYTHON*. Plots to visualize the results were also made with *PYTHON.*

4 Results and discussion

In this chapter, the experimental results for both experimental setups are being discussed. With the use of these results, possible improvements for the HP system are being deduced.

4.1 Stand-alone mini-LHS

In the first test setup, it quickly became clear that the heat conduction through the aluminum had a strong influence on the results of the test. A mean temperature between the hot and the cold water temperature accommodated on every wall of the *mini-LHS*. When the two fins were heated to 70 °C and 50 °C, every wall reached a temperature of 60 °C. Thus, the PCM did not solidify as desired on the cold fin and form a phase front but solidified on all walls, in case the mean temperature was below the solidification temperature. The PCM was primarily formed at the bottom of the box. Figure 30 represents this effect.

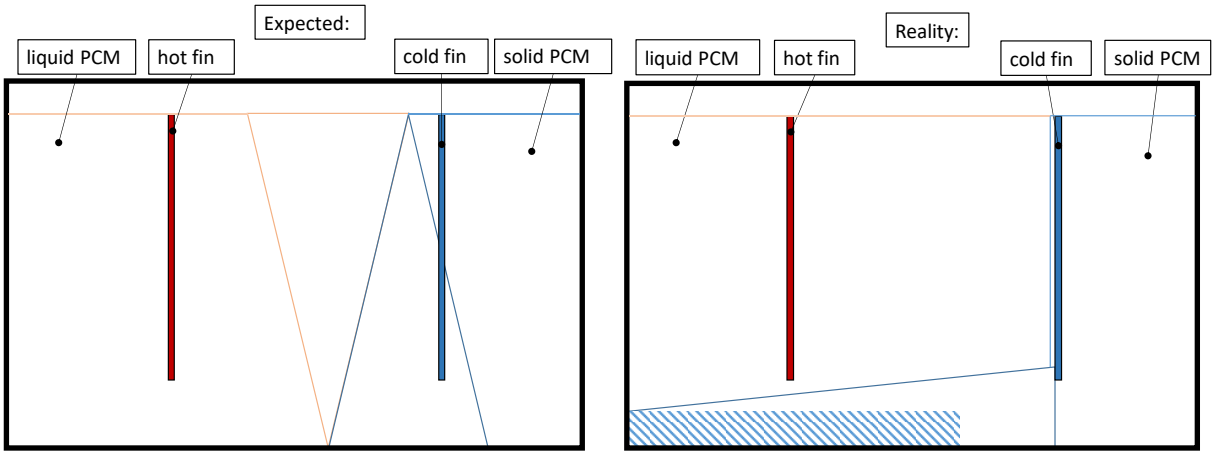

Figure 30 Schematic illustration of a cross-section of the LHS with the expected and the real accumulation of the phase front.

Another problem that resulted from this phenomenon was arching in the phase front in front of the cold fin. The solid PCM cumulated on the sidewalls and as it contracted it pulled the already solid PCM away from the cold fin, creating an air gap between the cooling fin and the PCM (see left in Figure 31). To solve this problem, the inside walls of the storage were insulated with *Armaflex* (2mm) (see center and right in Figure 31).

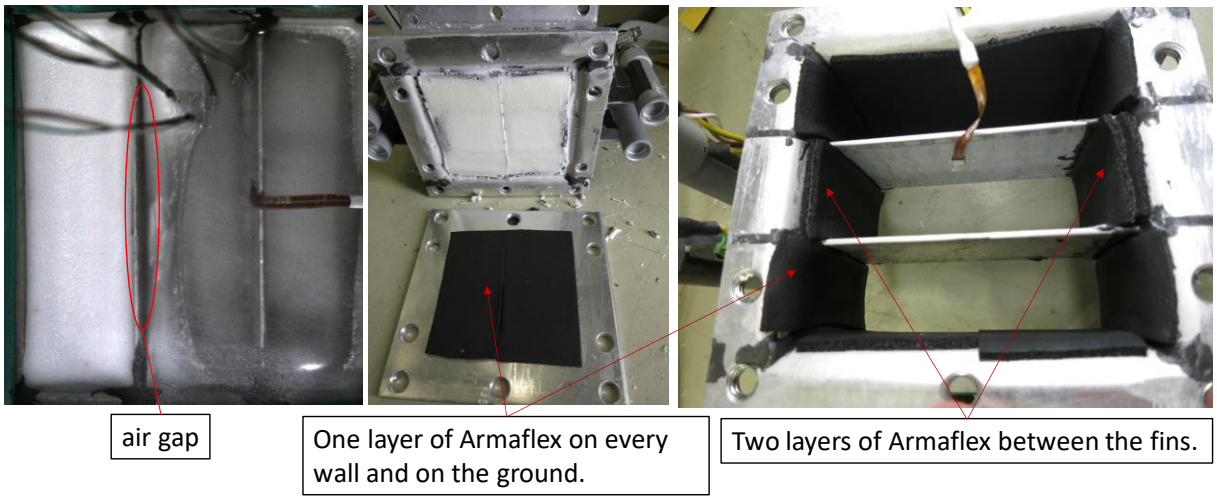

Figure 31: Left: The left fin has a constant temperature of 50°C while the right fin has 70°C. The solid PCM decreased its volume while cooled down further resulting in an air gap between PCM and the fin. The PCM solidifies primarily on the ground and on the side walls. Middle & Right: Inside insulation of the *mini-LHS* with Armaflex.

The result was a steadily growing layer of solid PCM on the cold fin as it was initially desired (see Figure 32).

Without inside insulation:

ΔT: 20°C (50°C-70°C)
Solid PCM accumulates on the bottom and on the side walls.

With inside insulation:

ΔT : 30°C (40°C-70°C)
Solid PCM accumulates only on the cold fin.

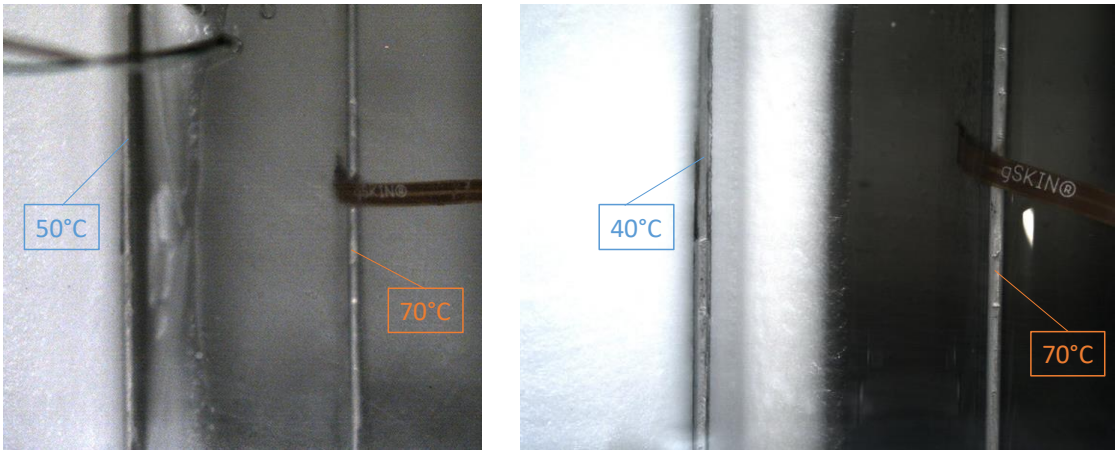

Figure 32: Comparison of the phase front without (left) and with (right) inside insulation.

Another challenge with the *mini-LHS* was to seal them against the liquid PCM. Even if the storage tank was watertight, it was still possible that PCM drained because the liquid PCM has a lower viscosity than water. At first, the storage was sealed as intended by *AKG*. The bottom flange was sealed with a flat gasket and 10 screws. As visible in the picture in Figure 33, this was insufficient. Liquid PCM trickled through the boreholes and between the sealing surfaces.

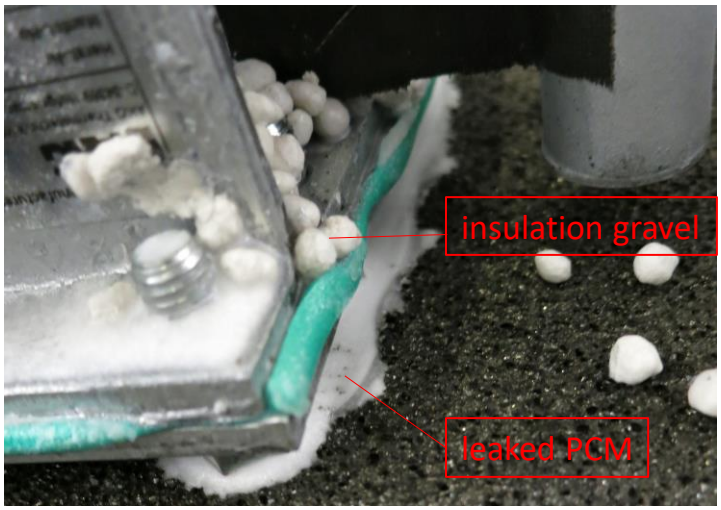

Figure 33: Picture of leaked PCM after the LHS was sealed with a flat gasket.

As a second approach to diminish this problem, the LHS was sealed with a high-temperature silicone without the flat gasket. In Figure 34 this procedure is being visualized. However, this proved not to be sufficient as well.

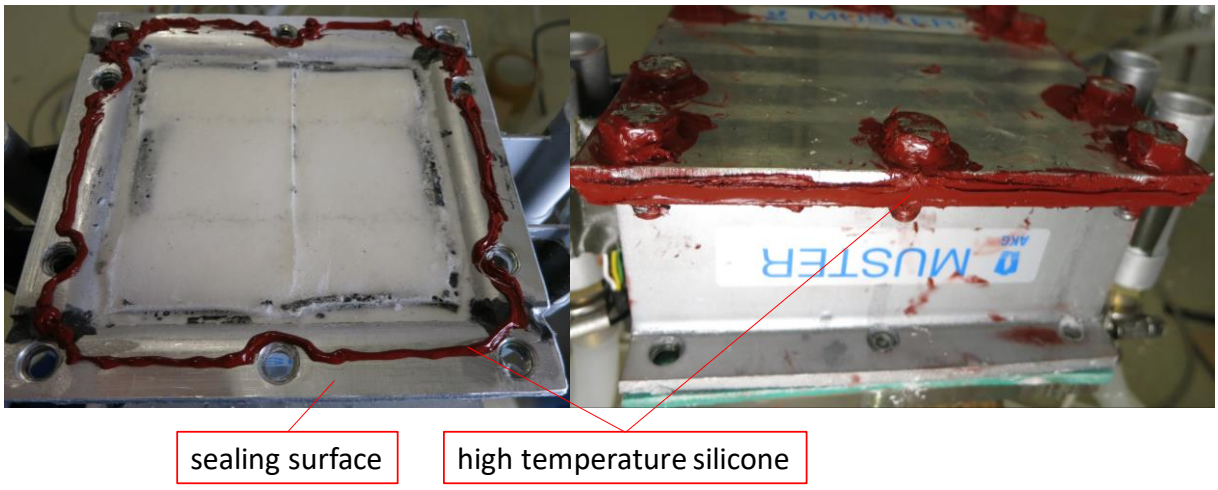

Figure 34: Photographs of the sealing surface and the bottom of the PCM box, being sealed with high-temperature resistant silicone.

This procedure was repeated 3 times also using silicone together with the flat gasket, without success. This leads on the one hand to the conclusion that the silicone is not suitable for sealing against this PCM and on the other hand to the conclusion that the flat gasket alone cannot efficiently seal against liquid RT64 even though the tank was impermeable to water.

In the next attempt to finally overcome the leakage problem Loctite 3475 (Epoxy) was used. As illustrated in Figure 35 the sealing surface, as well as the screws, were sealed with Loctite. This solution proved to be sufficient although the *mini-LHS* was now permanently sealed.

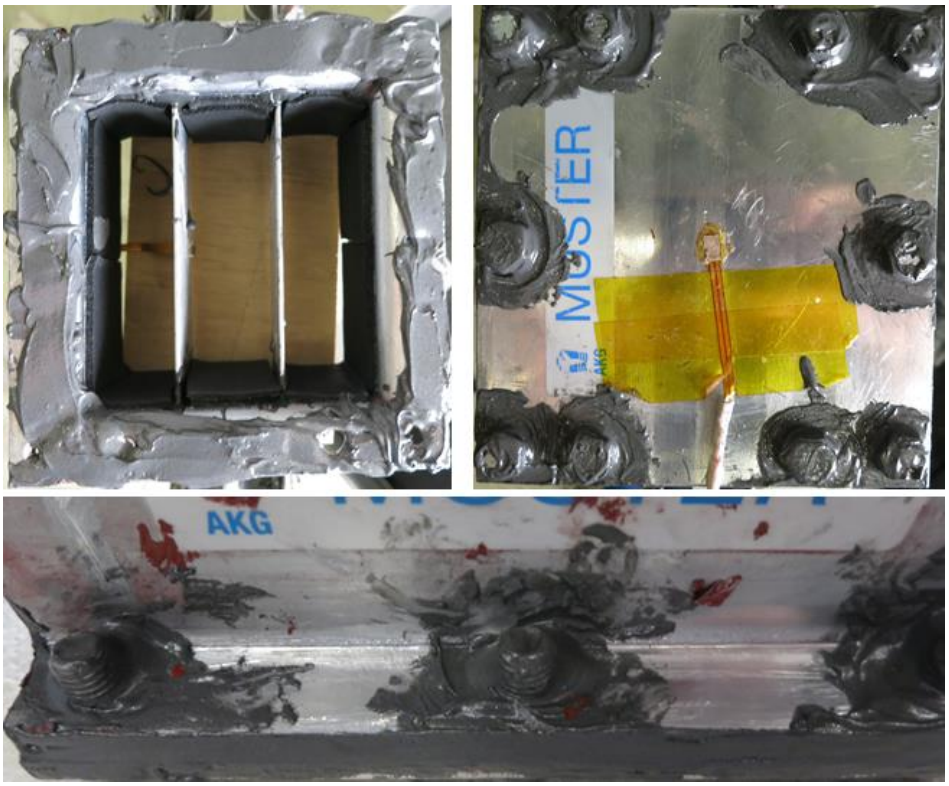

Figure 35: Sealing the Storage with Loctite 3475.

To get a better understanding of the PCM (RT64) a series of tests were performed. These tests are divided into two parts, the former are labeled *stationary tests* and the latter are labeled *dynamic tests*.

4.1.1 Stationary tests

In the first setup, the hot fin temperature was kept constant at 70 °C while the cold fin temperature was being adjusted step by step (see Figure 36). The temperature profiles of this test are visualized in Figure 36. The test is divided into two parts. In the first part, the PCM was completely melted at a temperature of 70 °C (see bottom left of Figure 36) and then the cold fin temperature was set to 58 °C. As soon as the phase front reached a steady-state the cold fin temperature was lowered by 2 °C. In the second part, this process was reversed. First, the PCM was cooled to 34 °C (see bottom right of Figure 36), then the hot fin temperature was set to 70 °C. As soon as the phase front reached a steady-state, the cold fin temperature was raised by 2 °C step by step.

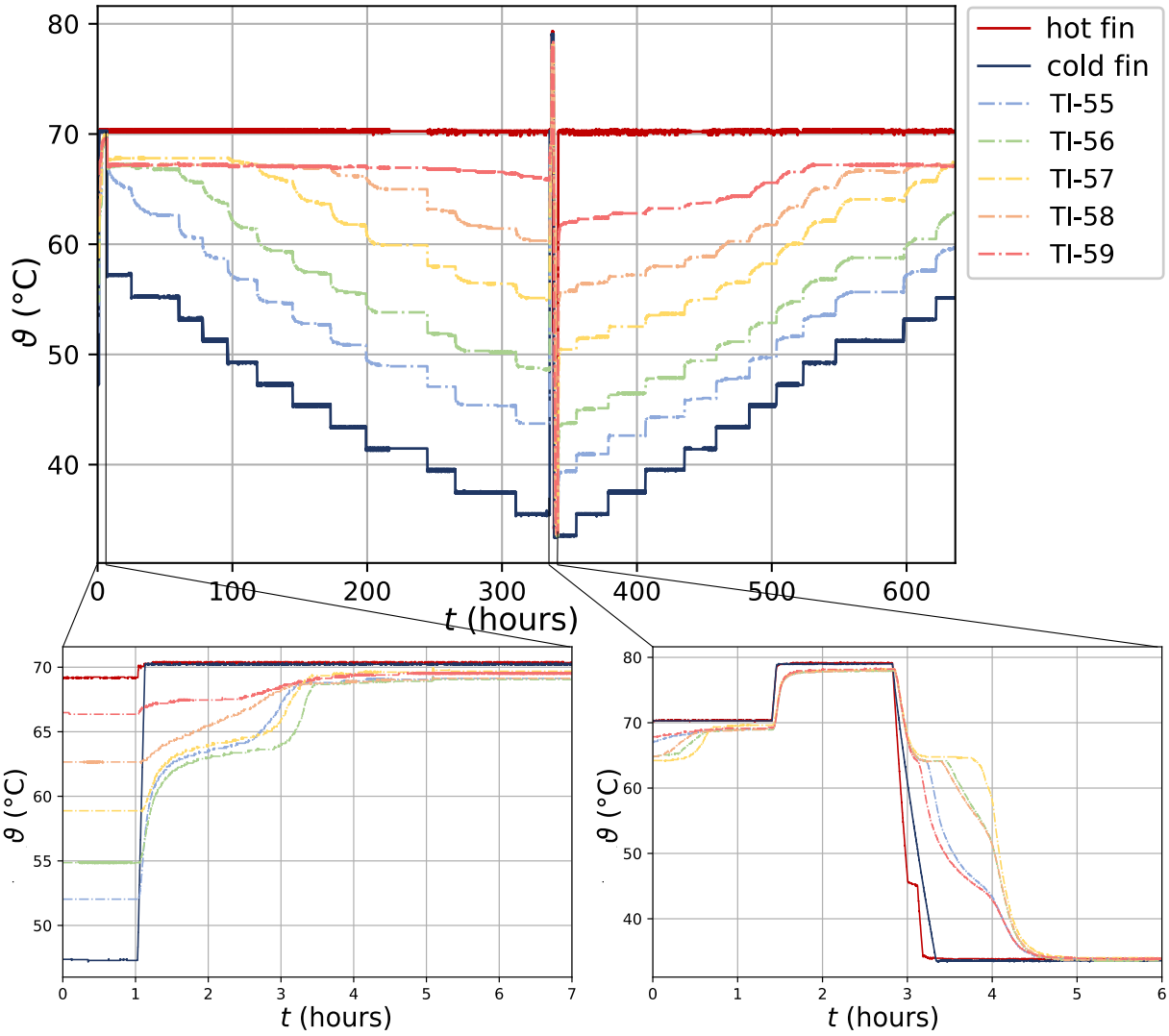

Figure 36: Temperature profile of the *stationary test* with the *empty-sample*. The hot fin is constantly kept at 70 °C while the cold fin is lowered and raised step by step. Top: Hot and cold fin temperatures as well as PCM temperatures TI-55 to TI-59. Bottom left: Initial temperatures before the stationary cooling test was started. Bottom right: Initial temperatures before the stationary heating test was started. Note that the initial temperatures and states of the phase of the PCM have a large impact on the development of the experiment.

The results of these two experiments are visualized in Figure 37.

Because the changes in temperature were very small and the volume of the PCM was large compared to the area of the fins, neither melting nor solidification peaks can be observed in the temperature profile of the PCM (TI-55 to TI-59).

With every temperature reduction, the heat flux jumped to a higher value which had its origins in the greater temperature difference. At the same time, the phase front started to grow. Interestingly the heat flux kept decreasing even after the phase front reached a steady state. Despite that, it is still visible that as the phase front emerged the heat flux decreased at a higher rate. This supports the assumption that the heat flux through the solid PCM was the limiting factor of the total heat flux.

The thermal conductivity λ rose with growing heat flux and with a growing phase front (equation (16)). This correlation is visible as λ reached a minimum when the cold fin temperature was lowered and rose together with the growing phase front. RUBITHERM states that λ is 0.2 $Wm^{-1}K^{-1}$ but does not provide its temperature dependency. However, λ was different in between the two tests which indicates that either equation (16) was not suitable or that the difference in measured heat flux caused this difference.

After each temperature jump, the heat flux slowly decreased. Between hours 200 and 250 in the cooling test the data recording system crashed. But it is visible from the behavior of the phase front that the temperature was lowered within this timeframe. Between hours 100 and 150, the system which took the pictures of the phase front crashed, which is the reason for the lack of data in this time period. The same happened between hours 150 and 200 in the heating test.

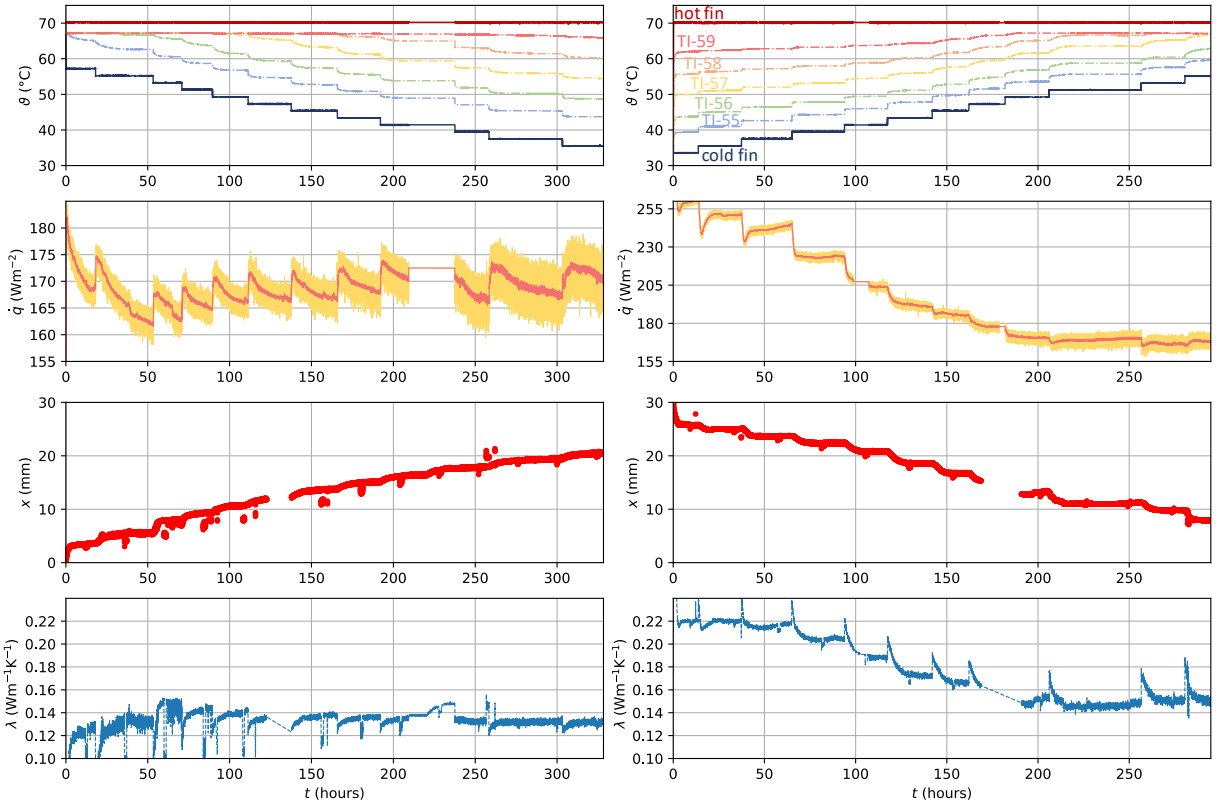

Figure 37: Experimental results of the stationary experiments with the *empty-sample*. Left: Results from cooling the liquid PCM by reducing the temperature of the cold fin step by step. Right: Results from heating the solid PCM by increasing the temperature of the cold fin step by step. Top: Temperatures of the cold and hot fin together with the temperatures inside the PCM. Second: The heat flux measured between the hot fin and the PCM and its mean value (running mean over 200 values). Third: Measured phased front thickness x. Bottom: Calculated lambda via the heat flux and the phase front thickness with equation (equation (16)).

To validate if the measured heat flux is in accordance with the heat flux calculated with equation (15), both curves are presented in Figure 38. In the cooling test, the calculated heat flux through the solid PCM was significantly higher. In the heating test, the calculated heat flux was almost constant, even though the temperature of the cold fin was raised, thus decreasing the temperature difference between the phase front and the cold fin. This is because the thickness of the solid phase x was declining at the same rate. The measured heat flux decreased below 200 Wm^{-2} as the temperature of the liquid PCM surrounding the hot fin reached temperatures close to the fin temperature. Changes in the cold fin temperature did always have an immediate effect on both, the calculated and the measured heat flux. Although, in the latter part of the experiments this influence onto the measured heat flux was diminishing. From Figure 38 it can be derived that the assumption of equation (6) is wrong. Thus, $\dot{q}_1 \neq \dot{q}_2$. The calculated heat flux which describes $\dot{q}_1$ was not equal to the measured heat flux $\dot{q}_2$. If the heat flux would be calculated for $\dot{q}_2$ the two graphs in Figure 38 would likely show the same values. But because the thermodynamic properties of RT64 were not known, only $\dot{q}_1$ could be derived numerically. To see if the calculation of $\dot{q}_1$ is reliable the experiment was changed where the heat flux sensor measured $\dot{q}_1$ (see chapter " 4.1.2 *Dynamic tests")*.

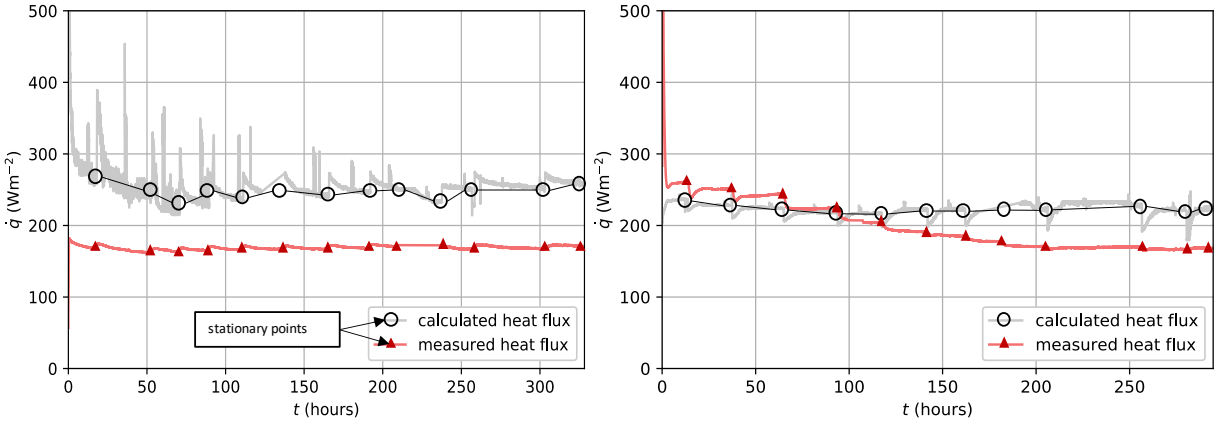

Figure 38 Representation of the measured and the calculated heat flux of the stationary experiments with the *empty-sample*. Left: The liquid PCM was being cooled. Right: The solid PCM was heated up.

Since the hot fin temperature is steady at 70 °C, the measured data can be described as a function of the cold fin temperature. It is clear that between the melting and solidification process there are major differences. Even though the temperature difference between the hot and cold fin is the same, a different steady-state is reached. This observation can be enhanced by looking only at the data points just before the cold fin temperature was lowered or raised respectively.

Figure 39 visualizes these data points as a function of the cold fin temperature. The temperatures inside the PCM strongly differed from each other depending on if the steady-state was reached by cooling the PCM or by heating it. Naturally, with different temperatures inside the PCM, the phase front did not reach the same position and the heat flux which was measured by the difference between liquid PCM and hot fin also differed, especially in the first half of the heating process. When being heated, the solid phase was around 2 mm thicker.

This behavior can be explained by the fact that the state of the PCM is not only dependent on the temperature but is also affected by its previous state (Jin et al., 2015). The heating and cooling tests had different initial conditions. The initial condition for the cooling test was the PCM being in solid state whereas in the heating test the PCM was completely melted. In the heating process, the heat flux was a lot higher because the temperature difference between the hot fin and the PCM was higher.

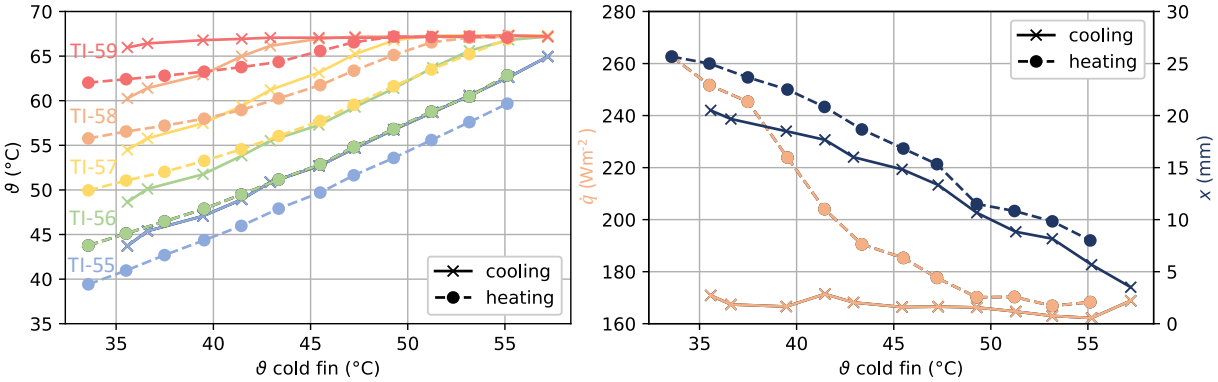

Figure 39: Measured data points before the cold fin temperature was raised/lowered in dependence of the cold fin temperature. Left: Temperatures TI-55 to TI-59. Right: Heat flux and thickness of the solid phase front.

When comparing the temperatures inside the PCM and the heat flux in dependence of the phase, front it is visible in Figure 40 that the temperatures in the heating test were in general lower when reaching the same phase front length. With the solid phase front thickness x exceeding 18 mm the temperatures of heating and cooling test seem to converge.

The high difference in heat flux above 15 mm phase front thickness was due to the high temperature difference between the hot fin and the PCM. When being cooled the PCM temperature in front of the hot fin (TI-59) stayed around 68 °C. When being heated up this location was still covered in solid PCM which is indicated with TI-59 still being around 64 °C. The measured heat flux was in any case higher. The overall heat flux $\dot{q}$ cannot differ too much between those two tests since the temperature difference between the fins was equal and is the main driving force for the heat flux.

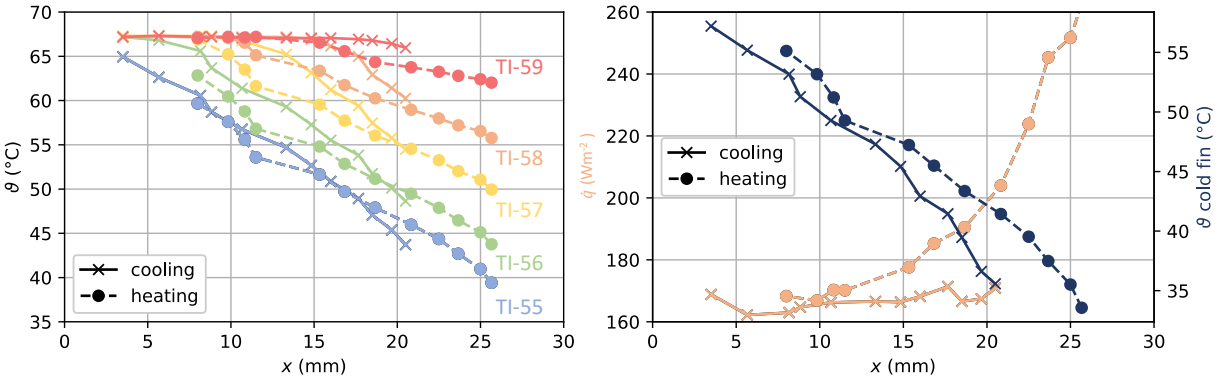

Figure 40: Measured data points before the cold fin temperature was raised/lowered in dependence of the solid phase front thickness *x*. Left: Temperatures TI-55 to TI-59. Right: Heat flux and temperature of the cold fin.

In the *fin-sample*, no heat flux was being measured because the majority of the transferred heat was conducted through the aluminum in between the two fins. A steady-state of the phase front was reached within an hour contrary to the *empty-sample* where it took up to 24 hours.

With the *fin-sample*, the same tests were carried out. The hot fin is kept constantly at 70 °C while the cold fin temperature is lowered and raised step by step. To prove that the state of the PCM is dependent on its previous state the heating test was conducted twice. They will be referred to as *heating case 1* and *heating case* 2. In *heating case 1* the temperature of the cold fin was raised right after the cooling test was conducted. In *heating case 2* the PCM was first lowered to a temperature

of 34 °C and then the hot fin was raised to 70 °C (like in the *empty-sample*). As soon as a steady-state was reached the cold fin temperature was raised step by step.

Figure 41 presents the measured data in these three tests. The phase front does not reach the same position. Marked with blue circles are phase front positions where the temperature difference between the two fins was the same (A, B, C). Between *cooling case* and *heating case 1* the difference in the phase front position was small and was attributed to the hysteresis effect between heating and cooling. In *heating case 2* the phase front reached again a different position. This indicates that the steady-state of RT64 is dependent on its previous state. In this case, there were three different previous states (1, 2, 3) resulting in three different phase front positions (A, B, C). One initial state was the PCM being completely liquid (1), one was two-phased (liquid and solid (2)) and the last one is completely solid (3).

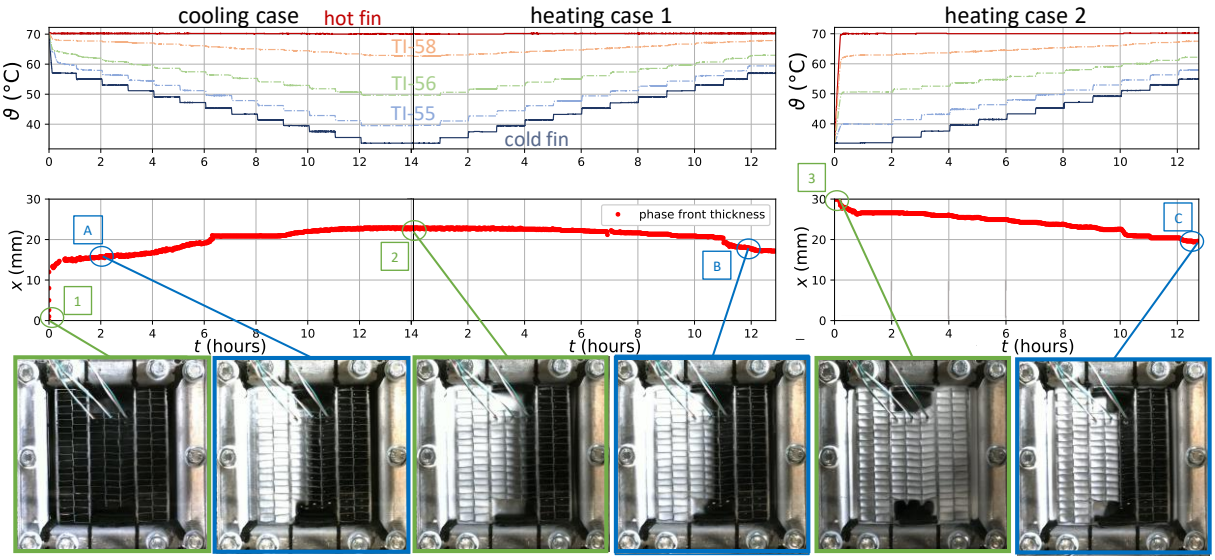

Figure 41: Experimental results of the stationary experiments with the *fin-sample*. Left: Results from cooling the liquid PCM by reducing the temperature of the cold fin step by step. Middle: Results from *heating case 1*. The solid PCM is melted by increasing the temperature of the cold fin step by step. Right: Results from *heating case 2*. The solid PCM is melted by increasing the temperature of the cold fin step by step. Top: Temperatures of the cold and hot Fin together with the temperatures inside the PCM (TI-55, TI-56, TI-58). Bottom: Measured solid phased front thickness. Underneath are pictures of the set up at certain times visualizing the solid phase front in various positions.

Contrary to the tests with the *empty-sample*, the temperatures inside the PCM for the *fin-sample* did not differ significantly from each other when comparing them as a function of the cold fin temperature (see the upper left in Figure 42). This is caused by the aluminum structure between the fins. The heat gets distributed a lot better inside the PCM. Even though the temperatures appear to be the same, the phase front is always in a different position (see the lower left in Figure 42). Hence, when comparing the temperatures as a function of the phase front thickness (see right in Figure 42), a difference is noticeable. Especially between the cooling and the two heating cases. This is an indication, that even with the same temperature inside the PCM at a specific position, a different state of phase can develop. For further understanding more detailed tests have to be performed, focusing on the solid structure and nucleation.

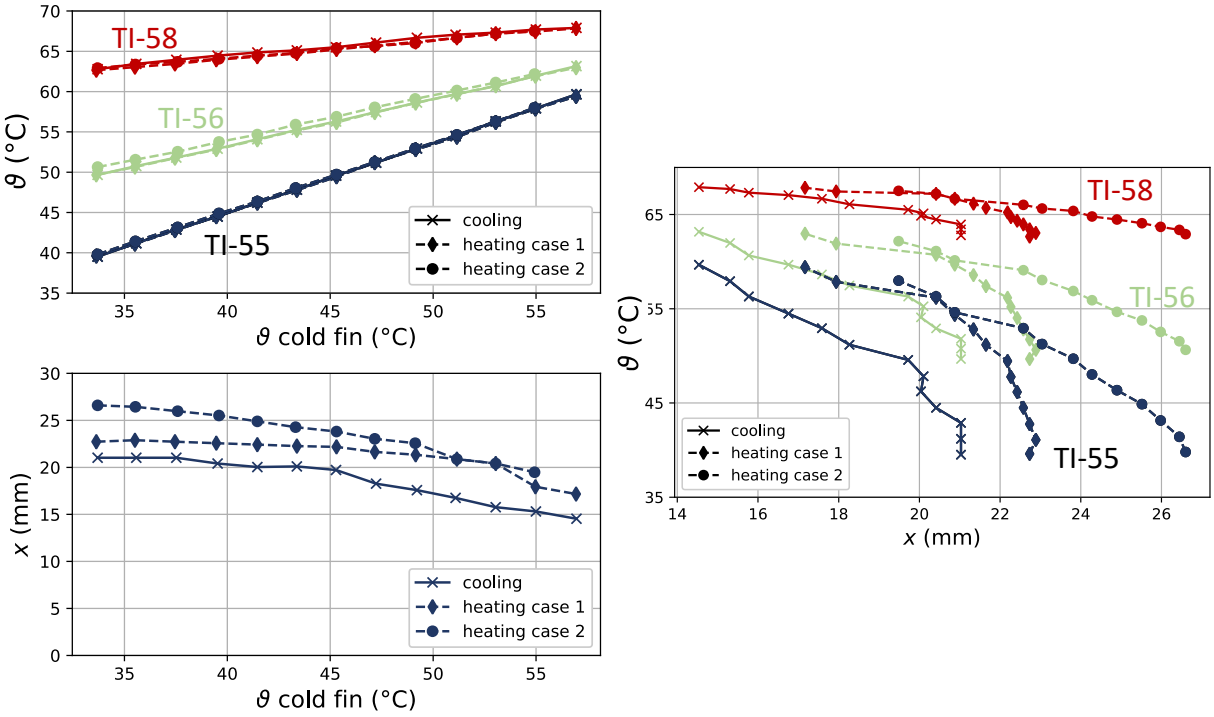

Figure 42: Measured data points before the cold fin temperature was raised/lowered. Left top: PCM temperatures TI-55, TI-56, and TI-58 in dependence of the cold fin temperature. Left bottom: Solid-phase front thickness in dependence of the cold fin temperature. Right: Temperatures TI-55, TI-56 and TI-58 in dependence of the solid phase front thickness.

4.1.2 Dynamic tests

To acquire a more dynamic response of the system, the PCM was brought to a certain temperature before a large temperature difference was set between hot and cold fin. The temperature difference was chosen so that the phase front could spread over almost the entire gap between the fins or melt completely. With the *empty-sample*, three tests were performed this way. One of the tests was done to see if the position of the heat flux sensor on the hot fin had a major influence on the measurement.

The left graph in Figure 43 represents the measured data as the PCM is being cooled down from 70 °C with one fin set to 25 °C and the hot fin staying at 70 °C. At 64 °C, the temperature curves have a strong dent which represents the solidification peak. The heat flux jumped to 150 Wm^{-2} as the cold fin reached 25 °C. From that moment on, it slowly declined as the phase front emerged at relatively high speed. But as soon as the phase front passed the 20 mm mark, hence 70% of the PCM was already solid, the heat flux started to rise again. Since the heat flux was measured through the temperature difference of PCM and hot fin, this behavior is a consequence of the PCM staying at the same temperature as long as enough solidification enthalpy is released. As soon as a major part of the PCM was solidified it cools down radically. After 6 hours the temperatures appeared to have reached a steady-state. At the same time, the measured heat flux started to rise dramatically. The phase front was still growing and as it got closer to the hot fin the liquid PCM around the cold fin was cooling down. With the phase front reaching a steady-state also the heat flux leveled out slowly. The thermal conductivity λ which was calculated through the measured heat flux and the phase front was steady in the first 3 hours. This is a strong indication that the decreasing heat flux in the beginning and the growing phase front are interdependent.

On the right side of Figure 43, the solid PCM at a temperature of 49 °C was being melted with one fin set to 72 °C. As the hot fin reached this temperature the heat flux peaked at approximately 1400 Wm^{-2} because the temperature difference between the solid PCM and the hot fin has a maximum. As soon as a gap of liquid PCM has emerged from the hot fin the heat flux decreased sharply. With the declining share of solid PCM, the calculated heat flux rose. With the measured heat flux being almost constant after two hours, λ was only a function of the phase front position and behaved accordingly.

The calculated heat flux had the tendency to behave like the measured heat flux from the opposite test. This shows that the heat flux was probably dependent on the location where it has been measured. When located on the fin where the temperature is changed, the heat flux peaked at the beginning of the test. Likewise, the heat flux started at a low value when placed on the stationary fin and rose throughout the experiment. It is obvious that the calculated heat flux is mirroring the phase front thickness x because the temperature of the phase front and the cold fin are constant throughout the experiment. Thus, the calculated heat flux is solely a function of x.

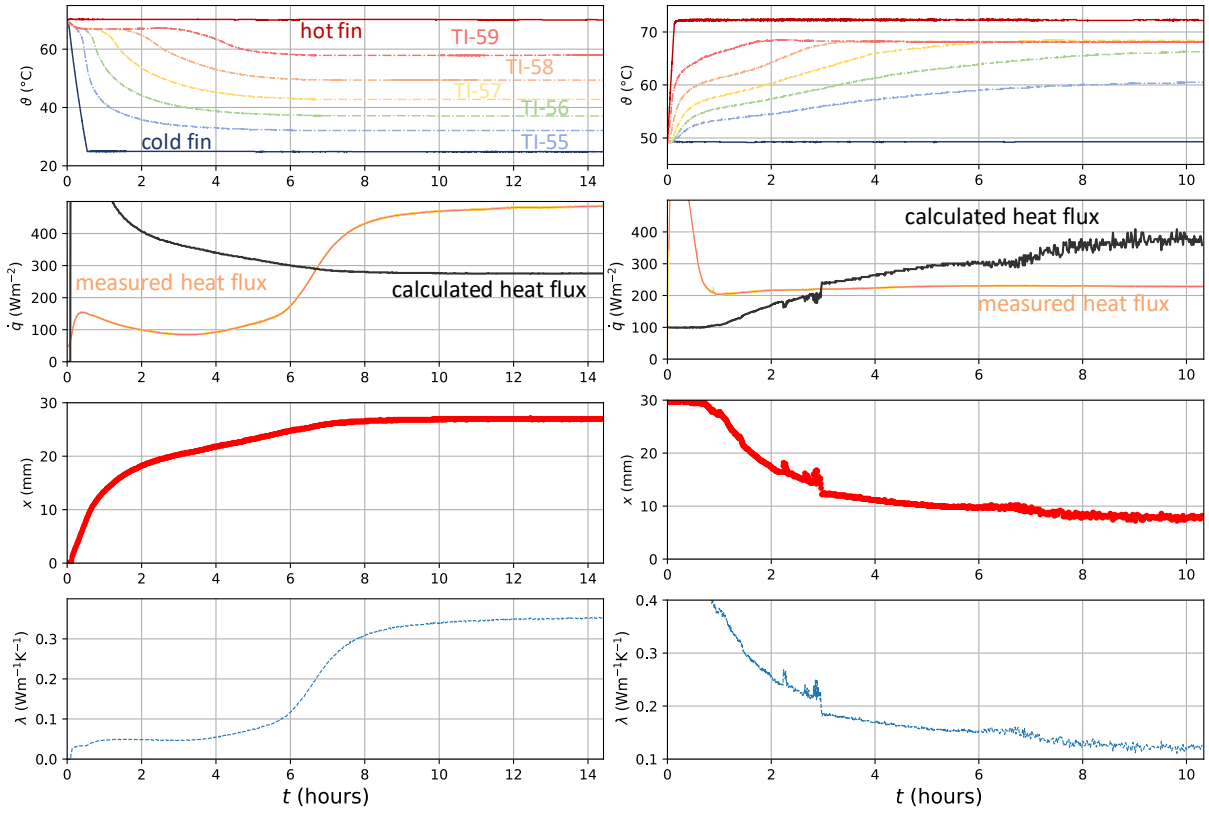

Figure 43: Measured data during *dynamic tests* with the *empty-sample* as a function of time. Top row: Temperature profile of the PCM (TI-55 to TI-59) as well as hot and cold fin temperatures. Second row: Heat flux and running mean value of the heat flux as well as the calculated heat flux. Third row: Solid-phase front thickness. Bottom row: Calculated thermal conductivity with $\lambda = \lambda(\dot{q}, x)$. Left: PCM is being cooled from initially 70 °C with the cold fin set to 25 °C. Right: PCM is being heated from initially 49 °C with the hot fin set to 72 °C.

To check if the heat flux sensor displayed credible values the heat flux from the hot fin into the liquid PCM was calculated with equations (8) to (13). The thermodynamic properties of RT64 for these temperatures were not known exactly, therefore the results of these calculations were rather an estimation. For the kinematic viscosity $\nu = 8 * 10^{-6}$ m^2s^{-1}, the specific heat capacity $c_p =$ 1 $kJkg^{-1}K^{-1}$, density $\rho = 800$ kgm^{-3} and the thermal conductivity $\lambda = 0.2$ $Wm^{-1}K^{-1}$ was used.

Table 2 shows the resulting calculated heat flux following equations (8) to (13), in dependence of the hot fin temperature and the PCM temperature in front of the hot fin. Since the temperature inside the liquid PCM is not uniform, the temperature directly in front of the hot fin is unknown, its value can only be assumed.

Nonetheless, the results show that the liquid PCM in the dynamic cooling test probably reached between 66 °C and 67 °C right in front of the fin. The heat flux peak in the dynamic heating test in the *empty-sample* is around 1400 W which matched the calculated results. With a PCM temperature of 64 °C, which is the melting temperature, the calculated heat flux on the liquid side amounts to approximately 1400 W.

Table 2 Results of the calculated heat flux (equation (8) to (13)).

measured hot fin temperature (°C)	assumed temperature of the PCM (°C)	calculated heat flux following equations (8) to (13) (W)
70	69	100.843
70	68	244.796
70	67	412.084
70	66	596.871
72	65	1228.059
72	64	1460.164
72	63	1701.391

To see if the calculated heat flux through the solid phase and the measured heat flux provide the same results, a third test was performed (Figure 44). This time the heat flux sensor was not located in the liquid PCM but on the cold fin where the PCM was solid throughout the whole test. The solid PCM (49 °C) was melted with the other fin set to 72 °C. In the first hour, liquid PCM was pressed out of the emerging liquid gap and reached the heat flux sensor (see Figure 44 on the right side). Hence it was not possible to evaluate if the heat flux displayed the same values as in the cooling test during the first two hours. But throughout the remaining experiment, the calculated and measured heat flux are behaving very similarly. The measured heat flux rose between 400 and 500 Wm^{-2}. Because of clogging in the hot fin, its temperature dropped constantly throughout the experiment which was probably the cause for the declining measured heat flux after 6 hours.

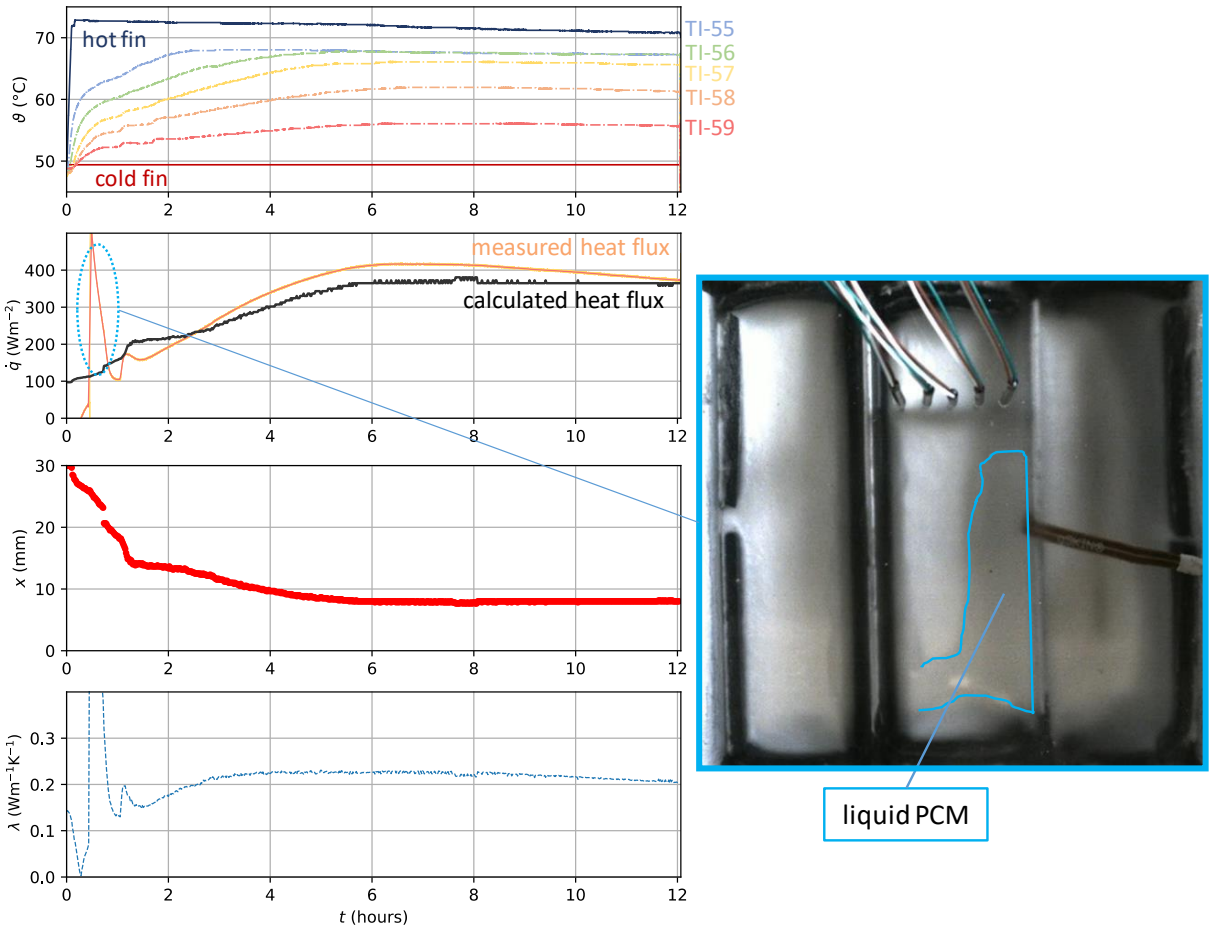

Figure 44: Measured data during the *dynamic test* with the *empty-sample* as a function of time. The PCM is heated from an initial temperature of 49 °C with one fin set to 72 °C. Contrary to all other experiments, the fin without the heat flux sensor is used as hot fin and the fin with the heat flux sensor is used as cold fin.
Top to bottom is:
- Temperature profile of PCM temperatures and fin temperatures.
- Heat flux as well as moving average of the heat flux.
- Solid-phase front thickness.
- Calculated lambda as a function of phase front thickness and heat flux $\lambda = \lambda(\dot{q}, x)$.

Right: Image of the *empty-sample* showing the liquid PCM that caused the heat flux sensor to peak at the beginning of the experiment.

The positioning of the heat flux sensor had a strong influence on the measured data. When placed onto the fin where the temperature is being changed, a high peak appeared in the measured data at the beginning of the experiment. After that, the heat flux did not change significantly compared to when it is placed on the fin with a constant temperature. Here the measured heat flux is small at the start but as soon as most of the PCM had changed phase, it rose sharply.

The *dynamic tests* were also carried out with the *fin-sample*. Because of the enhanced heat transfer rate in the *fin-sample*, these tests required only a tenth of the time. The slow cooling rate of the *JULABO* affected the tests. As visible in Figure 45 the PCM temperatures followed the declining curve of the cold fin. The solidification peak can be well observed at 64 °C, the second peak in solidification however is not visible. The phase front reached 23 mm and was therefore 3 mm smaller than in the *mini-LHS* without fins. This effect could be a result of supercooling which is pronounced with higher cooling rates (Mollova et al., 2013; Uzan et al., 2017).

In the heating test, the difference between the two *mini-LHS* was a lot more significant. In the *empty-sample*, the phase front melted below 10 mm whereas in the *fin-sample* the solid phase

stayed at 20 mm. The temperatures deliver the explanation for this. TI-55 reached temperatures around 60 °C in the *empty-sample* (see the right image in Figure 43) whereas in the *fin-sample* TI-55 only reached 53 °C (see the right image in Figure 45).

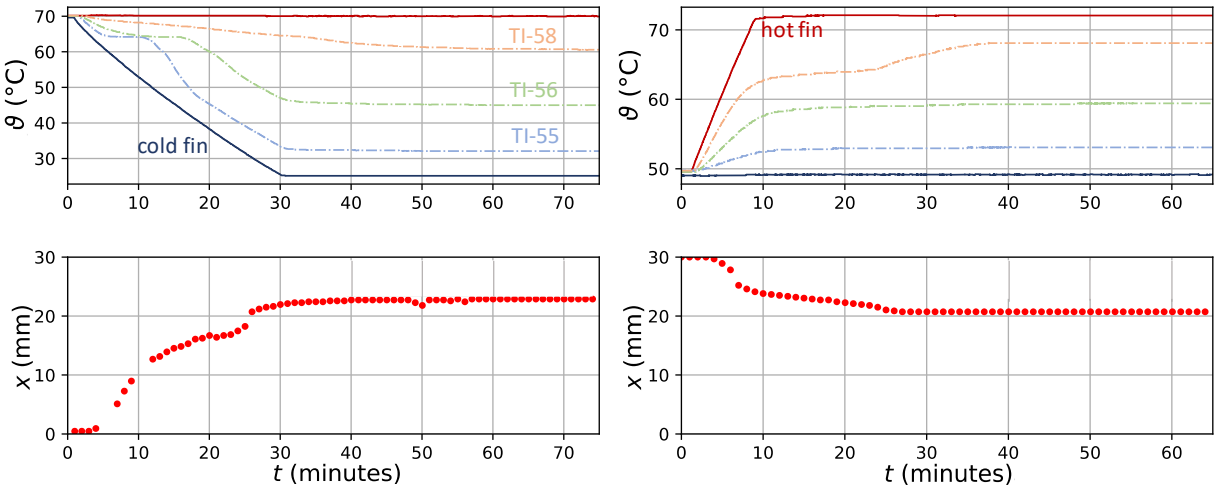

Figure 45: Temperature profile and solid-phase front thickness in the *dynamic tests* with the *fin-sample*. Left: Cooling the PCM with the hot fin at 70 °C and the cold fin set to 25 °C. Right: Heating the PCM with the hot fin set to 72 °C and the cold fin set to 49 °C.

A possible explanation for this discrepancy is the better heat distribution in the *fin-sample*. Looking only at the temperatures at the end of the dynamic heating tests in the *empty-sample* and the *fin-sample* it is clearly visible that in the *fin-sample*, contrary to the *empty-sample*, the temperature distribution was almost linear. The distribution inside the solid PCM was always linear but within the liquid phase, a linear temperature distribution is very unlikely due to convection.

Therefore, also the phase front reached completely different positions. Figure 46 illustrates the different temperature distribution at the end of each heating test with the *empty-sample* and the *fin-sample* together with the resulting phase front.

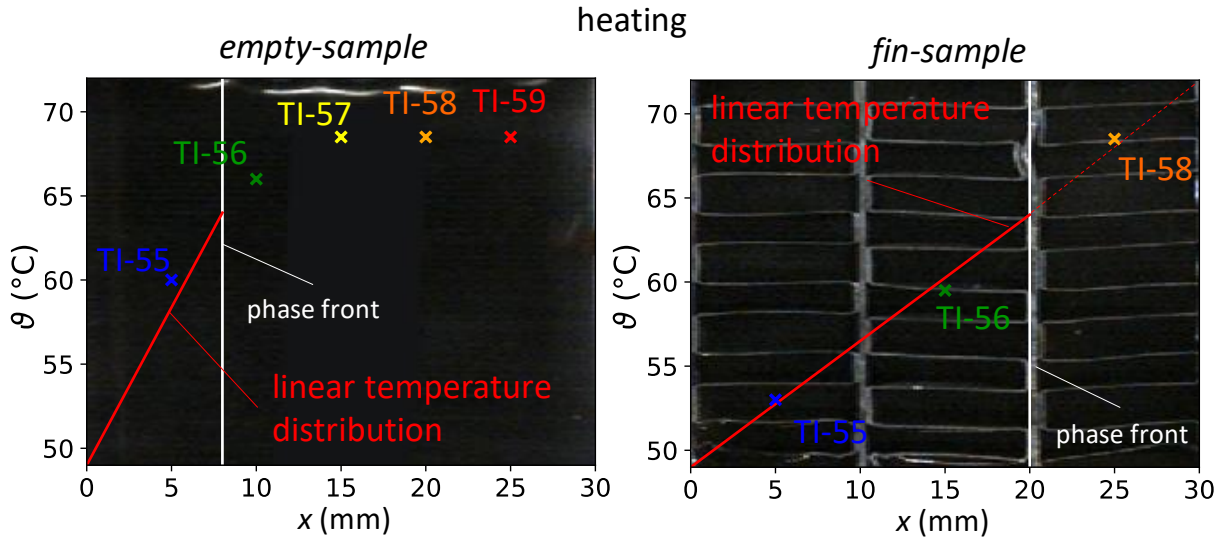

Figure 46: Measured PCM temperatures at the end of a test with the cold fin at 49 °C and the hot fin at 72 °C. Left: Temperatures TI-55 to TI-59 in the *empty-sample*. Right: Temperatures TI-55, TI-56, and TI-58 in the *fin-sample*. The red line represents a linear temperature distribution inside the solid PCM between the cold fin temperature and the temperature of the phase front. It is clearly visible that the temperature distribution in the *fin-sample* is also in the liquid phase almost linear.

In the cooling tests, the difference was not significant because inside the solid phase the temperature distribution was in any case linear. However, in Figure 47 it was visible that in the *fin-sample* the phase front did not reach the position of TI-58 even though the sensor displayed values cooler than 61 °C. This is a strong indication for subcooling.

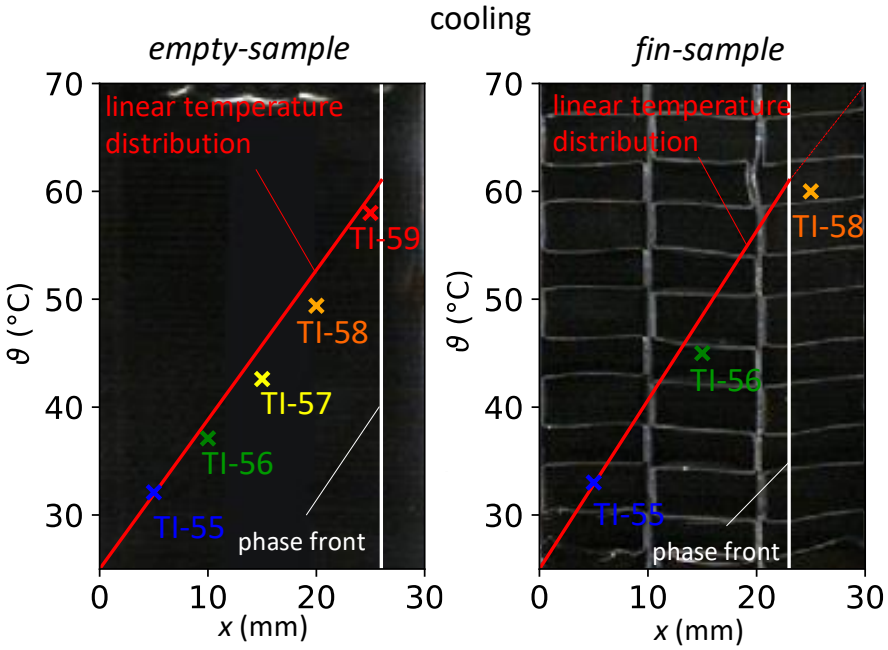

Figure 47: Measured PCM temperatures at the end of a *dynamic test* with the cold fin at 49 °C and the hot fin at 72 °C. Left: Temperatures TI-55 to TI-59 in the *empty-sample*. Right: Temperatures TI-55, TI-56, and TI-58 in the *fin-sample*. Note that TI-58 is lower than the solidification temperature which indicates subcooling. The red line represents a linear temperature distribution inside the solid PCM between the cold fin temperature and the temperature of the phase front.

Since in none of the experiments the second solidification peak was visible two additional tests were conducted where both fins were being cooled and heated simultaneously in the *fin-sample*. Interestingly both solidification peaks were clearly accentuated when both fins were being cooled at the same time (see Figure 48 left). Also, the melting peak is clearly visible at 64 °C (see Figure 48 right).

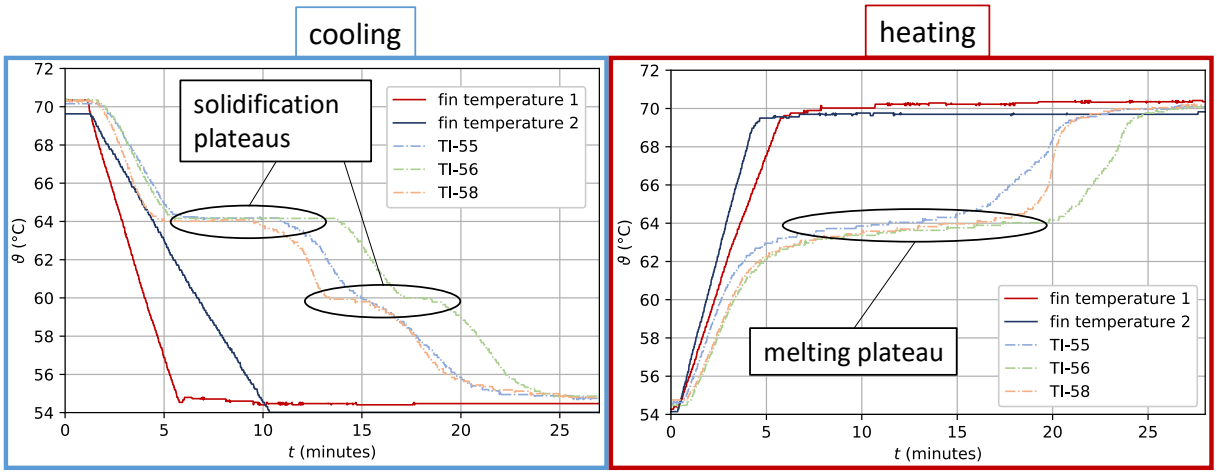

Figure 48: Temperature profile of PCM temperatures and fin temperatures in the *fin-sample* where both fins are being heated or cooled. Left: Cooling the PCM from 70 °C to 55 °C. Right: Heating the PCM up from 55 °C to 70 °C.

4.2 Integrated RPW-HEX experiments

In order to capture the behavior of the RPW-HEX and its influence on the compression HP, a series of tests were performed. The main parameters to describe each test series were:

- Outside temperature (T_{amb})
- Relative air humidity (RH_{amb})
- Water supply temperature (T-17)
- Water return temperature (T-37)
- Electrical supply AC/DC

Those default parameters are listed in Table 3.

Table 3: Default parameters for the different tests that were performed.

test	T_{amb} (°C)	RH_{amb} (%)	TI-17 (°C)	TI-34 (°C)	AC/DC	$u_{\mathrm{compressor}}$ (%)	$\dot{m}_W$(kgs^{-1})	discharge approach
Start-up	-	-	-	-	-	0-90	0.245	-
Charging	-7	75	33	43	AC	90	0.245	-
discharge case 1	-7	75	33	-	AC	0	0.14	I
discharge case 2	-7	75	33	-	AC	45	0.114	I
discharge case 3	-7	75	33	-	AC	57	0.14	I
discharge case 4	-7	75	33	-	AC	90	0.14	I
A-7W43_I	-7	75	34	43	AC	90	0.245/0.14	I
A-7W43_II	-7	75	34	43	AC	90	0.245/0.14	II
A2W37_I	2	85	31	37	DC	60	0.245/0.14	I
A2W37_II	2	85	31	37	DC	60	0.245/0.14	II
SoC	-7	75	31	37	AC	90	0.14	I
DC-voltage	2	85	31	37	DC	60	0.245	-

A-7W43_I and *A-7W43_II* as well as *A2W37_I* and *A2W37_II* had the same default values. These tests differed in the way they were discharged. Two different discharge approaches were examined:

Discharge approach I:

The RPW-HEX was discharged with 100% of the total water mass flow. The 3-way-valve opened completely. This resulted in water exit temperatures between 80°C and 55°C. When the water exit temperature of the RPW-HEX undercut 55°C, the discharge was stopped.

Discharge approach II:

In this approach, the aim was to achieve a constant system exit temperature of 55°C. Therefore, the 3-way-valve was regulated, letting only a portion of the water mass flow ran through the RPW-HEX. As the RPW-HEX now was discharged with a lower water mass flow, the discharging time increased compared to the discharge approach I. The discharge was stopped as soon as the RPW-HEX water exit temperature undercut 55°C.

A comparison of the water temperatures for those two approaches is given in Figure 49. The discharge approaches differed in the system's water outlet temperature.

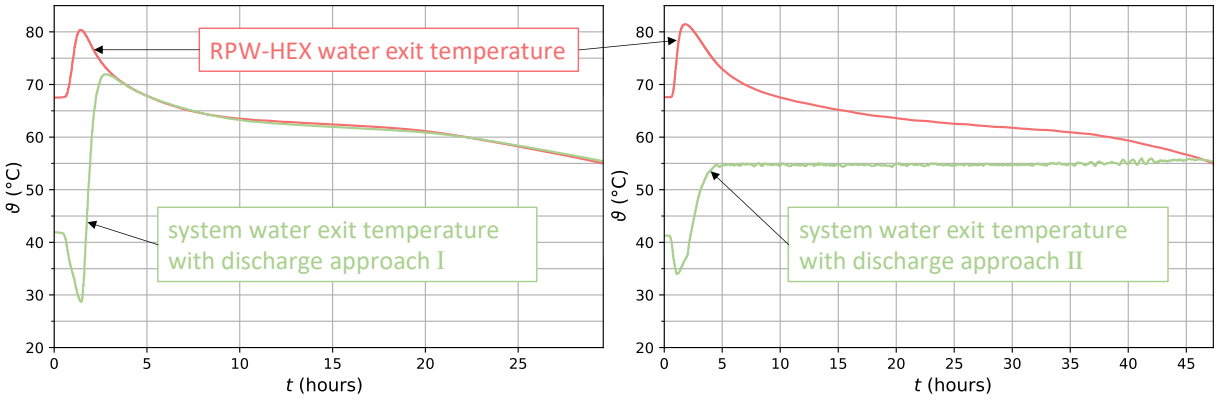

Figure 49: Measured water temperatures of two discharge cycles. The system outlet temperature is different, depending on which discharge approach was applied. Left: Discharge approach I. Right: Discharge approach II.

In the first experiments the RPW-HEX was leaking a small amount of liquid PCM (see Figure 50). The aluminum sealing, which was in place, proved not to be enough. In addition to the aluminum sealing, a Teflon thread sealing tape was used to solve the problem.

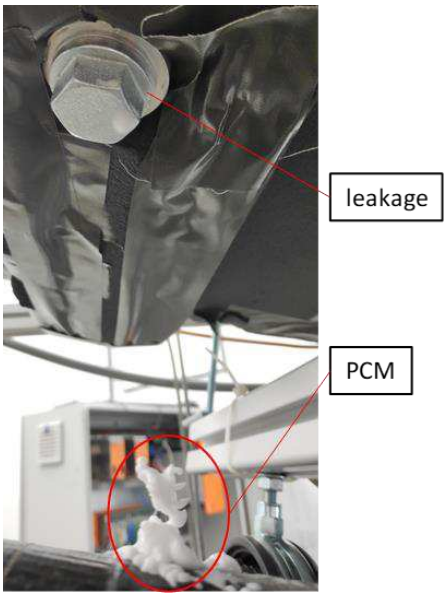

Figure 50 Picture of the leaked PCM from the RPW-HEX.

Another challenge that came with the implementation of the RPW-HEX appeared to be the oil supply for the compressor. Lubrication oil for the compressor circulated in the normal HP circuit without RPW-HEX. This was not possible anymore with the implementation of the RPW-HEX because the spatial volume of the circuit was enlarged, letting the compressor run dry. An oil separator had to be installed for this system. In addition, a vertical positioning of the RPW-HEX above the HP could help, letting the oil, which passes the oil separator, flow right back to the compressor instead of entering the circuit. This design decision is going to be implemented in the second version of the experimental setup.

4.2.1 Start-up

With the implementation of the thermal storage, the spatial volume of the refrigerant circuit increased dramatically. This was not a problem as long as the refrigerant did not condense inside this storage. Because if condensation occurred a large proportion of the refrigerant would accumulate there letting the other components of the circuit “dry out”. To avoid this problem, the temperature in the RPW-HEX during operation was always higher than the condensation temperature. In case the RPW-HEX was cold (after a long shut-down) a start-up procedure was developed. The main goal was to get the RPW-HEX exit temperature above the condensing temperature. In the left diagram of Figure 51, between minutes 10 and 20, the condensing temperature supersedes the RPW-HEX exit temperature because the compressor speed was raised too fast.

During the following experiments, the temperature of the RPW-HEX never was discharged to a temperature level where condensation could occur (see the right image of Figure 51). As a safety measurement, the minimum temperature difference ΔT (difference between condensing temperature and RPW-HEX exit temperature) was set to 1 K. If this value had been undercut the discharge process would have been stopped immediately.

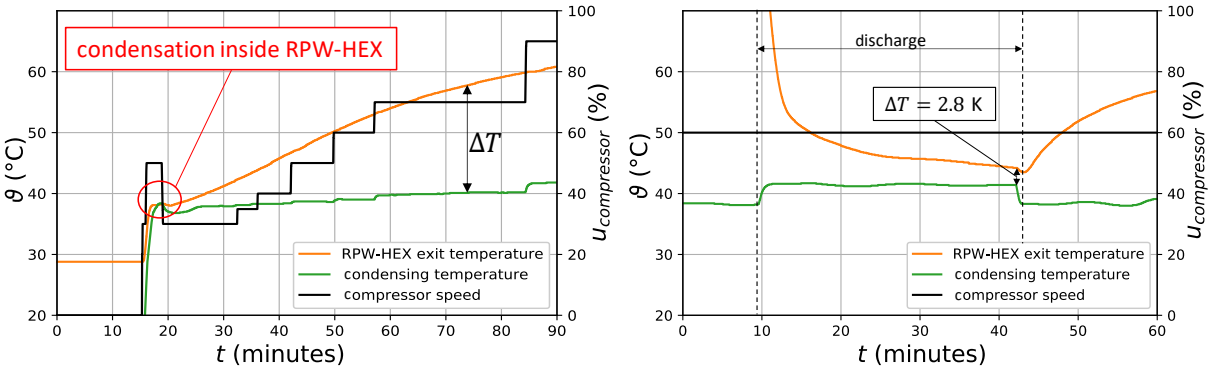

Figure 51: Refrigerant exit temperature of RPW-HEX. calculated condensing temperature and compressor speed during start-up and discharge. ΔT represents the temperature difference between the RPW-HEX exit temperature and the calculated condensing temperature. Left: Start-up procedure of the cold system. Right: Example of a discharge process with a constant compressor speed of 60%. ΔT does not undercut 1 K and the system stays warm.

With the implementation of a header in the refrigerant circuit, these measurements would not have been necessary. But the GWP of R-32 is still 675 times higher than the one of CO_2, therefore as little refrigerant as possible was used which prevents the use of a header in the refrigerant circuit.

4.2.2 Charging

To test the performance of the RPW-HEX, it was charged until the temperatures T-101 to T-114 reached a steady-state which took around 20 hours with the compressor speed set to 90%. The mean compressor exit temperature was 102 °C and the surface temperatures of the RPW-HEX reached their maximum between 85 °C and 90 °C. Figure 52 represents the charging process together with the melting temperature of the PCM. After 7 to 8 hours, the stored energy was solely sensible heat. A defrost was initiated three times which is visible as the surface and refrigerant exit temperatures dropped sharply because the compressor ran at a lower speed during each discharge.

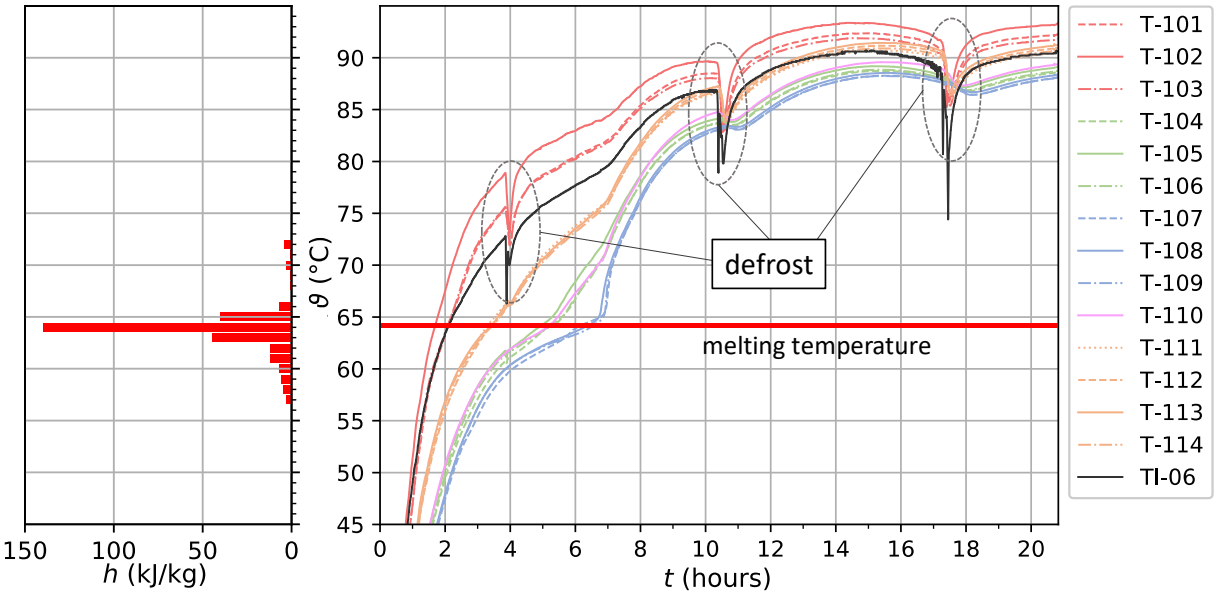

Figure 52: Right: Visualisation of Temperatures T-101 to T-114 and the compressor discharge temperature (TI-06) while being charged to full extent. Left: Partial melting enthalpy of the PCM RT64.

Looking at Figure 52, it is clearly noticeable that T-111 to T-114 (orange) displayed the second-highest temperatures throughout the whole charging process. From Figure 53 we can see that these four temperature sensors were located at the exit of the refrigerant. Naturally, the temperatures in this area are expected to be the coolest. From this, it can be deduced that a thermal bridge was developing inside the RPW-HEX. This can be attributed to the high proportion of aluminum (72% of total mass), since aluminum ($\lambda_{\text{aluminium}} \approx 200$ Wm^{-1}K^{-1}) has an approximately 1000-times higher thermal conductivity than RT64 ($\lambda_{\text{RT64}} \approx 0.2$ Wm^{-1}K^{-1}).

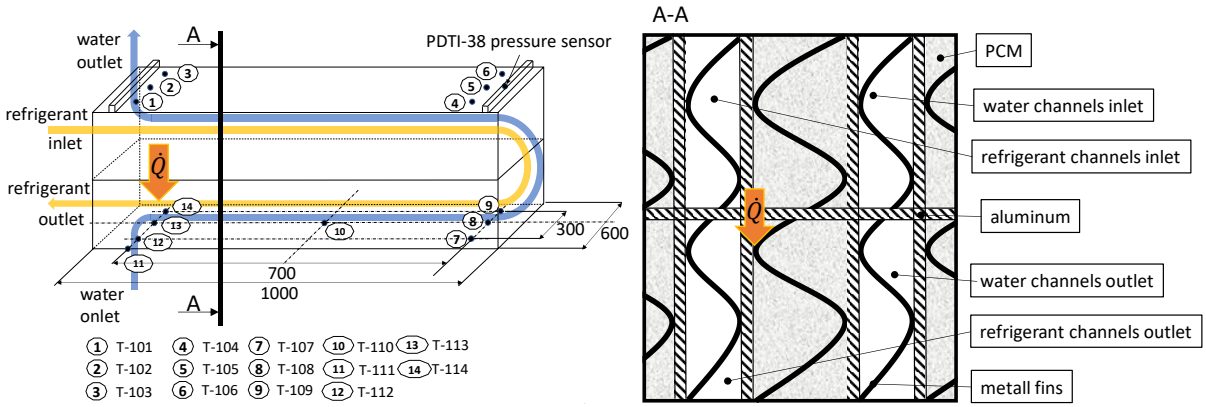

Figure 53: Left: Schematic illustration of the RPW-HEX. Right: Cross-section of the RPW-HEX.

The area behind the U-turn of the refrigerant, indicated by T-107, T-108 and T-109, took the longest to heat up and was, therefore, the coldest area in the RPW-HEX. Approximately after 13 hours, the refrigerant exit temperature TI-06 was getting colder than T-112, T-113, and T-114 (see Figure 52). This meant that the refrigerant cooled down while passing T-101 to T-109 and got heated up again at the exit of the RPW-HEX. Also, the refrigerant exit temperature TI-06 was significantly higher than the temperatures T-111 to T-114, which indicated a low heat transfer rate between the RPW-HEX and the refrigerant.

This effect led to the conclusion, that with this design of the RPW-HEX, the heat was conducted faster through the aluminum than it was transferred by the refrigerant. One attempt to solve this

problem would be to separate the upper and the lower part with an insulation layer. The heat transfer between the refrigerant and the aluminum could also be enhanced. This could be achieved by redesigning the RPW-HEX with smaller refrigerant channels, forcing the refrigerant to flow at higher velocities. In addition, the length of the refrigerant channels could be extended by redirecting the refrigerant more often through the RPW-HEX, which would also improve the heat transfer between refrigerant and RPW-HEX. These design improvements are going to be implemented in the second version of the RPW-HEX by *AKG*.

4.2.3 Discharge case 1

To determine the maximum storable energy in the RPW-HEX, the compressor was turned off bevor the *discharge case 1* was started. The supply water mass flow was set to 0.14 kgs^{-1} and the RPW-HEX was discharged completely. In Figure 54, the temperature distribution of the surface of the RPW-HEX is shown. At 64 °C (indicated by the upper blue line) the curves showed a plateau which indicates the solidification in the PCM. On the left-hand side, the partial enthalpy from 58 °C to 72 °C is depicted. At 64 °C, the PCM provided ~100 $kJkg^{-1}$ while solidifying, and at 61 °C the partial enthalpy had another small peak of 50 $kJkg^{-1}$. As T-101, T-102 and T-103 passed 58 °C they displayed a dent that indicates the second solidification peak, but at a lower temperature than it has been observed in the *mini-LHS*. One possible explanation for this is that the heat transport from the aluminum to the PCM was too low. Therefore, the aluminum cooled faster than the PCM and the temperatures displayed were lower than the actual temperatures inside the PCM. But this is rather unlikely since the first solidification plateau occurred at exactly 64 °C which correlated perfectly with the measured data from the *mini-LHS*. Another possible explanation is the effect of subcooling, which has been observed by others as well (Mehling et al., 2017; Rathgeber et al., 2018; Zahir et al., 2019). With higher cooling rates the solidification happens at lower temperatures. After 35 minutes the RPW-HEX was completely empty as all temperatures reached 33 °C, which was the water inlet temperature.

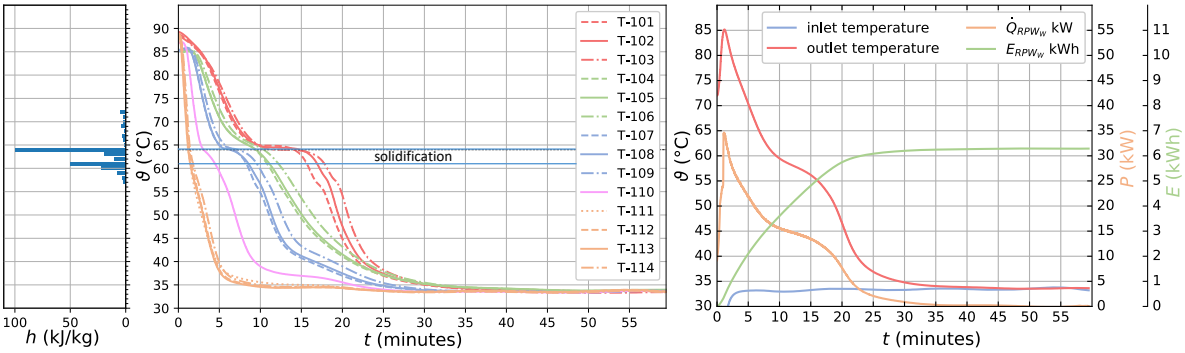

Figure 54: Results of the first discharging test with HP turned off. Left: Partial melting enthalpy of RT64. Middle: Temperatures T-101 to T-114 of the RPW-HEX surface. Right: Water inlet and outlet temperature as well as the derived thermal power and energy from the RPW-HEX.

A total amount of 6.28 kWh was drawn from the RPW-HEX (see the right image in Figure 54). The water exit temperature peaked at 85 °C after 2 minutes. In the first 3 minutes, the water inlet temperature did not reach the actual 33 °C because stagnant water from the pipes was being flushed through the RPW-HEX with a temperature of 28 °C. This led to a power peak of $\dot{Q}_{\mathrm{RPW_W}}$. Between minutes 10 and 15 the gradient of the water outlet temperature decreased. At minute 20 the heat storage was almost empty as the water outlet temperatures declined rapidly. This means that the remaining heat inside the RPW-HEX was of sensible nature. The energy $E_{\mathrm{RPW_W}}$ levels out horizontally shortly afterwards.

4.2.4 Discharge cases 2,3,4

In Figure 55, Figure 56, and Figure 57 the temperatures, measured on the RPW-HEX surface, are plotted. With rising compressor speed values, the discharging time increased. For the discharge process, with a compressor speed of 45%, the water mass flow was also reduced to 0.114 kgs^{-1}. Obviously, this had a positive effect on the discharging time, which is why the discharge process with 45% compressor speed took as long as the discharging process with 90% compressor speed.
Looking at Figure 55, Figure 56, and Figure 57 the energy does not level out horizontally compared to Figure 54. The RPW-HEX functioned as a heat exchanger between the water and the refrigerant gas. Therefore, the RPW-HEX power never reached zero. In addition to that, the water inlet temperature was constantly higher compared to the *discharge case 1* where the HP was not operating, because the water got heated up by the condenser before entering the RPW-HEX. Hence also the power of the RPW-HEX $\dot{Q}_{\mathrm{RPW_W}}$ was smaller except for the peak in the beginning. The power peak in Figure 56 was smaller compared to all other discharge cases because the water mass flow was reduced. In the first 10 minutes of this discharge case, the HP switched itself off because the necessary water mass flow of 0.113 kgs^{-1} was undercut. This led to the uneven water inlet temperature and an uneven power resulting from inlet and outlet temperature.

In Table 4 the total amounts of energy drawn from the RPW-HEX in one hour are listed. Temperatures of the RPW-HEX at the beginning of the *discharge case 2* were between 80 °C and 85 °C instead of 85 °C to 90 °C. For that reason, the thermal energy of the *discharge case 2* was not higher than the energy of the *discharge case 1*.

In general, it was observed that with prolonged discharging time the solidification peaks got accentuated due to the direct heat transfer from the refrigerant to the water. The solidification peaks themselves were independent of the discharging time as they are material inherent. In addition, the second plateau in the temperature curves had the tendency to occur at lower temperatures with higher cooling rates. This may be a delayed solidification that occurs at faster cooling rates which also was reported in Mollova et al., 2013.

Table 4: Compressor speed and thermal energy of all four discharge cases.

test	compressor speed (%)	thermal energy (kWh)
discharge case 1	0	6,28
discharge case 2	45	6,26
discharge case 3	56	7,15
discharge case 4	90	7,73

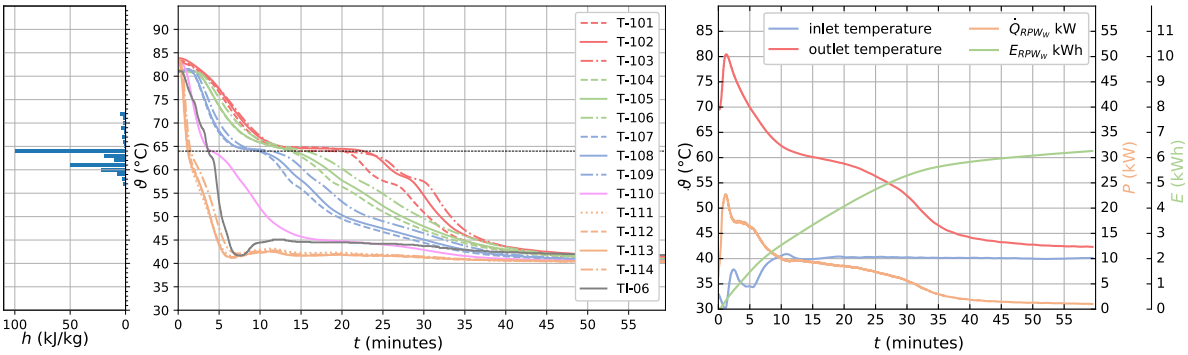

Figure 55: Results of *discharge case 2*. Left: Partial melting enthalpy of RT64. Middle: Temperatures T-101 to T-114 of the RPW-HEX surface and the refrigerant exit temperature TI-06. Right: Water inlet and outlet temperature as well as the derived thermal power and energy from the RPW-HEX.

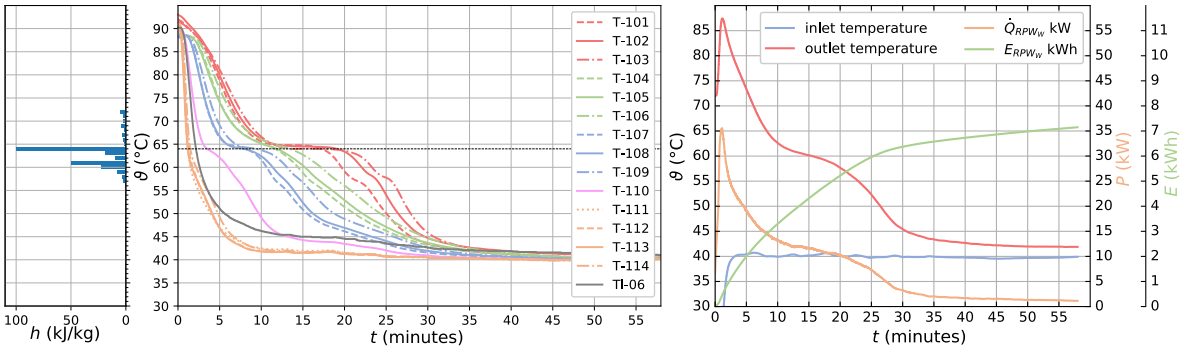

Figure 56: Results of *discharge case 3*. Left: Partial melting enthalpy of RT64. Middle: Temperatures T-101 to T-114 of the RPW-HEX surface and the refrigerant exit temperature TI-06. Right: Water inlet and outlet temperature as well as the derived thermal power and energy from the RPW-HEX.

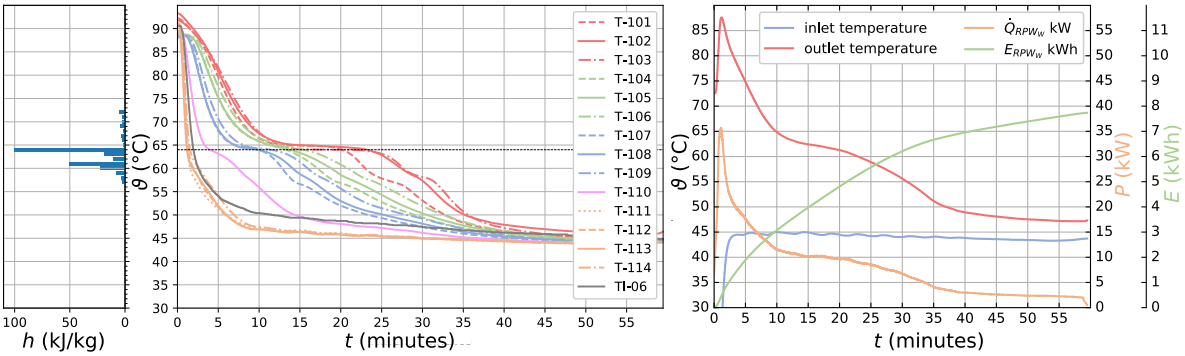

Figure 57: Results of *discharge case 4*. Left: Partial melting enthalpy of RT64. Middle: Temperatures T-101 to T-114 of the RPW-HEX surface and the refrigerant exit temperature TI-06. Right: Water inlet and outlet temperature as well as the derived thermal power and energy from the RPW-HEX.

4.2.5 A-7W43_I and A-7W43_II

During the *A-7W43_I*, the temperature inside the climatic chamber was set to -7 °C and air humidity to 75%. The HP was powered by AC. The supply temperature of the water was set to 34 °C resulting in a water condenser exit temperature for heating of 43 °C. The HP continuously charged the RPW-HEX. As soon as the three lowest temperatures (T-107, T-108, T-109) reached 70 °C the discharge was started and stopped immediately as the RPW-HEX water exit temperature reached 55 °C. Water mass flow was set to 0.14 kgs^{-1} during discharging and 0.25 kgs^{-1} during charging the RPW-HEX. Seven cycles were conducted with the discharge approach I (see Figure 58). In the following, the 7th cycle is described to explain the behavior of the system at this operating point.

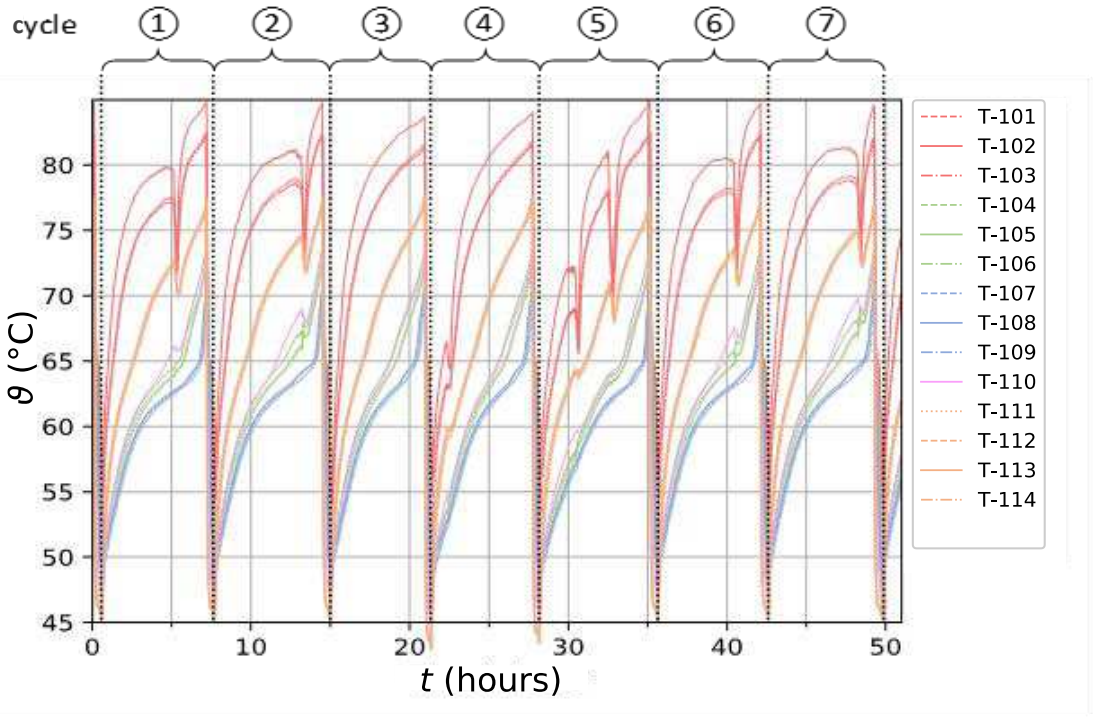

Figure 58: Surface temperatures of the RPW-HEX over a time period of 50 hours. The graph shows 7 cycles.

In Figure 59, the 14 temperatures of the RPW-HEX and the refrigerant exit temperature are plotted throughout a whole charging plus discharging cycle. Since T-101, T-102, and T-103 were located at the inlet of the refrigerant gas and the exit of the water channels, they always displayed the highest temperatures. The strong dent in the temperature curves between five and six hours represents a defrosting process.

Again, T-111, T-112, T-113, and T-114 displayed higher temperatures than the other sensors (T-104 to T-110) even though they were located at the refrigerant gas exit where the lowest temperature is expected. When being discharged with water, this effect could not be observed. The heat transfer between the RPW-HEX and the water was much higher, therefore the temperatures dropped in the same order as the water passed through them.

As T-107, T-108, and T-109 passed 65 °C after about 6.5 hours the PCM was completely melted.

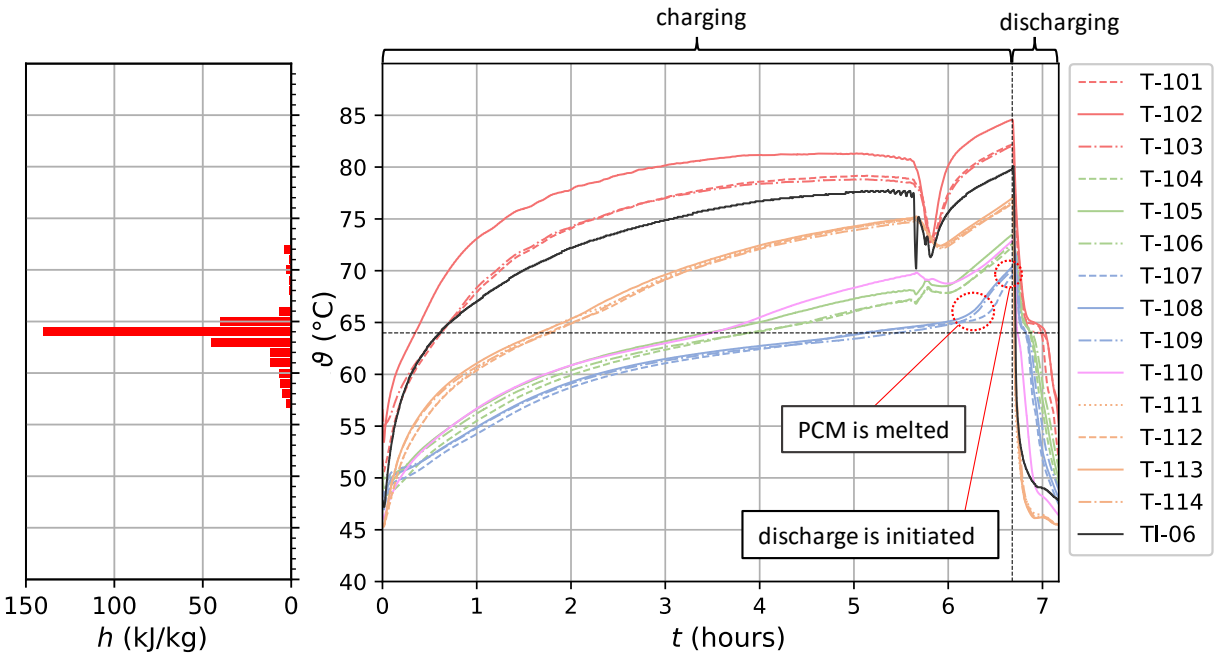

Figure 59: Left: Partial melting enthalpy of RT64. Right: Surface temperatures and RPW-HEX refrigerant exit temperature are plotted over a whole cycle (charging and discharging).

In Figure 60 thermal powers over time for the seventh cycle (charging and discharging) are plotted. The loss of refrigerant power (red) during the charging cycle had two main reasons. First of all, the temperature difference between inlet and exit temperature declined as the RPW-HEX was being charged. Secondly, to limit the compressor hot gas exit temperature the liquid injection valve opened more gradually. The refrigerant which flew through the liquid injection valve bypassed the flow measurement unit FTI-8. For this reason, the power of the refrigerant could only be estimated and not calculated accurately. The estimated refrigerant mass flow, however, declined when the liquid injection opened.

Between hours 5 and 6, the power dropped radically. This was because of a defrosting. The total power turned negative and so did the condenser power because the condenser acted as evaporator during this time.

When the discharging process started, a drop in the condenser power $\dot{Q}_{\mathrm{Cond}}$ was observable. The resulting lower condenser power was due to a lower water mass flow. The short steep drop of the condenser power to 5 kWh can be explained by looking at the condenser water exit temperature (TI-23 in Figure 62) and the mass flow rate ($\dot{m}_{\mathrm{W}}$ in Figure 61). For the discharging process, the mass flow rate was being reduced which could be measured almost instantly. But by reducing the mass flow, the condenser exit temperature naturally rose. This happened with a certain delay of about 2 minutes (see Figure 62). While the exit temperature was still low as well as the mass flow, the condenser power reached a minimum. After that, it rose together with the condenser exit temperature TI-23.

During the discharging process, the condenser power declined steadily while the power of the refrigerant through the RPW-HEX rose. The refrigerant experienced a higher temperature difference through the RPW-HEX as it got discharged and eventually reached its initial power of about 2 kW. At the same time, the condenser lost power because the inlet temperature of the refrigerant into the condenser declined (see TI-06 in Figure 59).

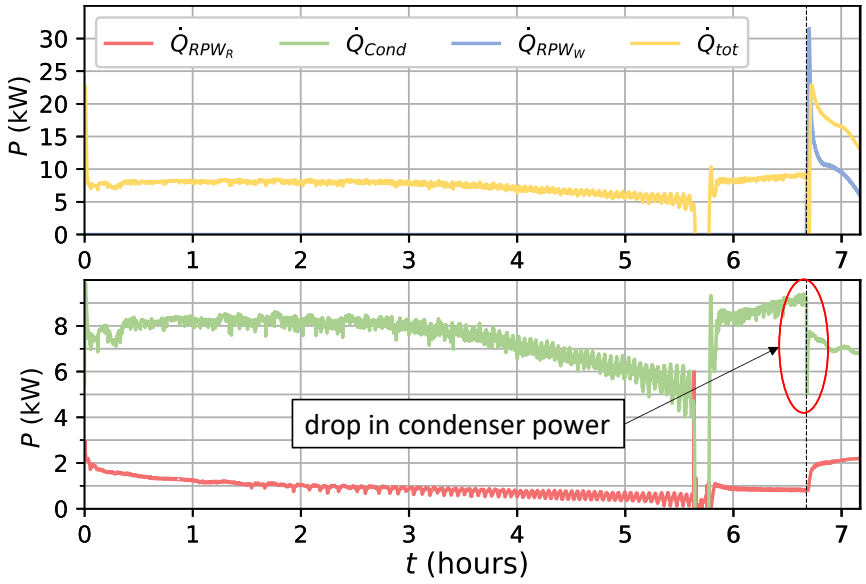

Figure 60: Powers the system provided over the 7th cycle in *A-7W43_I*. Top: Total power and RPW-HEX power derived from the waterside. Bottom: Condenser power and RPW-HEX Power derived from the refrigerant side.

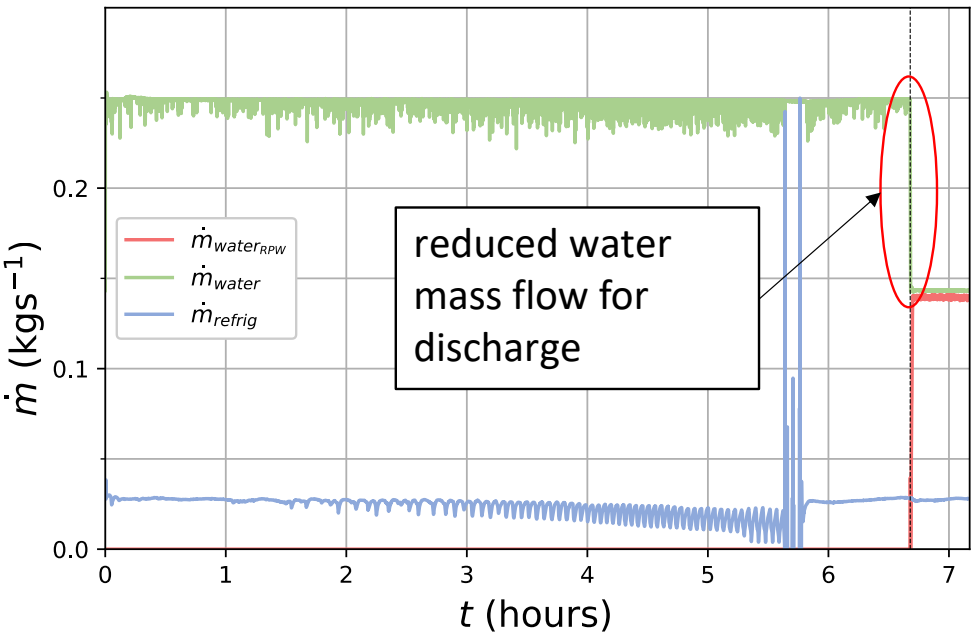

Figure 61: Water and refrigerant mass flow in the 7th cycle of *A-7W43_I*.

In Figure 61 the mass flow of the refrigerant declined during the charging process until a defrost was conducted. After the defrost the refrigerant mass flow returned to its original value. In reality, the refrigerant mass flow was not reduced, rather the liquid injection valve opened up further and part of the refrigerant mass flow bypassed the FTI-08.

In Figure 62 $\dot{Q}_{\mathrm{RPW_W}}$ (blue) reached a maximum shortly after the discharging process was being started. This maximum originated from the peak in TI-26 and the low of TI-34. The peak in TI-26 represents the hot water which was resting inside the RPW-HEX during the charging. At the same time, the stagnant cold water from the piping system in front of the RPW-HEX got pushed past TI-34. For a short period of time, the temperature difference between TI-34 and TI-26 was 55 °C resulting in the power peak. At the same time $\dot{Q}_{\mathrm{tot}}$ (yellow) experienced a low. The system exit

temperature TI-34 dropped below the system inlet temperature TI-17 as stagnant water from the pipes passed the TI-34 sensor. The result was a negative total power $\dot{Q}_{\mathrm{tot}}$.

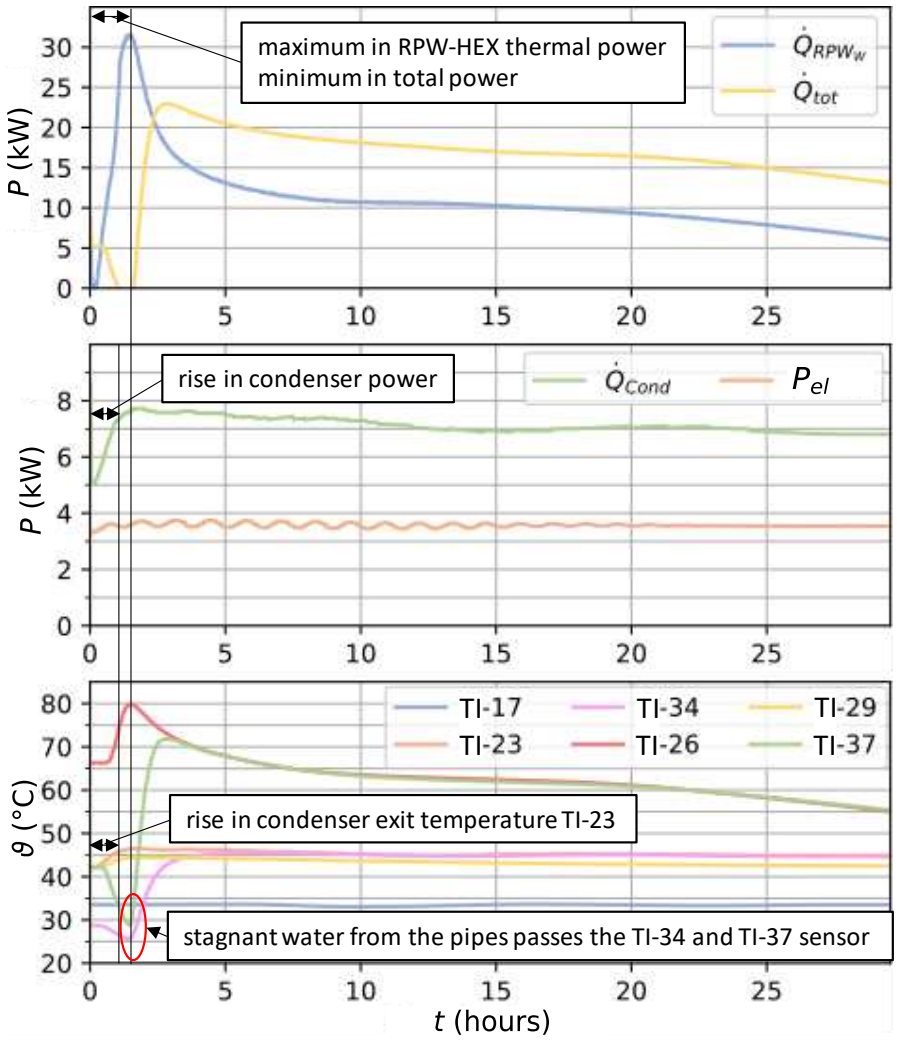

Figure 62: Thermal powers and water temperatures during the discharging process of the 7th discharge in *A-7W43_I*.

If the energy of the RPW-HEX ($E_{\mathrm{RPW_W}}$) and the energy of the condenser (E_{Cond}) were added up, they resulted in a higher energy than the total energy provided by the system (see the right image in Figure 63). This occurred because of the effect described above. The thermal power $\dot{Q}_{\mathrm{RPW_W}}$ had a maximum while the total thermal power $\dot{Q}_{\mathrm{tot}}$ was experiencing a minimum at the beginning of the discharging process. This is being illustrated with E_{loss}. Notice that E_{loss} was smaller than the illustrated losses in the bar-plot (grey). The bar plot includes thermal losses throughout the whole charging cycle. In this cycle, the thermal losses would therefore account to 0.51 kWh. With a charging time of 6.7 hours, the RPW-HEX lost approximately 75 W.

In conclusion, the RPW-HEX delivered more energy than the system was actually providing because it covered heat losses of stagnant water in the piping.

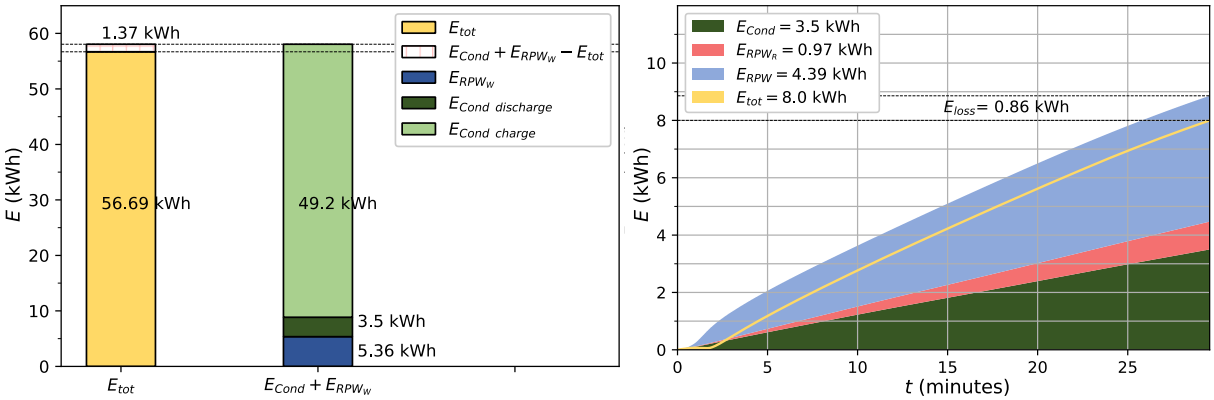

Figure 63: Energies transferred to the water cycle in the 7th cycle of *A-7W43_1*. Left: Barplot showing the total energies during the whole cycle. Right: Stackplot showing the energies transferred during discharging.

The decrease of the refrigerant mass flow resulted from the closing of the expansion valve and the opening of the liquid injection valve as frost accumulated on the evaporator (see Figure 64). The evaporator lost efficiency and could not heat the refrigerant sufficiently. As the frost progressed, which is indicated by the ascending scale, the pressure at the compressor inlet and thereby outlet declined. The expansion valve closed to compensate for the performance loss of the evaporator, reducing the refrigerant mass flow. As the frosting condition became severe the expansion valve started to oscillate. This had the negative side effect that the compressor exit temperature had to be controlled with the liquid injection valve which opened further to prevent temperatures above 103 °C at the compressor exit. With an oscillating expansion valve, the scale measured small changes in weight because the refrigerant mass flow was wavery.

Just before hour 5, the HP started to lower the compressor speed automatically. Usually, at this point, a defrost was initiated but the HP control failed to do so. This is an indication that the control of the HP was not yet fully developed for operations with an implemented RPW-HEX. After an hour of faulty operation, the defrost was finally executed.

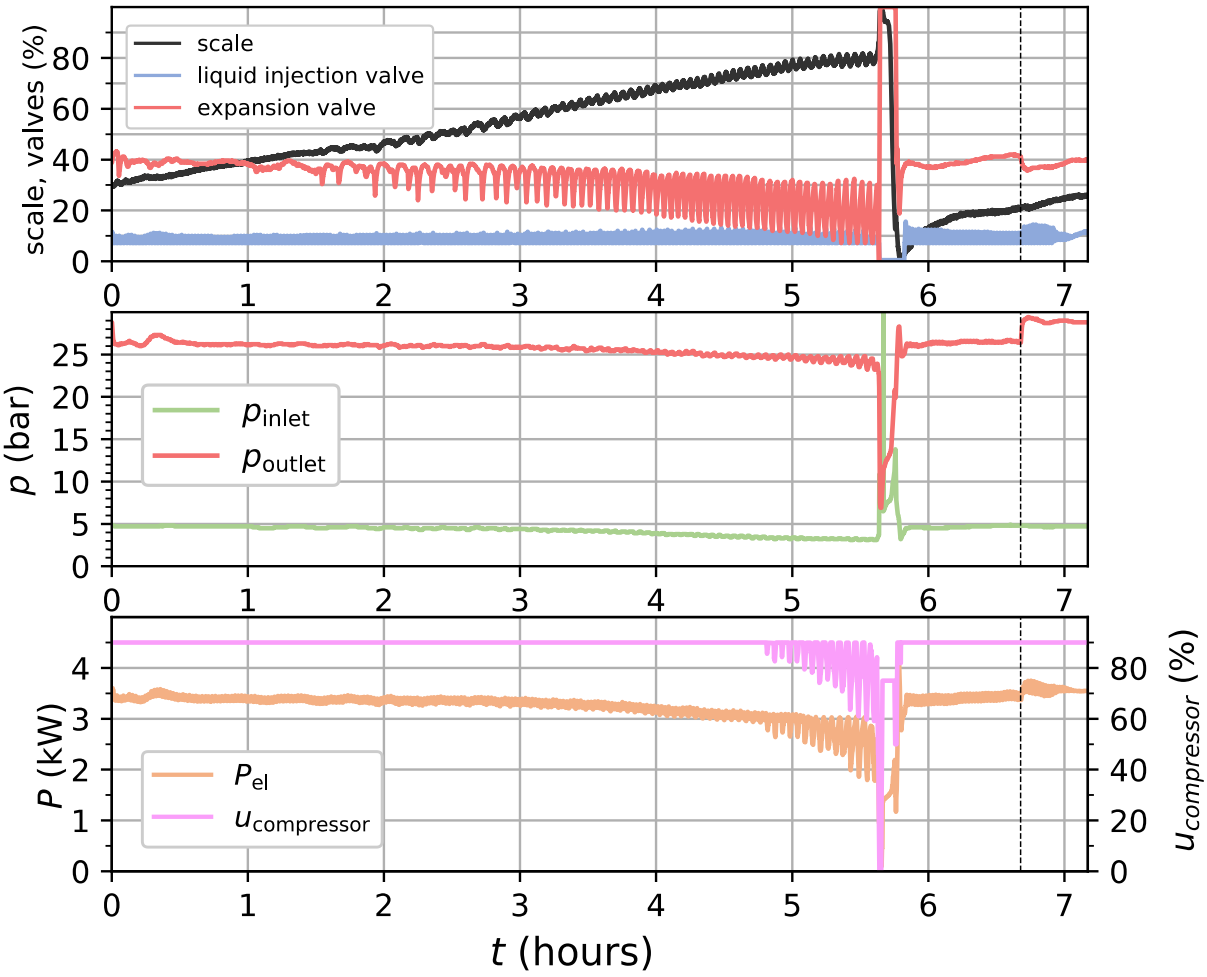

Figure 64: Results of the 7th cycle of *A-7W43_I*. Top: Scale measurement and the degree of opening of liquid injection as well as expansion valve. The scale measurements are divided by its highest value to acquire the change in weight in (%). Middle: Pressure at compressor in- and outlet. Bottom: Electrical power and compressor speed.

Table 5 shows the PF for all seven cycles as well as the thermal energy provided by the system. The 3rd cycle stuck out with a better PF and lower thermal energy because in this cycle the condenser power was higher than in the other cycles. This resulted in a shorter charging time. Thus, the total thermal energy provided is lower. The reason for this was a defrost happening at the very start of the cycle. Figure 65 shows the thermal and electrical power as well as the resulting thermal and electrical energy of the 7th cycle compared to the 3rd cycle.

Table 5: Thermal energy and performance factor for all cycles in *A-7W43_I*.

cycle	T_{amb} (°C)	RH_{amb} (%)	TI-37 (°C)	$E_{thermal}$ (kWh)	PF
1	-6.38	73.56	42.03	57.45	2.55
2	-6.37	70.67	41.83	57.73	2.51
3	-6.19	70.96	42.43	54.92	2.67
4	-6.29	70.08	42	55.73	2.57
5	-6.22	72.19	41.59	57.35	2.49
6	-6.26	70.54	42.22	57.7	2.59
7	-6.28	70.89	42.02	58.06	2.56

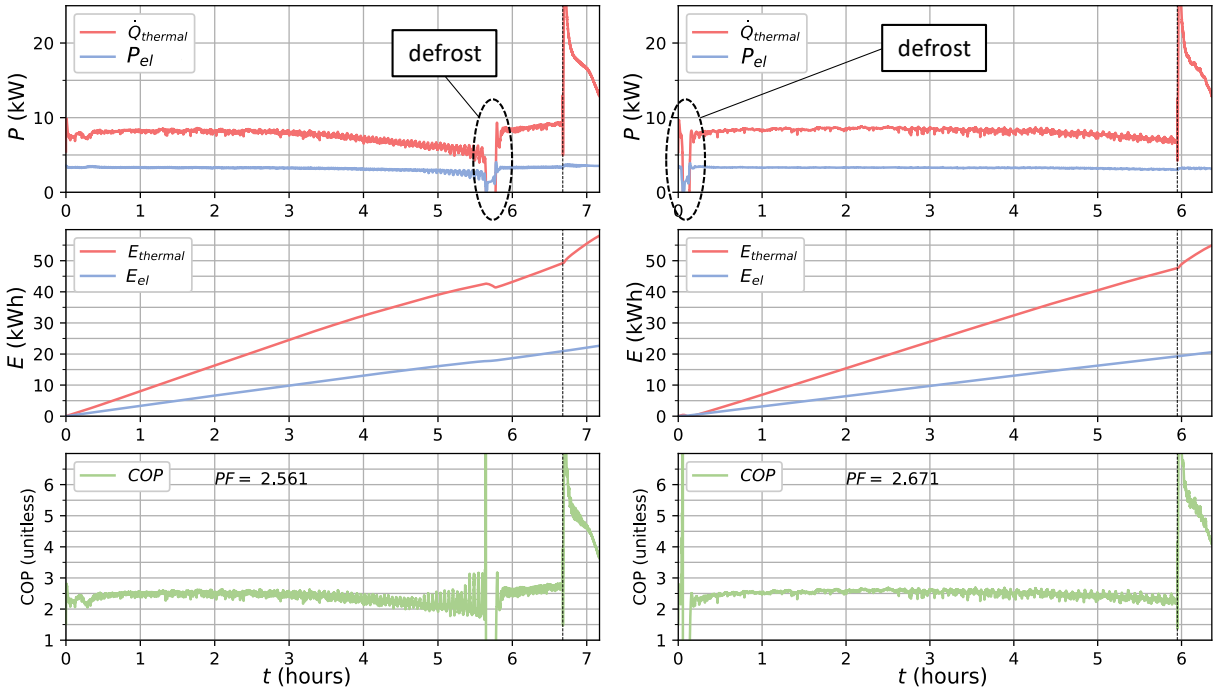

Figure 65: Comparison of thermal and electric Power/Energy and the resulting COP of the 7th cycle (left) and the 3rd cycle (right) in *A-7W43_I*. Top: Thermal and electric power. Middle: Thermal and electric energy. Bottom: COP

To calculate the PF of this system the electric energy was compared to the thermal energy throughout the whole cycle. With

$$E_{\text{thermal}} = E_{\text{RPW}_\text{W}} + E_{\text{Cond}} \quad \textbf{(24)}$$

ignoring part of the thermal losses in the pipes. The performance factors yielded 2.56 and 2.67. The better PF was solely due to the early defrost in the cycle. In Figure 65 the thermal power decreased while the electrical energy stayed steady. The COP which resulted from these two values decreased consequently.

In conclusion, the defrost had the largest impact on the performance of the system. If the defrost would have been conducted fast without a period where the compressor slowed down, the performance of the system would have enhanced dramatically.

Five cycles were carried out testing the discharge approach II at an ambient air temperature of -7 °C (*A-7W43_II*). In Table 6 the results for the thermal energy and the PF for these five tests are shown. They differed strongly from the test series where discharge I was used even though the ambient air temperature and humidity were similar.

Table 6: Thermal energy and performance factor for all cycles in *A-7W43_II*.

cycle	T_{amb} (°C)	RH_{amb} (%)	TI-37 (°C)	E_{thermal} (kWh)	PF
1	-6.61	71.19	40.50	65.31	2.42
2	-6.35	72.45	41.57	57.83	2.51
3	-6.59	71.44	40.92	58.06	2.45
4	-6.35	71.37	41.39	55.98	2.45
5	-6.74	71.43	41.56	56.04	2.49

In Figure 66 the PF of the *A-7W43_I* and *A-7W43_II* series are being compared. The PF in *A-7W43_II* is significantly lower in almost every cycle.

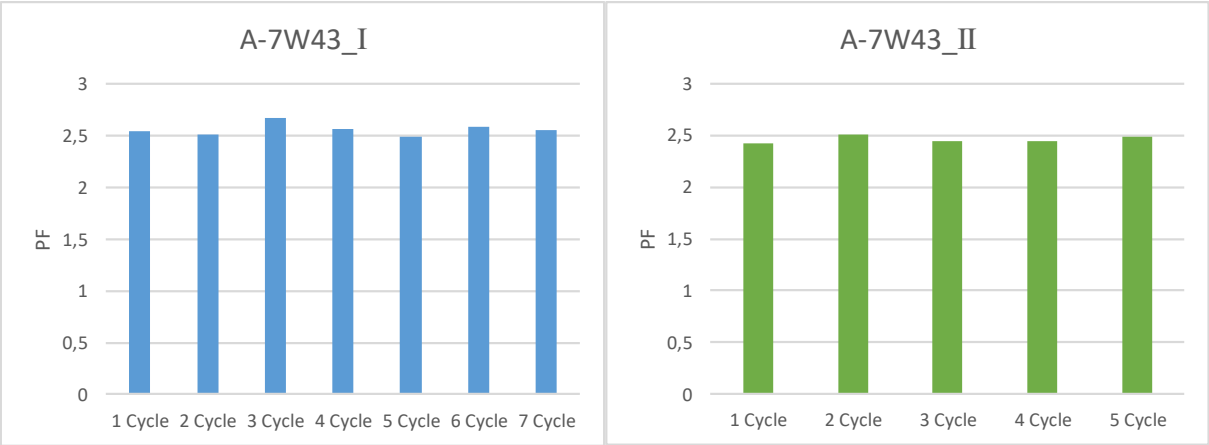

Figure 66 Results for PF of *A-7W43_I* and *A-7W43_II*. Left: *A-7W43_I*. Right: *A-7W43_II*.

The reason for the different performance was not the different approach in discharging the RPW-HEX. Rather the automatic control failed completely to initiate a defrost in *A-7W43_II*. To explain this the 1st cycle is used in Figure 67. As the frost progressed the expansion valve closed more frequently, and the compressor reduced its speed. The expansion valve closed to 10% and the liquid injection valve was opened to 10% meaning that around 50% of the refrigerant mass flow was bypassing the evaporator. Thus, the performance of the HP diminished. Notice that also the pressure at compressor in- and outlet was reduced during the faulty operation. This resulted in a lower condensing temperature. Therefore, the thermal power $\dot{Q}_{\mathrm{thermal}}$ dropped close to the value of P_{el} resulting in a very low COP. As soon as the defrost was performed the system regulated itself again. The curves for electrical and thermal energy did no longer overlap.

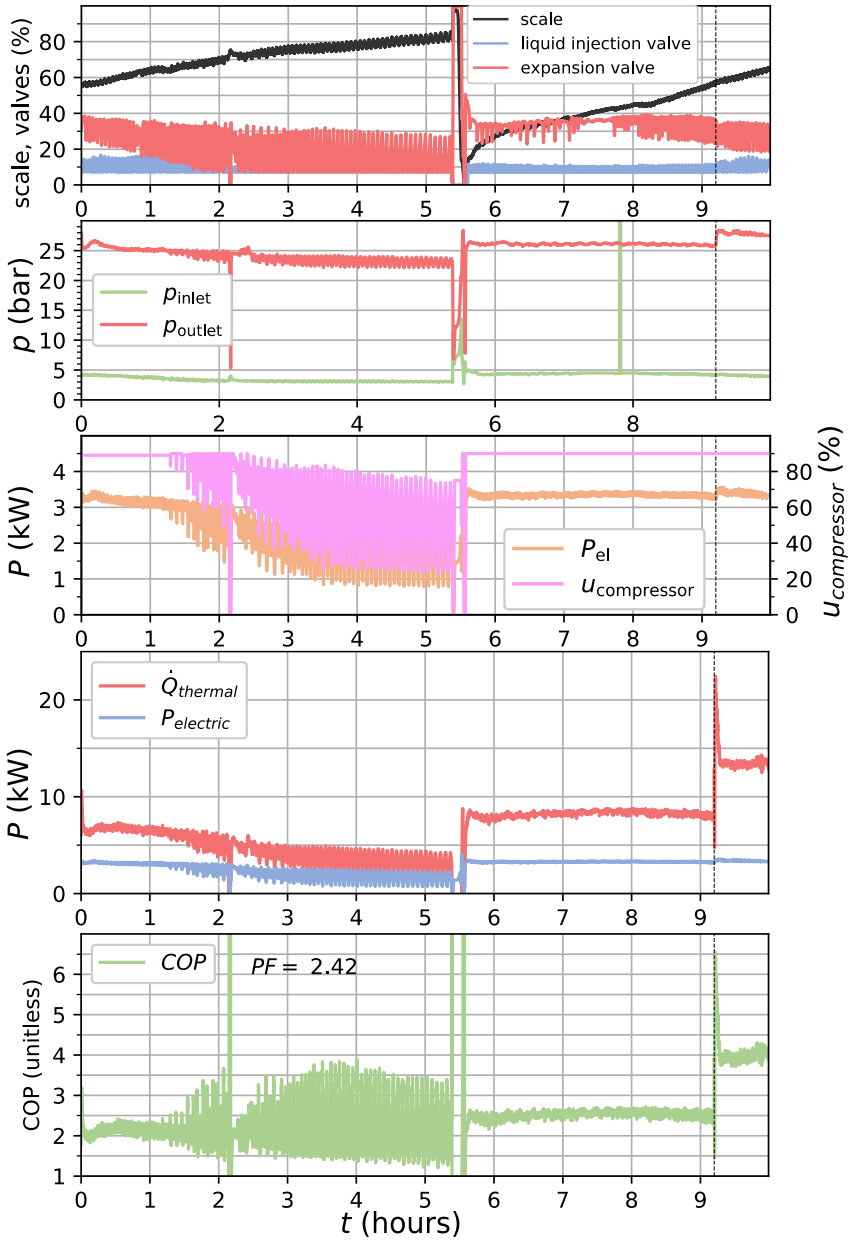

Figure 67: Results of the 1st cycle of *A-7W43_II*. Top: Scale, liquid injection valve and expansion valve. Second: Compressor inlet and outlet pressure. Third: Compressor speed and electric power. Fourth: Thermal and electric power in comparison. Bottom: Resulting COP is illustrated. The PF which represents the mean COP accounts to 2.42.

Contrary to the whole cycle, the discharge cycles of the *A-7W43_II* were supposed to distinguish themselves from the first cycle. By regulating the hot water temperature to 55 °C the water mass flow through the RPW-HEX was reduced which led to longer discharging times. Comparing the PF in Table 7 and Table 8 it is obvious that in the second series the discharge performance was significantly lower. This was also on account of the weak performance of the condenser in *A-7W43_II*.

Table 7: Thermal energy and performance factor of all discharging tests in *A-7W43_I*.

cycle	T_{amb} (°C)	RH_{amb} (%)	TI-37 (°C)	$E_{thermal}$ (kWh)	PF
1	-6.15	73.4	60.52	8.87	5.03
2	-6.49	73.9	60.53	8.83	5.06
3	-6.55	68.13	60	7.32	5.55
4	-6.41	66.68	60.15	7.74	5.37
5	-5.95	72.15	60.56	8.85	5.05
6	-6	73.8	60.6	8.91	5.03
7	-6.28	75%	60.5	8.86	5.03

Table 8: Thermal energy and performance factor for all discharge cycles in *A-7W43_II*.

cycle	T_{amb} (°C)	RH_{amb} (%)	TI-37 (°C)	$E_{thermal}$ (kWh)	PF
1	-6.16	71.2	53.86	10.82	4.04
2	-6.36	70.53	53.75	8.92	4.41
3	-6.37	69.67	53.9	9.1	4.33
4	-6.11	66.45	54.09	9.24	4.14
5	-5.96	69.72	54.13	10.63	4.1

The provided thermal energy was significantly higher with discharge approach II. Hence, a higher amount of DHW was produced even though the system had a worse performance. This difference is visualized in Figure 68.

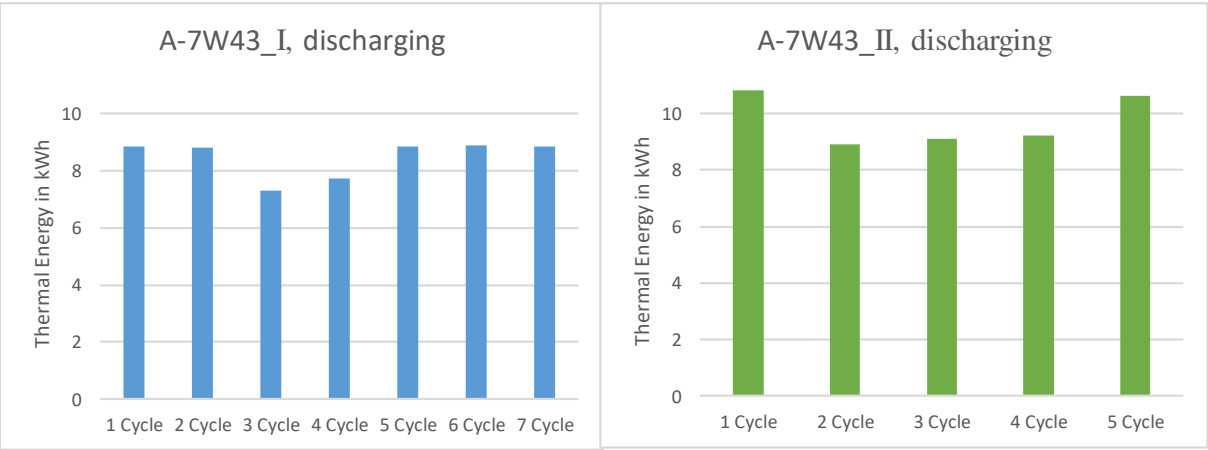

Figure 68 Results for PF of the *A-7W43_I* and *A-7W43_II* during discharge only. Left: *A-7W43_I*. Right: *A-7W43_II*.

However, in between the five cycles that have been tested this way, the discharging time varied strongly, which was also reflected in the extracted energy. This highlights how strong the influence of the condenser's performance affected the discharge. The RPW-HEX was always at the same state of charge before being discharged and provided approximately 4.5 kWh. Consequently, the difference in thermal energy was dependent on the energy the HP provided during the discharge.

The 1st and the 2nd cycle in *A-7W43_II* exhibited the greatest discrepancy in provided thermal energy while discharging. Figure 69 displays the thermal energies drawn from the RPW-HEX for these two cycles. While E_{RPW} remained the same E_{Cond} and E_{RPW_R} differentiated strongly from each other. The mean condenser exit- and therefore the RPW-HEX inlet water temperature for the 1st cycle was 42.3 °C and for the 2nd cycle, it was 40.95 °C. This underlines the weak performance of

the condenser in the 2nd discharge cycle which also reduced the discharging time. The weaker performance was attributed to more frost on the evaporator.

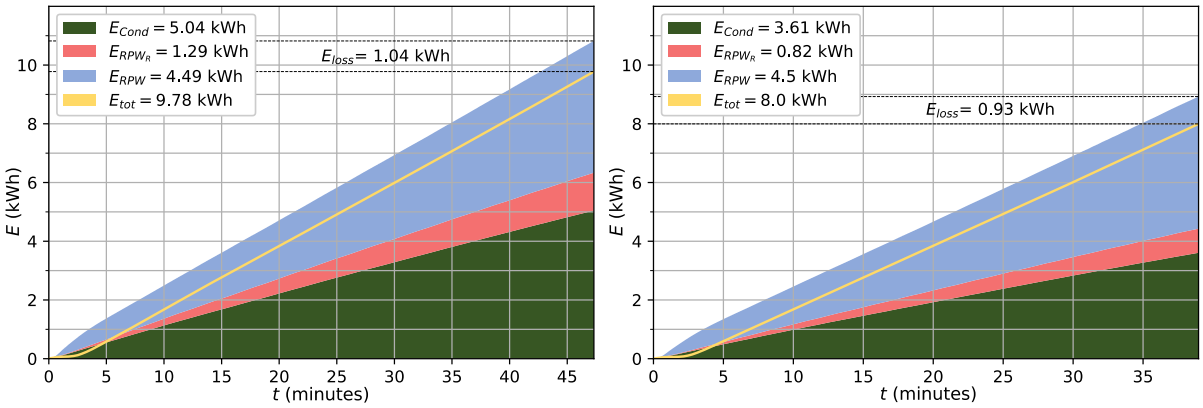

Figure 69: Stackplots showing energies of discharge cycles in *A-7W43_II*. Left: Energy transferred to the waterside in the 1st discharge cycle. Right: Energy transferred to the waterside in the 2nd discharge cycle.

4.2.6 A2W37_W37_I and A2W37_W37_II

A2W37_I and A2W37_II were conducted with an outside air temperature of 2 °C and relative air humidity of 85%. The HP was powered by DC instead of AC. The water return temperature was set to 31 °C and was being heated up to 37 °C. The domestic hot water was being produced by discharging the RPW-HEX until the water exit temperature of the RPW-HEX reached 55 °C.

Under these conditions, frosting of the evaporator was accelerated. For these tests, no refrigerant mass flow was being measured because in this operating mode it was two-phased, meaning it didn't condense completely in the condenser. The CORIOLIS mass flow measurement (FTI-8) which was located in front of the expansion valve, was not able to measure a two-phase medium. Compared to the tests which were performed at an ambient air temperature of -7 °C the provided thermal energy in one cycle was much higher (see Table 9 and Table 10).

Table 9: Thermal energy and performance factor for all cycles in *A2W37_I*.

cycle	T_{amb} (°C)	RH_{amb} (%)	TI-37 (°C)	$E_{thermal}$ (kWh)	PF
1	2.1	68	37.21	75.21	3.32
2	2.26	70.29	37.49	80.91	3.5

Table 10: Thermal energy and performance factor for all cycles in *A2W37_II*.

cycle	T_{amb} (°C)	RH_{amb} (%)	TI-37 (°C)	$E_{thermal}$ (kWh)	PF
1	2.16	67.28	37.2	75.18	3.36
2	2.13	70	37.29	76.48	3.32
3	2.37	68.33	37.46	78.34	3.42
4	2.03	69.47	36.68	71.59	3.11

Compressor speed was set to 60% rather than 90%. Consequently, the charging of the RPW-HEX took much longer resulting in a higher total amount of provided thermal energy. To describe *A2W37_I* the 2nd cycle is used. As one can see in Figure 70 it took over 12 hours until the temperatures T-107. T-108 and T-109 reached 70 °C. During this time a defrost was carried out twice.

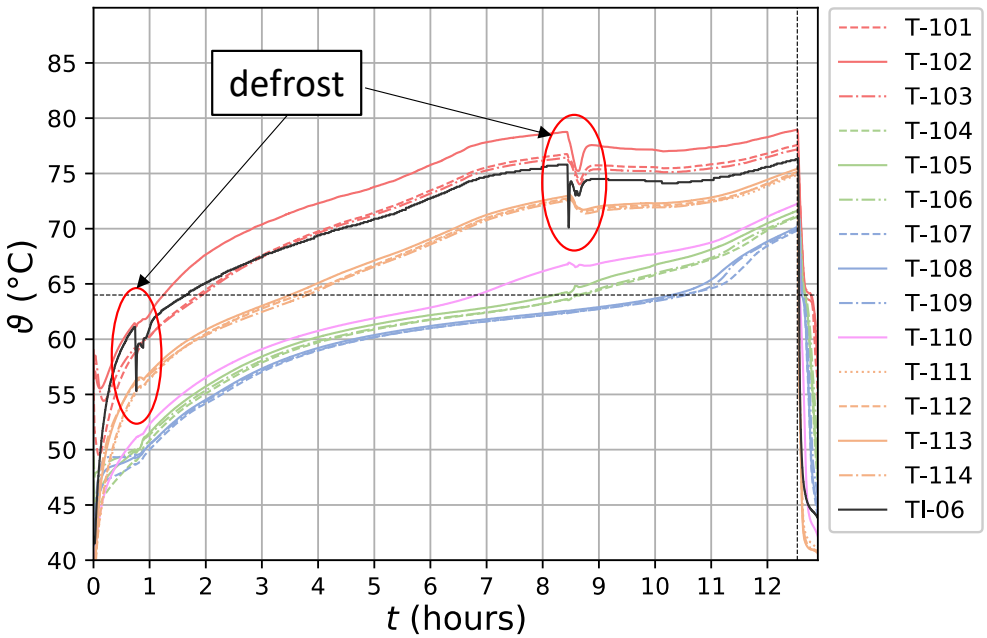

Figure 70: Temperatures of the RPW-HEX together with the refrigerant exit temperature plotted over the 2nd cycle of *A2W37_I*.

The PF was significantly higher than in the previous tests *A-7W43_I* and *A-7W43_II*. On the one hand, this could be traced back to the higher ambient air temperature. On the other hand, based on the findings from the previous testing, automatic defrosting algorithms were modified to better meet the requirements. In Figure 71 the compressor did not lower his speed before a defrost was conducted. The Expansion valve was not closing as the frost accumulated on the evaporators heat exchanger surface. It opened further to counterpoise the loss of performance by reducing the inlet temperature into the evaporator. The liquid injection valve was not oscillating.

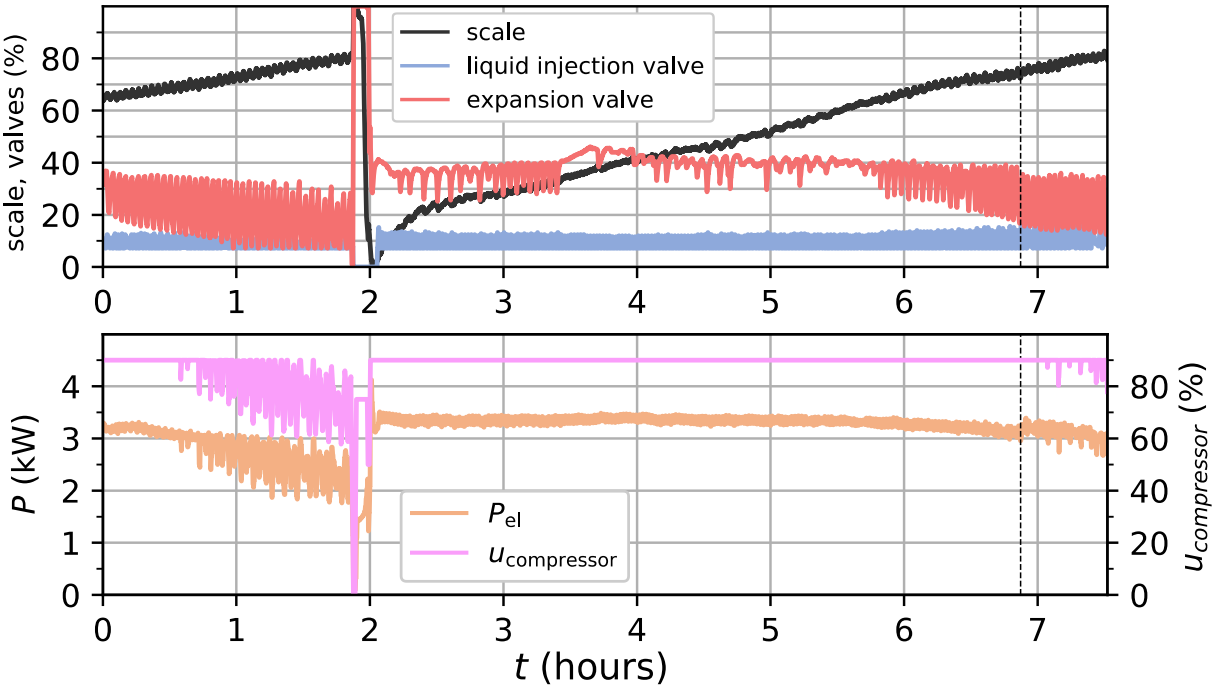

Figure 71: Scale, liquid injection valve expansion valve, electric power and compressor speed over the 2nd cycle of the *A2W37_I*.

In A2W37_I and A2W37_II, the PF did not differ between the cycles significantly (see Figure 72) and was solely attributed to the time when a defrost was conducted during the cycle.

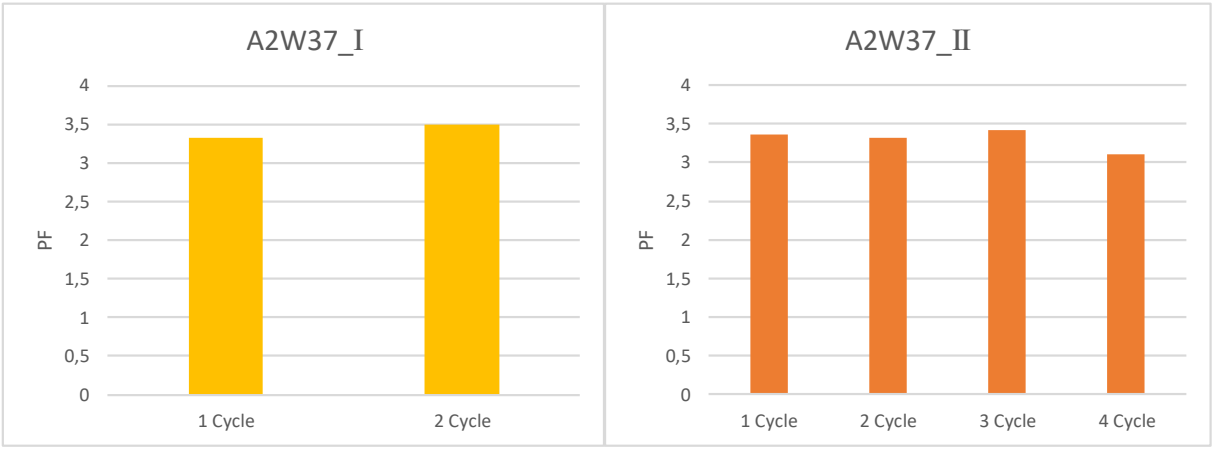

Figure 72 Results for PF of *A2W37_I* and *A2W37_II*. Left: *A2W37_I*. Right: *A2W37_II*.

This is highlighted when comparing the 1st and 2nd cycle in *A2W37_I* (see Figure 73). The 2nd cycle demonstrated a higher PF because during the charging of the RPW-HEX two defrosts were conducted whereas in the 1st cycle only one was initiated. The thermal power was decreasing with increasing frost by 3 kW. As a result, the overall performance in the 2nd cycle was better.

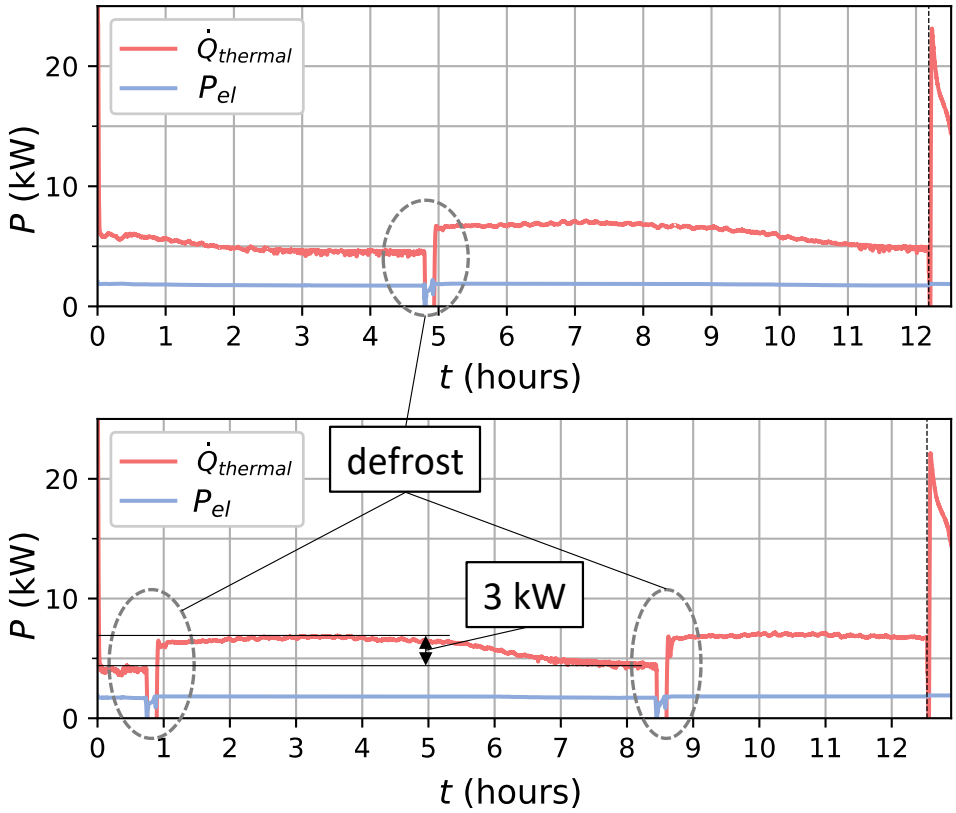

Figure 73: Comparison of the thermal and electric power in the 1st and 2nd cycle of *A2W37_I*. Top: 1st cycle. Bottom: 2nd cycle.

The decrease in power occurred after 4 hours of operation. In the work by Hochwallner Felix, 2019 the frosting phenomenon is investigated on the same heat exchangers surface at an ambient air temperature of 1.7 °C. In Figure 74 the frost accumulation between two fins is depicted. The air flow cross section of the evaporator was almost completely blocked by the accumulated frost after 4 hours. As a result, the evaporator was not able to heat the refrigerant sufficiently. The pressure on the suction side of the compressor dropped. Because the compressor was operated at a fixed speed, also the compressor outlet pressure declined which was already discussed in A-7W43_I and A-7W43_II. With declining pressure on the pressure side of the refrigerant cycle, the condensing temperature was lowered. Thus, the thermal power provided by the condenser was reduced. As a result, obstruction of the air flow by accumulating frost led to a distinct decrease in thermal power.

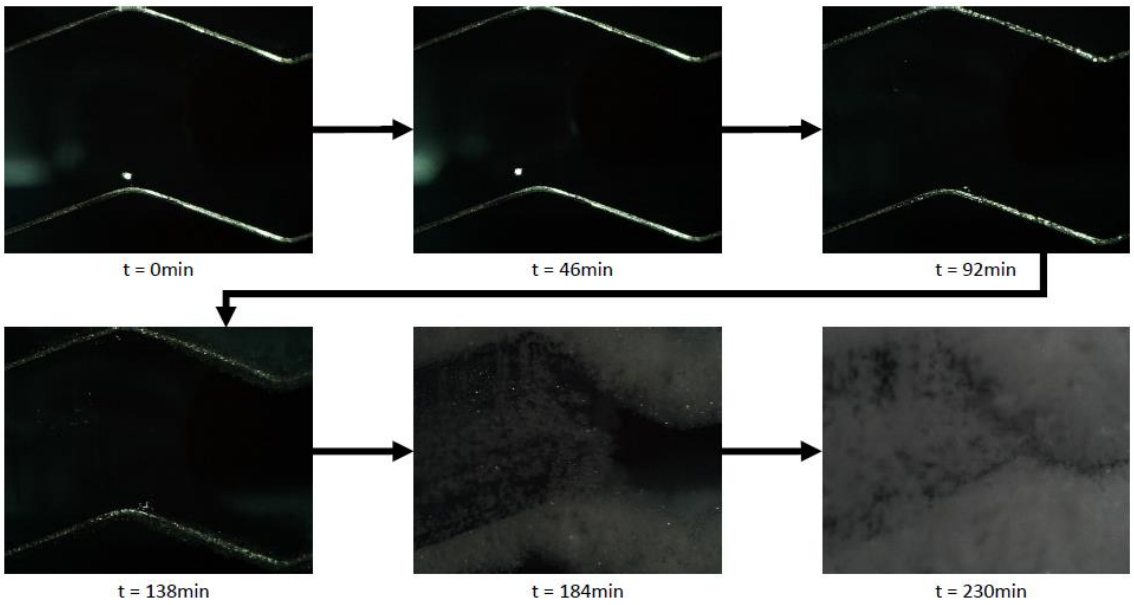

Figure 74: Frosting phenomena on the heat exchanger surface of the evaporator with an outside temperature of 1.7°C. (Hochwallner Felix, 2019)

Other than that, *A2W37_I* and *A2W37_II* behaved fairly similar. By discharging the RPW-HEX with a regulated system outlet temperature of 55 °C the discharge was prolonged and a higher amount of thermal energy for DHW production was provided (see Figure 75). The differences within each test series in thermal energy while discharging was due to different progress in frosting. If the defrost has been performed long before the discharge was conducted the HP had less thermal power which abbreviated the discharging time and lowered the amount of produced DHW.

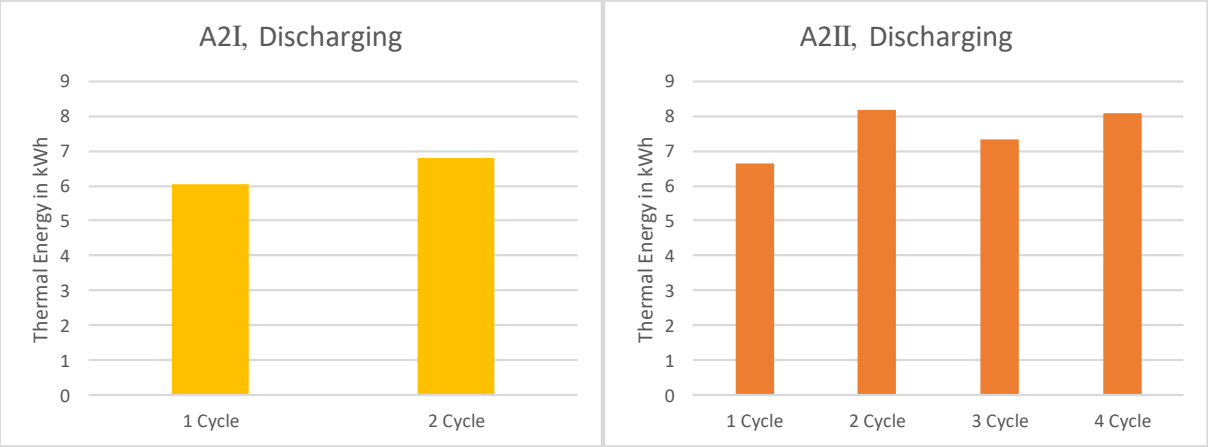

Figure 75: Comparison of the thermal energy yielded in the *A2W37_I* and *A2W37_II*. Left: *A2W37_I*. Right: *A2W37_II*.

In Figure 76 a comparison between the two discharge approaches is given. $E_{\mathrm{RPW_W}}$ displays the energy yielded by the RPW-HEX including the energy which is transferred from the refrigerant into the RPW-HEX. Because the discharge approach II was prolonged the HP contributes to more thermal energy resulting in a higher total output during the discharge.

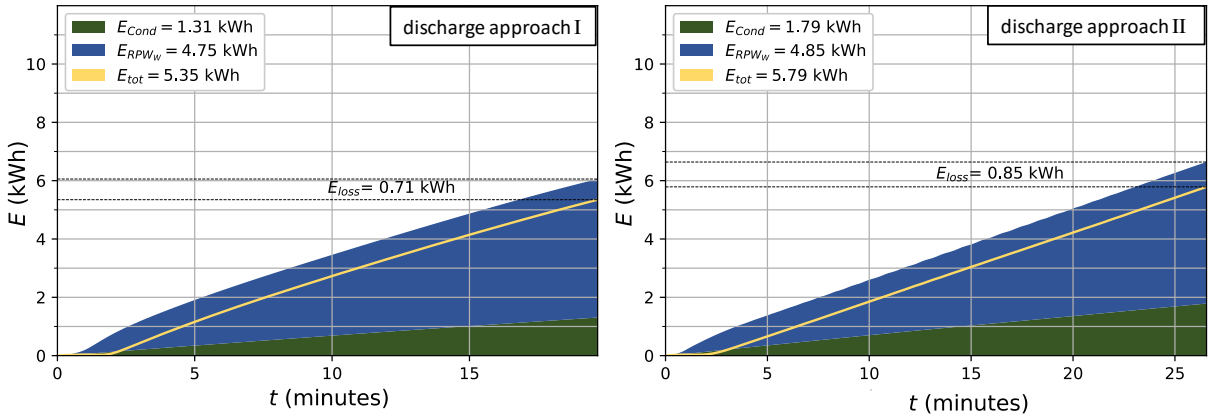

Figure 76: Comparison of the discharge process in *A2W37_I* and *A2W37_II*. Left: Discharge I. Right: Discharge II.

4.2.7 State of Charge (SoC)

One question that came up when implementing the RPW-HEX into the refrigerant cycle was how to determine the SoC. From the experiments with the *mini-LHS* it was deduced that the temperature sensors on the surface of the RPW-HEX delivered reliable data. The PCM temperature inside the RPW-HEX could be reflected with satisfying accuracy. However, when commercially building such a latent heat storage, surface temperature sensors are effortful, expensive and impractical. Therefore, another solution to determine the state of charge is necessary. One attempt was to use the pressure inside the PCM section of the RPW-HEX.

When set to zero at 20 °C, the pressure sensor PDTI-38 was not capable of measuring any changes in pressure, because the pressure quickly rose above 600 mbar. Therefore, the air was let out of the PCM section at a higher temperature to re-set the pressure inside the RPW-HEX PCM section to zero. This way the pressure difference throughout the whole discharging cycle could be measured. The total pressure that would occur if the RPW-HEX was heated up from 20 °C is unknown but changes in pressure could be measured as presented in Figure 77. Below the pressure, the derivative of the pressure and its mean value are shown. The data suggests that with the majority of the PCM has been solidified the pressure changed abruptly. This way a state of discharge could be determined by the sudden change in pressure.

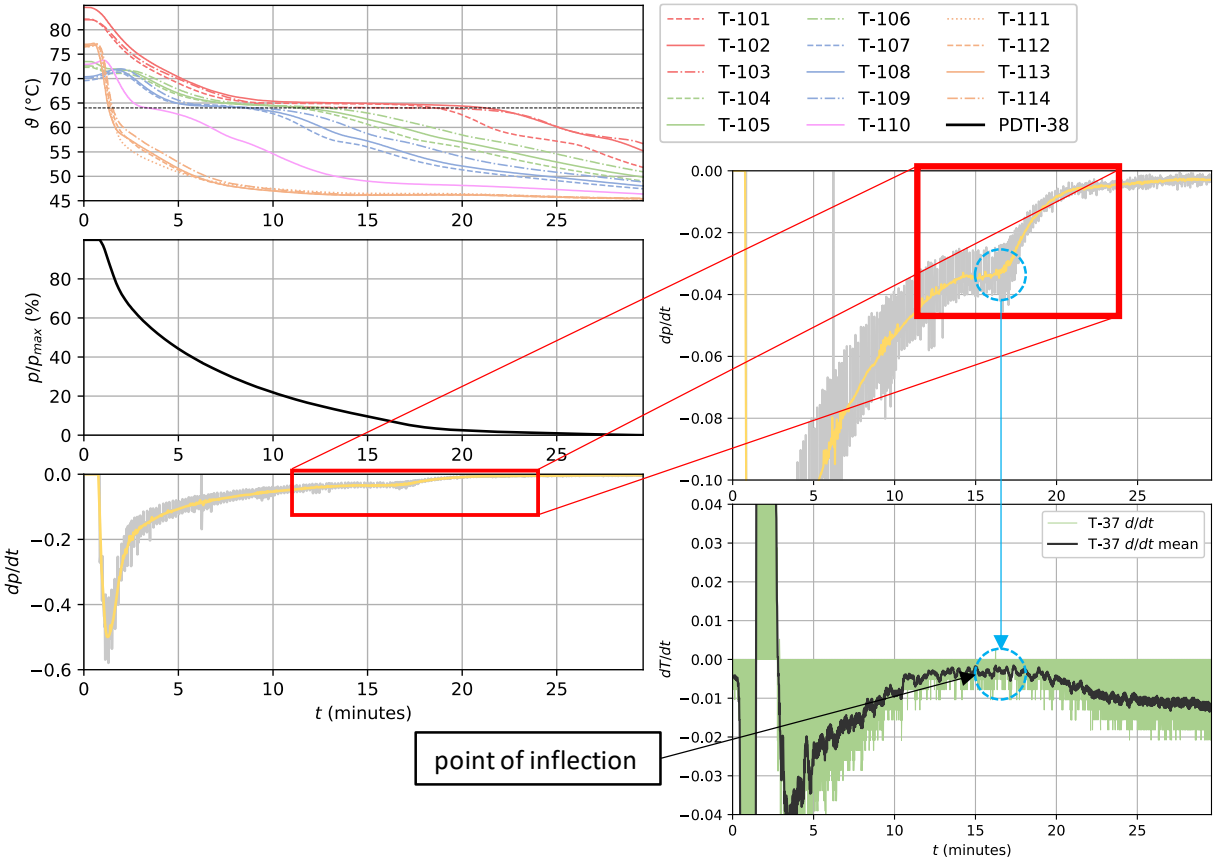

Figure 77: Measured data during discharging to determine the SoC. Left top: Temperatures on the RPW-HEX surface. Left middle: Pressure (PDTI-38) divided by the highest measured value. Left bottom: The grey curve represents the time dependent derivative of the pressure and the yellow line is a moving average over 10 values of this curve. Right top: Close up of the time dependent derivative between minutes 15 and 20. Right bottom: Time dependent derivative of the RPW-HEX water exit temperature.

On the right side of Figure 77, the change of the RPW-HEX exit water temperature is also plotted. It is visible that the time derivative of the water outlet temperature of the RPW-HEX had its point of inflection when the fast change in pressure occurred. The point of inflection indicates that most

of the thermal energy saved in the PCM was used and therefore the PCM had solidified to a large extent because the water temperature was starting to decline faster again.

Later the PDTI-38 was exchanged with a sensor that was capable of measuring pressures up to 10 bar. With this pressure sensor, difficulties were experienced as well. More than once the liquid PCM was pressed into the pressure sensors hose and the sensor itself (see Figure 78) where it solidified. This led to wrong measurement results. If the pressure of RT64 needs to be monitored it is advisable to make sure that the liquid PCM is not able to block the measurement hose. Please note that the liquid RT64 has a lower viscosity than water. Because of these problems, it was not possible to measure the pressure throughout a whole charging cycle. Therefore, only data for the discharging process exists.

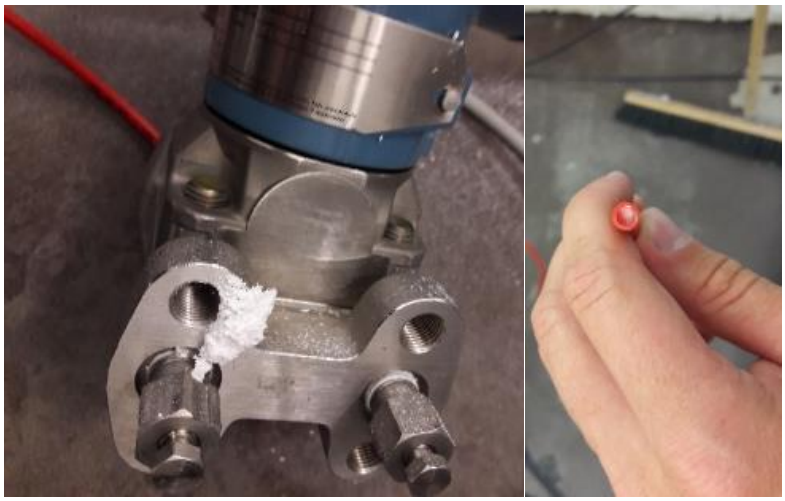

Figure 78: Left: Pressure sensor which was clogged by PCM. Right: Image of the PCM inside the pressure sensors hose.

In the future, more tests with correct measurements of the pressure inside the PCM section will clarify if the SoC can be determined through the pressure. It was observed that with complete solidification or melting, the pressure clearly changes in a short period of time. From this observation, it can be derived that the change in volume is the greatest during melting and solidification. RUBITHERM states that the change in volume of RT64 is 11% when the temperature is changed from 20 °C to 80 °C (Rubitherm, 2020) but it is unknown when the greatest change in volume occurs.

4.2.8 Different DC voltage

To see if the HP can be operated with DC and if there are any "side effects", a DC-test with different voltages was performed.

The results of these tests are shown in Figure 79. In order to investigate the impact of a change in voltage, when operating the HP with DC, the voltage was changed from 510 V to 680 V and to 595 V. Switching between the different voltages was smooth and did not interrupt the operation.

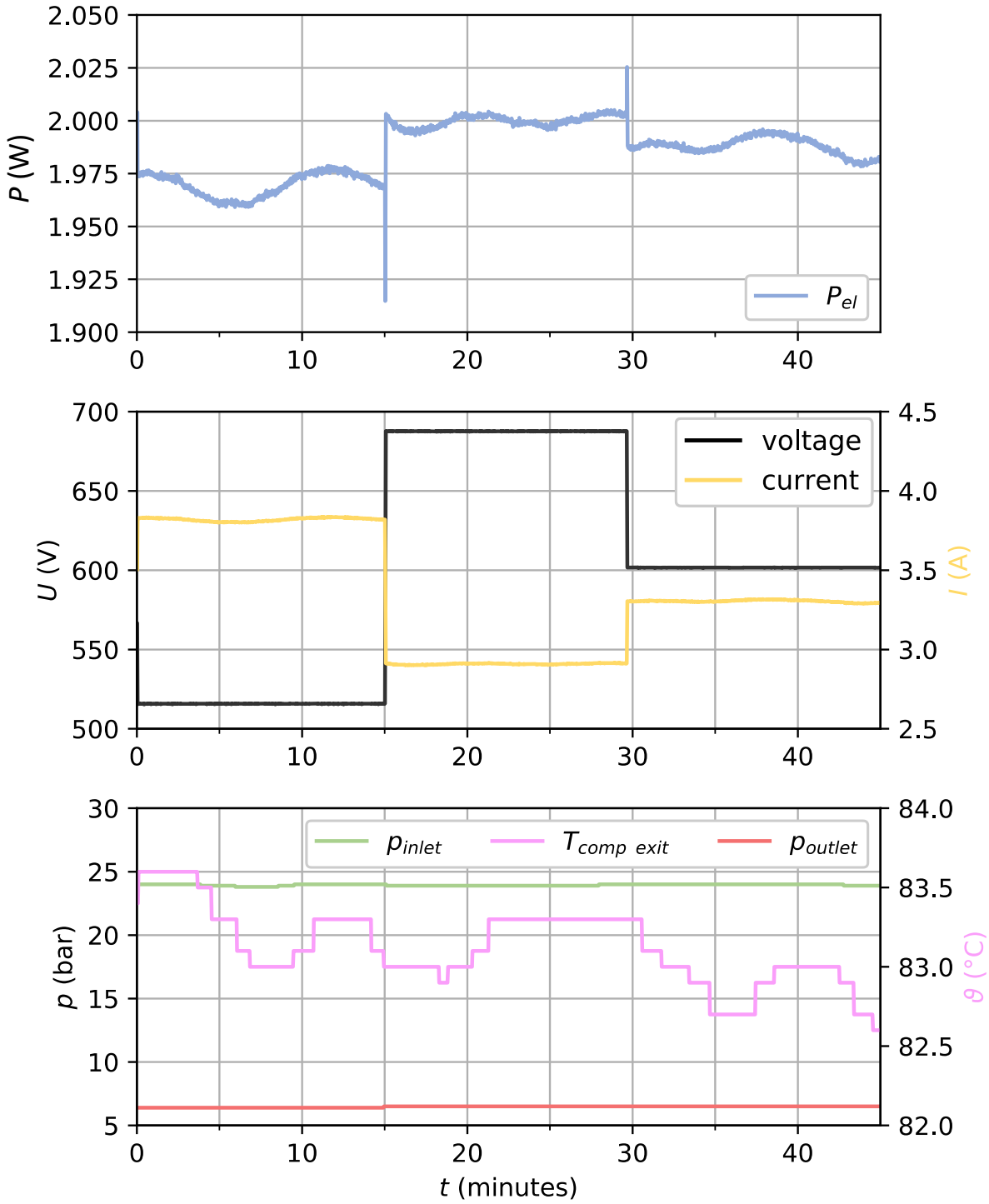

Figure 79: Results from testing the HP with DC. Top: Measured electric power P_{el}. Middle: Current I(t) and voltage U(t). Bottom: Compressor inlet and outlet pressure and compressor exit temperature TI-04.

In Figure 79 neither the compressor exit temperature nor the in- and outlet pressure of the compressor changed significantly when changing the voltage. The mechanical power consumption of the compressor was dependent on the HP operating conditions. From the experiments, one may conclude that during this test run the HP operation was constant based on the temperature and pressure measurements. But the change in voltage had, however, an impact on the electric power consumption. When switched from 510 V to 680 V, the electric power rose by 25 W. As soon as the voltage was turned down from 680 V to 595 V the electric power decreased as well. This led to the conclusion that it is most efficient to power the compression HP with low voltage if DC is used. In Table 11 the results of the DC-bus testing including the standard deviation are shown.

Table 11: Results of DC-testing.

test case	voltage (V)	current (A)	CPR	P_{el} (W)	$\dot{Q}_{Cond}$ (W)
DC-1	515.8 ± 0.09	3.8 ± 0.01	3.7 ± 0.01	1969.8 ± 5.64	7242.9 ± 94.05
DC-2	687.6 ± 0.12	2.9 ± 0.00	3.7 ± 0.01	1999.8 ± 2.72	7311.6 ± 56.43
DC-3	601.7 ± 0.06	3.3 ± 0.01	3.7 ± 0.01	1988.1 ± 4.18	7389.4 ± 68.53

4.2.9 Pressure drop of the water through the RPW-HEX

In Figure 80 the pressure drop of the water is plotted as a function of the water mass flow through the RPW-HEX. As we can see the pressure loss increased quadratically with the mass flow rate. Mass flow rates could be set from 380 to 2230 lh^{-1} in this experimental setup.

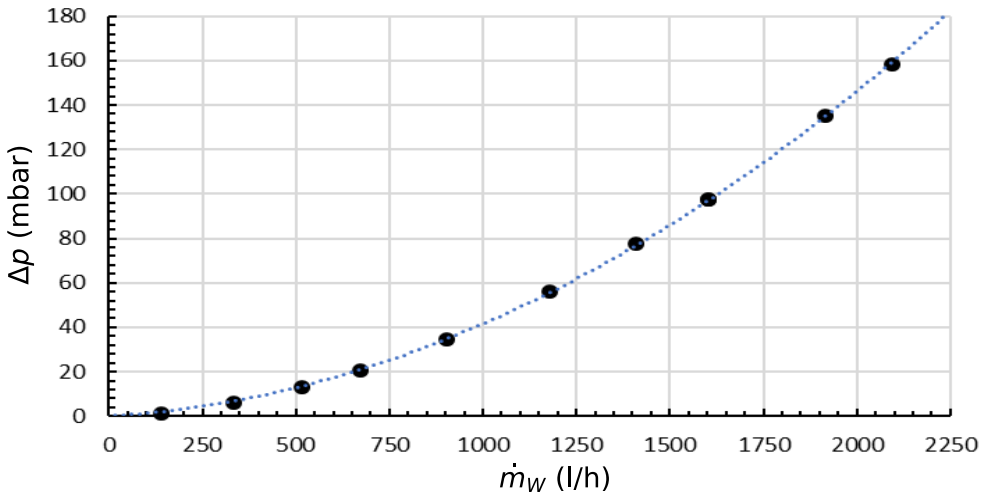

Figure 80: Pressure drop of the water as a function of the water mass flow through the water section of the RPW-HEX.

4.2.10 Refrigerant mass flow as a function of pressure loss through the RPW-HEX

Because the refrigerant mass flow could not be measured when the refrigerant was in a two-phase state, an attempt was made to establish a correlation between mass flow and pressure loss via the RPW-HEX on the refrigerant side. To achieve this, all measured data throughout every test was divided into pieces 7.5 minutes long. Whenever the refrigerant mass flow was measurable during those 7.5 minutes the mean pressure drop and the mean refrigerant mass flow were plotted as a dot in Figure 81. As we can see, in none of the measured data points the liquid injection valve was closed. Therefore, the refrigerant mass flow was slightly incorrect. In order to get clear results, more tests have to be carried out where the mass flow is correctly measured, and the liquid injection valve is closed.

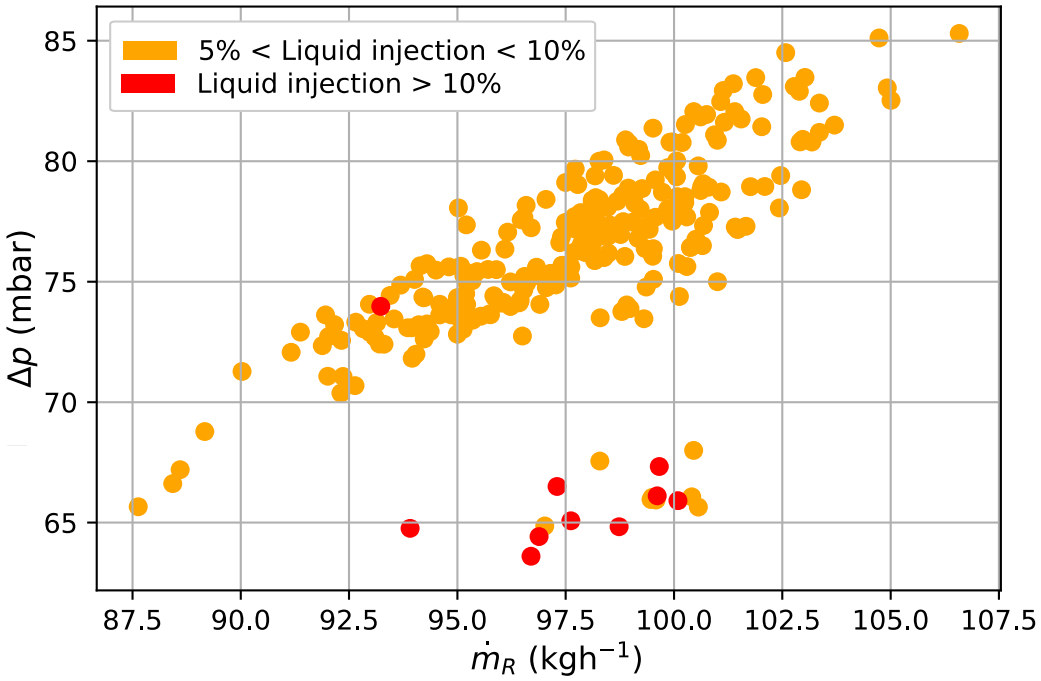

Figure 81: Pressure loss through the RPW-HEX as a function of the refrigerant mass flow. The measured data is insufficient to acquire a useful correlation between refrigerant mass flow and pressure loss.

5 Conclusion and Outlook

Technical details for a novel HP system were described and the experimental results discussed. In the novel system, a refrigerant/water/phase change material heat exchanger (RPW-HEX) was integrated into the refrigerant cycle using the hot compressor exit gas to store thermal energy for domestic hot water (DHW) production. A start up procedure was developed for the HP system and challenges, which the system faced with the implementation of a latent heat storage into the refrigerant cycle, were described. Tests to evaluate the performance of the RPW-HEX were performed and the behavior of the system was examined during dynamic operation. During the dynamic operation, the system operated continuously with a fixed compressor speed while charging and discharging the RPW-HEX. Design decisions and changes for a new version of the RPW-HEX were created that should lead to a better heat distribution and heat transfer within the RPW-HEX. The HP was also tested with DC voltage. Different methods to determine the state of charge of the RPW-HEX were discussed. The system was tested under two critical outside temperatures (-7 °C and 2 °C) where frost accumulated on the evaporators heat exchanger surface rapidly. In addition, two different discharge approaches of the RPW-HEX were validated.

To develop a further understanding of the behavior of the PCM within the RPW-HEX, stand-alone mini latent heat storages (LHS) were built. With these *mini-LHS,* the phase change behavior of the PCM RT64 was investigated. The effect of subcooling and the influence of the previous state of phase on the current state of phase was observed. Implementation of a fin geometry into the PCM enhanced the heat transfer tremendously and led to completely different temperature distributions within the PCM.

The research questions were answered as follows:

Stand-alone mini-LHS:

1. How is the phase change behavior altered when implementing fins into the PCM?

The data strongly indicates that with the implementation of metal fins into the PCM in addition to an enhancement in thermal conductivity the phase change was inhibited to some extent. With the same temperature difference, the phase front reached different positions even though the previous state was the same. In the cooling tests, it is assumed that the supercooling effect is the driving force for this phenomenon. But the difference was especially big in the heating tests. The PCM reached completely different temperatures in the *empty-sample* and the *fin-sample*. The implementation of the aluminum structure enhanced the heat transfer and at the same time induced a linear temperature profile within the liquid phase of the PCM. This led to a completely different temperature distribution and therefore a different position of the phase front.

2. How does the heat transfer change with progressing solidification?

With equation (15) a decrease in heat flux with the rise of the solid phase position was assumed. Since the complete heat transfer between the hot and the cold fin was not measured, and the assumption of $\dot{q}_1 = \dot{q}_2 = \dot{q}$ was proved wrong, it was impossible to say to what extent the heat flux depended on the position of the solid phase front. In one experiment, however, the heat flux sensor was positioned in the solid phase. In this test, the measured results correlated with the calculated results from equation (15). For more meaningful results about the dependency of the heat flux to the solid phase thickness, more tests would have to be carried out, measuring the heat flux on both fins simultaneously.

3. Is the measurement of a heat flux sensor dependent on the state of the PCM-phase?

The measurement with a heat flux sensor delivered different results, depending on the location of the sensor. With a heat flux sensor mounted onto the cold fin, a sudden rise in measured heat flux could indicate that the majority of the PCM has changed phase. In addition, the numerical approach to calculate the heat flux as a function of the solid phase position (x), proved to be valid for the heat flux through the solid PCM. Measurements of a heat flux sensor deliver different results depending on if the sensor was placed in the liquid region of the PCM or in a solid region. To determine the SoC a heat flux sensor is unsuitable because the measured heat flux is dependent on the position of the sensor. In addition, it is very unpractical to install a sensor inside the RPW-HEX.

4. Can an optimal fin geometry be derived from the *mini-LHS* measurements for the RPW-HEX?

The experiments with the *mini-LHS* showed that metal fins can improve heat conductivity through the PCM tremendously. By implementing fins, with a 10 mm width into the *mini-LHS*, melting and solidification time was reduced by a factor of 25. With an even smaller fin size, this time can be reduced even more, but at the same time, the LHS loses energy density, as the aluminum can only store sensible heat. Compared to aluminum the PCM can be regarded as thermal insulation. For this reason, it is important when building a thermal storage with RT64, to ensure a good heat distribution inside the PCM. Otherwise, the charge and discharge rates are strongly limited by the PCM. More tests with different fin widths will have to be performed to acquire the optimal fin width for the RPW-HEX. The PCM channels in the RPW-HEX were 7 mm thick and therefore 3 mm smaller than the fins in the *fin-sample*. Therefore, also the heat transfer rate was greater inside the RPW-HEX which led to the subcooling effect that was observed in the RPW-HEX experiments. The goal is to reduce the amount of aluminum inside the RPW-HEX but at the same time ensure satisfying heat transfer rates. Because naturally with a lower amount of aluminum the RPW-HEX would be more economical and at the same time gain a higher energy density. To achieve this, more tests have to be performed and validated.

5. What should be considered when using RT64 in a large storage device? How can the results of the *mini-LHS* be translated to a larger system? Does the PCM RT64 have any properties that can either enhance or limit its use in a latent heat storage for DHW production?

The PCM RT64 proved to be suitable as a PCM for a thermal storage application for DHW production. The effect of subcooling is noticeable but does not interfere with operation as the solidification temperature is only displaced by a few degrees Celsius. This, however, has no impact on the provided amount of DHW, because the desired system outlet temperature was chosen to be 55 °C (discharge approach II). The second solidification enthalpy peak was observed to be between 58 °C and 60 °C, depending on the cooling rate. Therefore, the desired outlet temperature should be below 58 °C, otherwise RT64 would not be the ideal PCM since part of the phase change enthalpy could not be used. The *mini-LHS* tests also showed that the state of the PCM was not only dependent on the temperature but also on its previous state. As the RPW-HEX preferably went through a complete phase change during operation, the different melting and solidification behavior caused by this effect, had no significant impact on the operation.

Integrated RPW-HEX:

1. Is the implementation and operation of the latent heat storage in an HP cycle possible from a technical point of view?

The experimental setup proved that an implementation of an RPW-HEX into a refrigerant cycle is unproblematic from a technical point of view. However, the refrigerant cycle and its automatic control have to be adapted to make an operation possible.

2. What challenges arise when integrating a heat storage directly into a refrigerant cycle and how can they be overcome?

When testing the combination of an HP with the RPW-HEX, a few problems occurred which have to be considered when setting up an HP-system like this.

a) For the HP, R-32 was used as a refrigerant because it has a zero ODP and tends to reach higher temperatures when being compressed. However, the GWP of R-32 is still 675 times higher than the one of CO_2. Therefore, as little refrigerant as possible is used which prevents the use of a header in the refrigerant circuit. A header would ensure an even flow of refrigerant. To prevent condensation inside the RPW-HEX it is never discharged to temperatures below the condensation temperature of the refrigerant. Condensation of refrigerant inside the RPW-HEX would "dry out" the refrigerant cycle.

b) Lubrication oil for the compressor circulated in the normal HP circuit without RPW-HEX. This was not possible anymore with the implementation of the RPW-HEX because the spatial volume of the circuit was enlarged, letting the compressor run dry. An oil separator had to be installed for this system. In addition, a different positioning (vertical above the HP) of the RPW-HEX could also help to solve this problem.

c) The mass flow measurement generates a pressure loss that should not be disregarded, which is why it was installed in this design downstream of the condenser. If it were installed upstream of the condenser, the condensation temperature in the condenser would drop. The problem with this installation is that the mass flow sensor is bypassed when the liquid injection valve is open. In addition, whenever the refrigerant is in a two-phased state after the condenser, the mass flow could not be measured. The problem could be solved by finding out the dependency of pressure loss and the mass flow of the refrigerant in several operating points. For this, several tests would have to be carried out in which the liquid injection valve is closed, and the refrigerant is liquid before entering the expansion valve.

d) The heat transfer from the refrigerant to the PCM inside the RPW-HEX could be increased. The exit temperature of the hot gas is always around 10 °C higher than the temperatures measured on the RPW-HEX surface. With a different design (e.g. smaller refrigerant channels, redirection of the refrigerant inside the RPW-HEX) this heat transfer can be increased. A second version of the RPW-HEX is currently under construction where these design decisions are being taken into account.

e) When measuring the pressure of the PCM-section arrangements have to be made, to prevent the liquid PCM from blocking the pressure measurement hose. Measuring the pressure inside the PCM section can give information about the SoC.

f) Operation with direct current does not pose any problems, however with an increase in supply voltage the electric consumption ascends.

3. Do surface temperature sensors on the RPW-HEX deliver reliable results?

The mounted surface temperature sensors on the RPW-HEX correlate with the results of the *fin-sample*. The temperature curves inside the PCM as well as on the surface of the RPW-HEX display the same profile when being heated or cooled. This means that the surface temperature sensors on the RPW-HEX reflected the actual temperature of the PCM to a satisfying degree.

4. How can the state of charge (SoC) of the RPW-HEX be determined?

There are two possibilities to determine the SoC of the RPW-HEX. The first one is to measure the temperature inside the PCM section of the RPW-HEX. Inserting temperature sensors into the RPW-HEX has to be considered in the production already, as it is not possible to subsequently boreholes into the RPW-HEX. The temperature can also be derived through the surface, which does not provide the same accuracy as a sensor inside the PCM but proved to be sufficient. However, with the temperature of the PCM exceeding 64 °C, the RPW-HEX can be considered as fully charged. The second possibility is to measure the pressure inside the PCM section of the RPW-HEX. In this work, a correlation between the change in pressure and the state of discharge was observed. Because of faulty pressure measurements, the SoC could not be deduced through the pressure. However, this method is promising as only one sensor is needed instead of many temperature sensors. With the validation of more tests, it is very likely that a meaningful correlation between the SoC and the pressure inside the PCM section of the RPW-HEX is discovered. A detailed analysis of the temperature dependent change in volume of the PCM would facilitate this proposition further.

5. Is the system capable of providing DHW under normal operating conditions?

The system proved to provide around 8 kWh of DHW each discharge. According to EN16147 (2017), the average DHW consumption of an apartment is 5.845 kWh per day. With up to 3 discharges per day under the operating settings described, the system is able to produce enough DHW for up to 4 apartments. Note that this strongly depends on the return water temperature. For these experiments, the return water temperature has been set to 31 °C and 34 °C. Emhofer et al., 2020 states that the annual energy savings are around 620 kWh_{el}/year and the minimum cost savings are 137 EUR/year when implementing an RPW-HEX with a storage capacity of 5 kWh. The lowest payback time was calculated with 12.4 years.

6. What factors have the biggest influence on the performance of the overall system?

As already mentioned multiple times, the largest impact on the performance of the overall system was the frosting phenomena and the resulting loss of performance. Especially when the defrost could not be properly initiated. Thus, the ambient temperature together with the air humidity can be derived as the largest influencing factor. The data suggests that the defrost should be conducted after 4 hours when operating at outside air temperatures around 2 °C. After 4 hours the air flow through the evaporators heat exchanger is blocked. Thus, the thermal power diminishes.

A second point is, powering the HP with DC at low voltage reduces the electric consumption while at the same time delivering the same thermal power.

7. Is the performance of the system enhanced by implementing the RPW-HEX?

Benchmark tests were conducted to validate the performance of the HP under various conditions. These conditions included heating/cooling and DHW generation at outside temperatures ranging from -10°C to 35°C.

At air temperatures around and below 0°C before each test a defrost was conducted to ensure that the test is not influenced by accumulated frost on the outside heat exchangers surface. Each benchmark test lasted 90 minutes. The measured data was used to calculate a COP:

$$COP = \frac{\bar{\dot{Q}}_{thermal}}{P_{el}}$$

With $\bar{\dot{Q}}_{thermal}$ being the mean thermal power provided by the condenser and P_{el} the average electric power consumption of compressor, evaporator fan and water pump combined. In Figure 82 the respective COP for each benchmark test is visualized. For all these tests the compressor exit temperature was limited to 115°C.

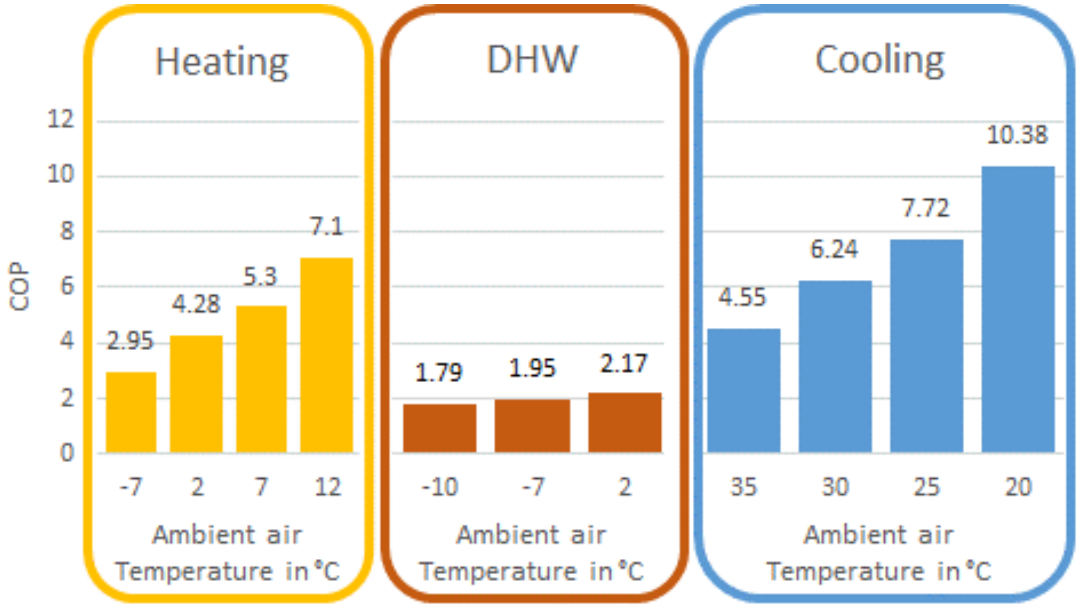

Figure 82: COP of every benchmark test that was conducted at the respective ambient air temperature.

The experimental setup with the integrated RPW-HEX cannot be compared to its this reference system because of mainly four reasons:

- The reference system was tested under conditions that excluded the frosting phenomena.
- DHW was generated at a temperature of 60°C instead of 55°C.
- The automatic control of the HP was changed and adapted throughout the tests.
- The compressor exit temperature was limited at 115 °C in the benchmark tests and was later reduced to 103 °C for the tests where the RPW-HEX was included.

Especially the frosting and at that time insufficient defrost process had such a significant impact on the performance of the system that it cannot be compared to a system where frosting is neglected.

The rise in efficiency by the implementation of the RPW-HEX has also been addressed in Hochwallner Felix, 2019 where this system was simulated with and without thermal storage. The results of the simulations revealed an overall efficiency enhancement of 5 to 10%. However, in reality, the heat transfer rate between the refrigerant and the RPW-HEX was lower than expected. Additionally, frosting resulted in a part-time operation of the HP with a thermal power-loss of up to 3 kW. Thus, the system was not able to live up to the expected results from the simulations. Note that this was a test prototype. Its purpose solemnly has been to demonstrate that an implementation of the RPW-HEX is possible and that the system can be operated smoothly. Tests, where frosting would not occur, were not carried in the course of this study.

The system proved to work reliably and switching between heating and DHW generation was smooth. The HP operation was uninterrupted throughout the dynamic operation. This underlines the ability of the system to shift thermal loads and generate high temperature heat while operating the HP at high efficiency.

In the future, a new version of the RPW-HEX will be integrated into the HP cycle and tested also under climatic conditions where frosting would not occur. In addition, cooling tests will be performed as well. Design decisions are going to be considered. To get a further understanding of the temperature distribution inside the PCM section of the RPW-HEX, the second version will be equipped with rod temperature sensors reaching into the PCM. The results will be used to optimize the experimental setup for a field test in France where this concept of the project HYBUILD is being tested in a real building.

Furthermore, investigating the thermodynamic properties of the PCM RT64 would make it possible to build mathematical models to calculate heat transfer rates and, in a further aspect, the melting and solidification times. More tests with different fin geometries will help to find the optimal fin geometry and therefore maximize the latent heat capacity but at the same time ensuring sufficient heat transfer rates.

5.1 Acknowledgment

Parts of this work have received funding from the European Union's Horizon 2020 research and innovation program under grant agreement No 768824 (HYBUILD).

6 List of figures

7 List of tables

8 References

Air-water heat exchanger [WWW Document], 2020. URL https://www.thomasnet.com/articles/process-equipment/understanding-heat-exchangers/ (accessed 2.4.20).

Bianco, V., Scarpa, F., Tagliafico, L.A., 2017. Estimation of primary energy savings by using heat pumps for heating purposes in the residential sector. Applied Thermal Engineering 114, 938–947. https://doi.org/10.1016/j.applthermaleng.2016.12.058

Christodoulides, P., Aresti, L., Florides, G., 2019. Air-conditioning of a typical house in moderate climates with Ground Source Heat Pumps and cost comparison with Air Source Heat Pumps. Applied Thermal Engineering 158, 113772. https://doi.org/10.1016/j.applthermaleng.2019.113772

Chung, Y., Yoo, J.W., Kim, G.T., Kim, M.S., 2019. Prediction of the frost growth and performance change of air source heat pump system under various frosting conditions. Applied Thermal Engineering 147, 410–420. https://doi.org/10.1016/j.applthermaleng.2018.10.085

Elias, C.N., Stathopoulos, V.N., 2019. A comprehensive review of recent advances in materials aspects of phase change materials in thermal energy storage. Energy Procedia 161, 385–394. https://doi.org/10.1016/j.egypro.2019.02.101

Emhofer, J., Marx, K., Barz, T., Hochwallner, F., Zsembinszki, G., Strehlow, A., Nitsch, B., Pink, W., 2020. Techno-economic analysis of a heat pump cycle including a three-media refrigerant/phase change material/water heat exchanger in the hot superheated section for efficient domestic hot water generation 12.

European Commission, 2020. THE ENERGY PERFORMANCE OF BUILDINGS DIRECTIVE [WWW Document]. Factsheet: Energy Performance in Buildings Directive. URL https://ec.europa.eu/energy/sites/ener/files/documents/buildings_performance_factsheet.pdf (accessed 1.4.20).

Farid, M.M., Khudhair, A.M., Razack, S.A.K., Al-Hallaj, S., 2004. A review on phase change energy storage: materials and applications. Energy Conversion and Management 45, 1597–1615. https://doi.org/10.1016/j.enconman.2003.09.015

Fawcett, T., 2011. The future role of heat pumps in the domestic sector 12.

Ferrari, S., 2007. Building envelope and heat capacity: re-discovering the thermal mass for winter energy saving 6.

Frequenzy converter [WWW Document], 2020. URL http://www.frequencyinverter.org/frequency-converter-basics.html (accessed 1.4.20).

Furbo, S., 2015. Using water for heat storage in thermal energy storage (TES) systems, in: Advances in Thermal Energy Storage Systems. Elsevier, pp. 31–47. https://doi.org/10.1533/9781782420965.1.31

Guo, K., Zhang, N., Smith, R., 2015. Optimisation of fin selection and thermal design of counter-current plate-fin heat exchangers. Applied Thermal Engineering 78, 491–499. https://doi.org/10.1016/j.applthermaleng.2014.11.071

Hirmiz, R., Teamah, H.M., Lightstone, M.F., Cotton, J.S., 2019. Performance of heat pump integrated phase change material thermal storage for electric load shifting in building demand side management. Energy and Buildings 190, 103–118. https://doi.org/10.1016/j.enbuild.2019.02.026

Hochwallner Felix, 2019. Experimental and numerical analysis of a latent storage integrated in a heat pump cycle.

HYBUILD deliverable 3.2 [WWW Document], 2020. URL http://www.hybuild.eu/ (accessed 2.17.20).

International Energy Agency (Ed.), 2013. Transition to sustainable buildings: strategies and opportunities to 2050. IEA Publ, Paris.

Jarre, M., Noussan, M., Simonetti, M., 2018. Primary energy consumption of heat pumps in high renewable share electricity mixes. Energy Conversion and Management 171, 1339–1351. https://doi.org/10.1016/j.enconman.2018.06.067

Jevnikar, S., Siddiqui, K., 2019. Investigation of the influence of heat source orientation on the transient flow behavior during PCM melting using particle image velocimetry. Journal of Energy Storage 25, 100825. https://doi.org/10.1016/j.est.2019.100825

Jin, X., Hu, H., Shi, X., Zhang, X., 2015. Energy asymmetry in melting and solidifying processes of PCM. Energy Conversion and Management 106, 608–614. https://doi.org/10.1016/j.enconman.2015.10.001

Kim, B., Hun Lee, S., Lee, D., Kim, Y., 2020. Performance comparison of heat pumps using low global warming potential refrigerants with optimized heat exchanger designs. Applied Thermal Engineering 114990. https://doi.org/10.1016/j.applthermaleng.2020.114990

Le, K.X., Huang, M.J., Shah, N., Wilson, C., Artain, P.M., Byrne, R., Hewitt, N.J., 2019. High Temperature Air Source Heat Pump Coupled with Thermal Energy Storage: Comparative Performances and Retrofit Analysis. Energy Procedia 158, 3878–3885. https://doi.org/10.1016/j.egypro.2019.01.857

Linde Gases AG, 2020. Refrigerants Environmental Data. Ozone Depletion and Global Warming Potential. [WWW Document]. URL http://www.linde-gas.com/en/legacy/attachment?files=tcm:Ps17-111483,tcm:s17-111483,tcm:17-111483 (accessed 2.4.20).

Lizana, J., Chacartegui, R., Barrios-Padura, A., Valverde, J.M., 2017. Advances in thermal energy storage materials and their applications towards zero energy buildings: A critical review. Applied Energy 203, 219–239. https://doi.org/10.1016/j.apenergy.2017.06.008

Mehling, H., Barreneche, C., Solé, A., Cabeza, L.F., 2017. The connection between the heat storage capability of PCM as a material property and their performance in real scale applications. Journal of Energy Storage 13, 35–39. https://doi.org/10.1016/j.est.2017.06.007

Minglu, Q., Liang, X., Deng, S., Yiqiang, J., 2010. Improved indoor thermal comfort during defrost with a novel reverse-cycle defrosting method for air source heat pumps. Building and Environment 45, 2354–2361. https://doi.org/10.1016/j.buildenv.2010.04.006

Mohanraj, M., Muraleedharan, C., Jayaraj, S., 2011. A review on recent developments in new refrigerant mixtures for vapour compression-based refrigeration, air-conditioning and heat pump units. Int. J. Energy Res. 35, 647–669. https://doi.org/10.1002/er.1736

Mollova, A., Androsch, R., Mileva, D., Schick, C., Benhamida, A., 2013. Effect of Supercooling on Crystallization of Polyamide 11. Macromolecules 46, 828–835. https://doi.org/10.1021/ma302238r

Palm, B., 2008. Hydrocarbons as refrigerants in small heat pump and refrigeration systems – A review. International Journal of Refrigeration 31, 552–563. https://doi.org/10.1016/j.ijrefrig.2007.11.016

Picón-Núñez, M., Robles, J.L.L., 2005. Flow Passage Arrangement and Surface Selection in Multistream Plate-Fin Heat Exchangers. Heat Transfer Engineering 26, 5–14. https://doi.org/10.1080/01457630500205547

Plate heat exchanger [WWW Document], 2020. URL https://www.framatome.com/FR/businessnews-750/areva-np-et-tranter-inc-associent-leur-expertise-pour-le-remplacement-des-echangeurs-thermiques-dans-les-installations-nucleaires.html

Rady, M., 2009. Study of phase changing characteristics of granular composites using differential scanning calorimetry. Energy Conversion and Management 50, 1210–1217. https://doi.org/10.1016/j.enconman.2009.01.030

Rathgeber, C., Schmit, H., Miró, L., Cabeza, L.F., Gutierrez, A., Ushak, S.N., Hiebler, S., 2018. Enthalpy-temperature plots to compare calorimetric measurements of phase change materials at different sample scales. Journal of Energy Storage 15, 32–38. https://doi.org/10.1016/j.est.2017.11.002

Rubitherm, 2020. Technical datasheet RT64HC [WWW Document]. URL https://www.rubitherm.eu/media/products/datasheets/Techdata_-RT64HC_EN_06082018.PDF (accessed 1.4.20).

Shen, J., Qian, Z., Xing, Z., Yu, Y., Ge, M., 2019. A review of the defrosting methods of air source heat pumps using heat exchanger with phase change material. Energy Procedia 160, 491–498. https://doi.org/10.1016/j.egypro.2019.02.197

Shokouhmand, H., Kamkari, B., 2013. Experimental investigation on melting heat transfer characteristics of lauric acid in a rectangular thermal storage unit. Experimental Thermal and Fluid Science 50, 201–212. https://doi.org/10.1016/j.expthermflusci.2013.06.010

Sparrow, E.M., Schmidt, R.R., Ramsey, J.W., 1978. Experiments on the Role of Natural Convection in the Melting of Solids. Journal of Heat Transfer 100, 11–16. https://doi.org/10.1115/1.3450484

Stropnik, R., Koželj, R., Zavrl, E., Stritih, U., 2019. Improved thermal energy storage for nearly zero energy buildings with PCM integration. Solar Energy 190, 420–426. https://doi.org/10.1016/j.solener.2019.08.041

Sun, X., Chu, Y., Mo, Y., Fan, S., Liao, S., 2018. Experimental investigations on the heat transfer of melting phase change material (PCM). Energy Procedia 152, 186–191. https://doi.org/10.1016/j.egypro.2018.09.079

Sun, X., Zhang, Q., Medina, M.A., Lee, K.O., 2016. Experimental observations on the heat transfer enhancement caused by natural convection during melting of solid–liquid phase change materials (PCMs). Applied Energy 162, 1453–1461. https://doi.org/10.1016/j.apenergy.2015.03.078

Tang, L., Du, X., Pan, J., Sundén, B., 2019. Air inlet angle influence on the air-side heat transfer and flow friction characteristics of a finned oval tube heat exchanger. International Journal of Heat and Mass Transfer 145, 118702. https://doi.org/10.1016/j.ijheatmasstransfer.2019.118702

Uzan, A.Y., Kozak, Y., Korin, Y., Harary, I., Mehling, H., Ziskind, G., 2017. A novel multi-dimensional model for solidification process with supercooling. International Journal of Heat and Mass Transfer 106, 91–102. https://doi.org/10.1016/j.ijheatmasstransfer.2016.10.046

Verein Deutscher Ingenieure (Ed.), 2010. VDI heat atlas, 2. ed. ed, Springer reference. Springer, Heidelberg.

Zahir, Md.H., Mohamed, S.A., Saidur, R., Al-Sulaiman, F.A., 2019. Supercooling of phase-change materials and the techniques used to mitigate the phenomenon. Applied Energy 240, 793–817. https://doi.org/10.1016/j.apenergy.2019.02.045

9 Appendix A

The total water mass flow which will pass the condenser:

$$\dot{m}_W = FTI_{32} \tag{25}$$

The water mass flow which flows through the RPW-HEX is the difference between the total water mass flow and the mass flow which bypasses the RPW-HEX:

$$\dot{m}_{\mathrm{RPW_W}} = FTI_{32} - FTI_{21} \tag{26}$$

The refrigerant mass flow is measured in front of the expansion valve. When the refrigerant is two-phased the mass flow sensor is not capable of measuring the mass flow:

$$\dot{m}_R = FTI_8 \tag{27}$$

With the water temperatures at the inlet and outlet of the RPW-HEX, the Power delivered by it is derived from:

$$\dot{Q}_{\mathrm{RPW_W}} = (T_{26} - T_{34}) * \dot{m}_{\mathrm{RPW_W}} * \bar{c}_{p_{\mathrm{W}}}(T_{26}, T_{34}) \tag{28}$$

By integrating the Power $\dot{Q}_{RPW_W}$ over the time when water passes through the RPW-HEX we get the Energy that the RPW-HEX delivers to the water:

$$E_{\mathrm{RPW_W}} = \int \dot{Q}_{\mathrm{RPW_W}} * dt \tag{29}$$

With the refrigerant temperatures at the inlet and outlet of the RPW-HEX, the Power with which the RPW-HEX is being charged is derived from:

$$\dot{Q}_{\mathrm{RPW_R}} = (T_{06} - T_{04}) * \dot{m}_{\mathrm{R}} * \bar{c}_{p_{\mathrm{R}}}(T_{06}, T_{04}) \tag{30}$$

Through integration over time, the energy transferred from the HP to the RPW-HEX in a certain timeframe is derived:

$$E_{\mathrm{RPW_R}} = \int \dot{Q}_{\mathrm{RPW_R}} * dt \tag{31}$$

By knowing how much energy is transferred into the RPW-HEX (E_{RPW_R}) and how much is drawn from it at the same time (E_{RPW_W}), the energy which was stored can be calculated with:

$$E_{RPW} = \int_{t_1}^{t_2} \dot{Q}_{\mathrm{RPW_W}} * dt - \int_{t_1}^{t_2} \dot{Q}_{\mathrm{RPW_R}} * dt = E_{\mathrm{RPW_W}} - E_{\mathrm{RPW_R}} \tag{32}$$

The condenser power is derived from the total water mass flow and the temperatures at the inlet and outlet. However, depending on the operating mode of the system, two different temperature sensors are being used to measure the water outlet temperature of the condenser. During charging T_{29} is being used while during discharging T_{23} is used as the outlet temperature:

$$\dot{Q}_{\mathrm{Cond_{charging}}} = (T_{29} - T_{17}) * \dot{m}_{\mathrm{W}} * \bar{c}_{p_{\mathrm{W}}}(T_{29}, T_{17}) \tag{33}$$

$$\dot{Q}_{\mathrm{Cond_{discharging}}} = (T_{23} - T_{17}) * \dot{m}_{\mathrm{W}} * \bar{c}_{p_{\mathrm{W}}}(T_{23}, T_{17}) \tag{34}$$

The energy of the condenser is calculated by integrating each condenser power over the respective time window.

$$E_{\text{Cond}} = \int_{t_1}^{t_2} \dot{Q}_{\text{Cond}_{\text{charging}}} * dt + \int_{t_2}^{t_3} \dot{Q}_{\text{Cond}_{\text{discharging}}} * dt \quad \textbf{(35)}$$

The total thermal power of the system is derived from the total water mass flow, the water temperature at the condenser inlet and the water temperature after the mixing point of the RPW-HEX and the Bypass:

$$\dot{Q}_{\text{tot}} = (T_{37} - T_{17}) * \dot{m}_W * \bar{c}_{p_{\text{W}}}(T_{37}, T_{17}) \quad \textbf{(36)}$$

Integrating the total thermal power delivers the total thermal energy of the system:

$$E_{\text{tot}} = \int \dot{Q}_{\text{tot}} * dt \quad \textbf{(37)}$$

The electric power of the system is the measured electric power of the compressor and the fan of the evaporator. The power of the water pump is not considered. In order to regulate the total water mass flow for the experiments, the water pump runs at 90% of its capacity during the charging of the RPW-HEX and at 5% of its capacity during discharging. Since both of these operating points of the water pump are unrealistic, taking its electrical power into account would greatly falsify the results. The electric energy of the system is again derived by integration over time:

$$E_{\text{el}} = \int (P_{\text{compressor}} + P_{\text{fan}}) * dt = \int P_{\text{el}} * dt \quad \textbf{(38)}$$

The Coefficient of Performance (COP) is the proportion of thermal power to electrical power.

$$COP = \frac{\dot{Q}_{\text{Cond}} + \dot{Q}_{\text{RPW}_{\text{W}}}}{P_{\text{el}}} = \frac{\dot{Q}_{\text{tot}}}{P_{\text{el}}} \quad \textbf{(39)}$$

Since the COP is only meaningful at a certain point in time or for a static system, the performance factor (PF) is introduced to describe the dynamic system. The PF is calculated from the thermal energy divided by the electrical energy:

$$PF = \frac{\int \dot{Q}_{\text{Cond}}\, dt + \int \dot{Q}_{RPW_W}\, dt}{\int P_{\text{el}}\, dt} = \frac{\int \dot{Q}_{\text{tot}}\, dt}{\int P_{\text{el}}\, dt} = \frac{E_{\text{tot}}}{E_{\text{el}}} \quad \textbf{(40)}$$

The energy of the RPW-HEX determined on the waterside accounts for the energy losses,

$$E_{\text{loss}} = \int_{t_0}^{t_2} \dot{Q}_{RPW_R} * dt - \int_{t_1}^{t_2} \dot{Q}_{RPW_W} * dt \quad \textbf{(41)}$$

where t_0 reflects the point of time when the RPW-HEX starts to charge, t_1 where the RPW-HEX is charged completely and starts to discharge and t_2 is the end of a whole cycle. E_{loss} can only be obtained by looking at the difference between $\dot{Q}_{RPW_W}$ and $\dot{Q}_{RPW_R}$ at the end of a cycle.

To calculate the performance factor PF $\dot{Q}_{\text{cond}}$ and $\dot{Q}_{\text{RPW}_{\text{W}}}$ is being used:

$$PF = \frac{\int \dot{Q}_{\mathrm{Cond}}\, dt + \int \dot{Q}_{\mathrm{RPW_W}}\, dt}{\int P_{\mathrm{el}}\, dt} = \frac{E_{\mathrm{Cond}} + E_{\mathrm{RPW_W}}}{E_{\mathrm{el}}} \quad \textbf{(42)}$$

$\dot{Q}_{tot}$ also accounts for energy losses in the pipes.

$$\int \dot{Q}_{\mathrm{tot}}\, dt + E_{\mathrm{loss}} = \int \dot{Q}_{\mathrm{Cond}}\, dt + \int \dot{Q}_{\mathrm{RPW_W}}\, dt \quad \textbf{(43)}$$